Habilitation Booklets of the University of Miskolc
Mechanical Engineering Sciences Habilitation Committee

Overview of the Author's Scientific Work
2014–2025

The overview presented in this booklet is based on the review of the author's published peer-reviewed articles and books

SUMMARY OF A FEW RECENT THEORETICAL AND PRACTICAL ADVANCES IN THE FIELD OF ANISOTROPIC TURBULENCE MODELLING AND NUMERICAL SOLUTION OF THE NAVIER–STOKES EQUATIONS

Written by

Dr. László Könözsy

who is a Reader at Cranfield University, United Kingdom

and

who is applying for the title "dr. habil."
in the field of Mechanical Engineering Sciences
at the University of Miskolc, Hungary

MISKOLC-EGYETEMVÁROS
2025

A Miskolci Egyetem Habilitációs Füzetei
Gépészeti Tudományok Tudományági Habilitációs Bizottság

Tudományos Munkásság Áttekintő Összefoglalása
2014–2025

A füzetben itt bemutatott áttekintés a szerzőnek az irodalomban megjelent lektorált cikkein és könyvein alapszik

ANIZOTRÓP TURBULENCIA MODELLEZÉSE ÉS A NAVIER–STOKES EGYENLETEK NUMERIKUS MEGOLDÁSA TERÜLETÉN ELÉRT NÉHÁNY ELMÉLETI ÉS GYAKORLATI ELŐRELÉPÉS ÖSSZEFOGLALÁSA

Írta
Dr. Könözsy László
aki egyetemi docens, Cranfieldi Egyetem, Egyesült Királyság

és

aki a Gépészeti Tudományok tudományágban a "dr. habil." cím elnyerésére pályázik a Miskolci Egyetemen, Magyarországon

MISKOLC-EGYETEMVÁROS
2025

Author's Declaration

This habilitation booklet is submitted to the University of Miskolc, Hungary in support of the author's application for the title "dr. habil." which is an academic qualification and not a scientific degree. The material presented in this habilitation booklet is written with the author's own words as an overview of his scientific work based on a broad review of a few of his published peer-reviewed articles and books which is part of the application process for the title "dr. habil." at the University of Miskolc, Hungary.

The material presented in this habilitation booklet is based on the overview of those peer-reviewed articles and books which were published by the author after receiving his PhD degree (2004) from the University of Miskolc, Hungary as one of the requirements for applying for the title "dr. habil." at the University of Miskolc, Hungary.

I declare a) no conflict of interest, b) that this summary/overview/review work submitted has been written by me alone with my own words, c) that this summary/overview/review work submitted has not been previously submitted to the University of Miskolc, Hungary or any other universities, d) that all content is true to the best of my knowledge, e) that all quotations and references have been duly acknowledged according to the requirements of academic research, and f) that the current version of this summary/overview/review work submitted has been prepared only for academic use and non-commercial purposes.

Dr. László Könözsy,
MSc, PhD, PhD, FHEA

Cranfield, 05. 05. 2025

Copyright Permissions

This habilitation booklet is submitted to the University of Miskolc, Hungary in support of the author's application for the title "dr. habil." which is an academic qualification and not a scientific degree. The material presented in this habilitation booklet is written with the author's own words as an overview of his scientific work based on a broad review of a few of his published peer-reviewed articles and books which is part of the application process for the title "dr. habil." at the University of Miskolc, Hungary.

The material presented in this habilitation booklet is based on the overview of those peer-reviewed articles and books which were published by the author after receiving his PhD degree (2004) from the University of Miskolc, Hungary as one of the requirements for applying for the title "dr. habil." at the University of Miskolc, Hungary.

The hypothesis and theory in the author's previously published work overviewed in Chapter 2 were used with permission of Springer Nature BV, Switzerland, from the book entitled as "A New Hypothesis on the Anisotropic Reynolds Stress Tensor for Turbulent Flows", Author: László Könözsy, Volume I, Chapter 5, pp. 105-126, 1st. Edition 2019; the permission conveyed through Copyright Clearance Center, Inc.

Simulation results on the numerical prediction of anisotropic Reynolds stresses in the author's previously published work overviewed in Section 2.5 were used with permission of Springer Nature BV, Switzerland, from the book entitled as "A New Hypothesis on the Anisotropic Reynolds Stress Tensor for Turbulent Flows", Author: László Könözsy, Volume II, Chapter 4, pp. 222-231, pp. 244-252; Chapter 5, pp. 362-364, pp. 370-376, 1st. Edition 2021; the permission conveyed through Copyright Clearance Center, Inc.

Figures 2.1, 2.2, 2.3, 2.4, 2.5, 2.6 presented in Subsection 2.5.1 used with permission of Springer Nature BV, Switzerland, from the book entitled as "A New Hypothesis on the Anisotropic Reynolds Stress Tensor for Turbulent Flows", Author: László Könözsy, Volume II, Chapter 4, p. 223, p. 224, p. 247, p. 248, p. 250, p. 251, 1st. Edition 2021; the permission conveyed through Copyright Clearance Center, Inc.

Figures 2.7, 2.8, 2.9, 2.10, 2.11 presented in Subsection 2.5.2 used with permission of Springer Nature BV, Switzerland, from the book entitled as "A New Hypothesis on the Anisotropic Reynolds Stress Tensor for Turbulent Flows", Author: László Könözsy, Volume II, Chapter 5, p. 362, p. 372, p. 373, 1st. Edition 2021; the permission conveyed through Copyright Clearance Center, Inc.

Some parts of the theory and equations overviewed in Section 3.3 were first published in the article entitled as "A Unified Fractional-Step, Artificial Compressibility and Pressure-Projection Formulation for Solving the Incompressible Navier–Stokes Equations", Authors: László Könözsy and Dimitris Drikakis, *Communications in Computational Physics*, Vol. 16, No. 5, pp. 1135-1180, November 2014, ISSN: 1815-2406, published by Global Science Press. The original publication overviewed in Section 3.3 is credited according to the copyright agreement signed with Global Science Press.

Parts of redrawn Figures 3.1, 3.2, 3.3, 3.4 and parts of simulation results overviewed in Subsection 3.3.2 were first published in the article entitled as "A Unified Fractional-Step, Artificial Compressibility and Pressure-Projection Formulation for Solving the Incompressible Navier–Stokes Equations", Authors: László Könözsy and Dimitris Drikakis, *Communications in Computational Physics*, Vol. 16, No. 5, pp. 1135-1180, November 2014, ISSN: 1815-2406, published by Global Science Press. The original publication is credited according to the copyright agreement signed with Global Science Press.

Parts of Figures 3.5, 3.6 and results reviewed in Subsection 3.3.2 were first published in the article entitled as "Predicting Non-linear Flow Phenomena Through Different Characteristics-Based Schemes", Authors: Tom-Robin Teschner, László Könözsy and Karl W. Jenkins, *Aerospace*, Vol. 5, No. 1:22, pp. 1-20, 2018, published by Multidisciplinary Digital Publishing Institute under an open access Creative Common CC BY license.

Figures 3.7, 3.8, 3.9 in Subsection 3.4.3 were first published in the work entitled as "Pseudo-Transient Pressure-Momentum Coupling Method for Low-Speed Incompressible Flows", Author: László Könözsy, *In: MultiScience - XXXI. microCAD International Multidisciplinary Scientific Conference, University of Miskolc, Hungary*, CD-ROM, ISBN 978-963-358-132-2, 20-21 April 2017, published by the University of Miskolc.

Dr. László Könözsy,
MSc, PhD, PhD, FHEA

Cranfield, 05. 05. 2025

Contents

Author's Declaration iii

Copyright Permissions iv

Acknowledgements viii

Summary ix

Összefoglalás xi

Nomenclature xiii

1 Introduction 1

2 Advances in Anisotropic Turbulence Modelling for Incompressible Flows 2

2.1 Introduction . . . 2

2.2 A brief literature review and its critical assessment . . . 3

2.3 Unification of the Boussinesq hypothesis and the three-dimensional mechanical similarity theory of turbulent velocity fluctuations . . . 4

2.3.1 Anisotropic modification to the Boussinesq hypothesis . . . 8

2.4 The anisotropic hybrid k-ω SST/STM closure model . . . 10

2.4.1 Anisotropic modification to the k-ω SST closure model . . . 10

2.4.2 Divergence of the anisotropic Reynolds stress tensor . . . 13

2.4.3 The modified turbulent kinetic energy k production term . . . 14

2.4.4 The modified specific dissipation rate ω production term . . . 14

2.4.5 Governing equations of the hybrid k-ω SST/STM closure model . 15

2.5 Numerical prediction of anisotropic Reynolds stresses . . . 17

2.5.1 Reynolds stresses in a 2D turbulent flow over a flat plate . . . 17

2.5.2 Reynolds stresses in a 3D turbulent flow in a cylindrical pipe . . . 25

2.6 Summary of the contribution to the knowledge . . . 31

2.7 Új tudományos eredmények összefoglalása . . . 33

Contents

3 Advances in the Numerical Solution of the Navier–Stokes Equations **35**

3.1 Introduction 35

3.2 A brief literature review and its critical assessment 36

3.2.1 Marker and Cell Pressure-Projection (MAC-PP) method (1965) . 36

3.2.2 Artificial Compressibility (AC) method (1967) 37

3.2.3 Fractional-Step Pressure Projection (FS-PP) method (1968) . . . 39

3.2.4 Hybrid pressure-velocity coupling methods 40

3.3 Unification of the AC and FS-PP solution methods 41

3.3.1 Overview of the theoretical background 41

3.3.2 Overview of simulation results on benchmark problems 48

3.4 Development of a two-stage pseudo-transient solution method 57

3.4.1 Review of the background of the method development 57

3.4.2 Derivation of a pseudo-transient pressure evolution equation . . . 58

3.4.3 Laminar flow in a horizontal microfluidic channel 63

3.5 Summary of the contribution to the knowledge 67

3.6 Új tudományos eredmények összefoglalása 70

References **73**

References to the Author's Contributions **83**

Author's Selected Publications **85**

Author's Books **89**

Acknowledgements

It is essential for professional development to work together with supervisors at the beginning of an academic career. Therefore, I would like to commemorate and thank those supervisor professors who have since passed away, Professor Dr. Tibor Czibere, Professor Dr. András Nyíri and Dr. Árpád Fáy who supported my professional development and academic career 25 years ago at the University of Miskolc, Hungary. Without their outstanding teaching and supervisory work, I would not have achieved those successes, either in national or international academic life, what I am indeed having today. Looking back in time, I can see clearly that the foundations of my knowledge in the field of mathematics, fluid mechanics and mathematical physics gained through working with them in a daily basis long time ago. Therefore, I will always think of their work with great respect throughout my professional career and during my whole life. I find it also important to commemorate here the role of my father in my professional development—who was an applied mathematician and a mechanical engineer—because he introduced me to the world of chess, mathematics, computer science and book writing activity since my childhood encouraging me to choose a scientific career path in my life.

I would like to thank Professor Karl W. Jenkins, who is the Head of Centre for Computational Engineering Sciences at Cranfield University, UK, for writing reference letters and supporting the submission of my application and this habilitation booklet for the title "dr. habil." qualification at the University of Miskolc, Hungary.

I would like to thank Professor Dimitris Drikakis for bringing my attention to the importance of the numerical solution of the Navier–Stokes equations for incompressible fluid flows at low and moderate Reynolds numbers. Working with him 17 years ago at Cranfield University, UK, inspired me to develop different numerical procedures in this research field using high-resolution Godunov-type or other discretisation schemes.

I would like to express my gratitude to my co-authors, Dr. Tom-Robin Teschner, Dr. Zeeshan A. Rana and Mr. Hrishabh Chaudhary, who encouraged me to write this habilitation booklet as an overview of my scientific work.

I owe my thanks and gratitude to my family and loved ones who honored me with their patience when I was working on my habilitation application and writing this booklet.

Dr. László Könözsy,
MSc, PhD, PhD, FHEA

Cranfield, 05. 05. 2025

Summary

This habilitation booklet is an overview of the author's works based on his already published scientific articles and books in the literature, which deals with the investigation of three research areas for incompressible fluid flows. The background of the author's research work can be found in Chapter 1. Following that, a new anisotropic Reynolds stress tensor equation has been introduced in conjunction with its physical background which is relying on the unification of the deformation theory based Boussinesq hypothesis and the three-dimensional similarity theory of turbulent velocity fluctuations. This theoretical development may be considered as a new achievement in the field of current turbulence research, because according to the author's knowledge, no other researchers have previously made any attempt, either theoretically or practically, to unify these two theories. The new equation of the anisotropic Reynolds stress tensor, which has been introduced, modifies the terms in the governing equations of the Reynolds-Averaged Navier–Stokes (RANS) turbulence models used in the industry; thus it modifies the source term of the Reynolds momentum equation and the turbulent energy production terms which are playing roles in the physical description of the turbulence phenomenon. The theoretical developments and practical results summarised in this booklet differ from the computational method discussed in the author's PhD thesis[1] (2004) which dealt with the development of a numerical procedure for solving the curvilinear rotationally-symmetric mean vorticity transport equation. Note that in both cases, the anisotropic nature of the turbulence phenomenon played an important role and the vorticity transport theory was a starting point, which are indispensable in the research due to the vortical nature of turbulent flows.

The new anisotropic Reynolds stress tensor introduced by the author requires the development of new closure models which are relevant from an engineering point-of-view. Therefore, the second subject area of this habilitation booklet is the overview of the development of a new turbulence model through the anisotropic modification to Menter's k-ω Shear-Stress Transport (SST) engineering turbulence model which is relying on the momentum transport theory leading to a mathematical formulation which was previously unknown in the literature. In conjunction with that, new mathematical terms have been derived for the production terms of the turbulent kinetic energy k and the specific dissipation rate ω transport equations which led to a mathematical formulation of a new

[1] Könözsy, L., "Computation of Two-Dimensional Shear Flows with the Solution of the Turbulent Vorticity Transport Equation" (in Hungarian), PhD Thesis, University of Miskolc, István Sályi Doctoral School of Mechanical Engineering Sciences, Miskolc-Egyetemváros, Hungary, 2004.

hybrid engineering turbulence model. For the sake of brevity, the computational results obtained with the new Reynolds stress tensor and the new hybrid anisotropic turbulence model have also been compared against experimental data for two benchmark problems with particular attention to the distribution of Reynolds stresses. The validation of the new hybrid anisotropic turbulence model has been carried out for several engineering benchmark test cases which can be found in the articles and books of the author of this booklet. It is important to emphasise that the developers of turbulence models based on the Taylor [1]–von Kármán [2]–Kolmogorov [3] isotropic theory of turbulence primarily focus on the physical investigation of the Reynolds-averaged mean velocity and pressure field data with approximate or technically acceptable accuracy which has of relevance in engineering practice while they neglect the accurate distribution of anisotropic Reynolds stresses. Therefore, turbulence models based on the theory of isotropic turbulence have a limited range of applicability in the investigation of the internal mechanism of turbulence in-depth due to their incapability of predicting the distribution of anisotropic Reynolds stresses. Taking into account the anisotropy of Reynolds stresses is important from both a physical and an engineering point-of-view, because in most practical fluid flow problems, the effect of walls is present, and near to that the effect of the anisotropy of Reynolds stresses is amplified as well. Therefore, a more accurate mathematical description of the physics of turbulence is an indispensable task for solving both scientific and industrial problems. Advances made in the field of anisotropic turbulence modelling and a summary of the corresponding contribution to the knowledge are discussed in Chapter 2.

The third subject area of this habilitation booklet focuses on some of the latest results of the author's research work in the field of numerical solution of the Navier–Stokes momentum equations for incompressible fluid flows. A new approach and numerical solution method for pressure-velocity field coupling have been developed through the unification of methods relying on hyperbolic- and elliptic-type pressure-velocity coupling closure equations. The foundations and initial results of the corresponding mathematical approach were discussed through computational examples in the author's second PhD thesis[2] (2012) at Cranfield University, United Kingdom, which can be considered as starting points. Therefore, we deal with results from further improvement and further validation of the latter method which were published after 2012. Furthermore, a new pseudo-transient two-stage pressure-velocity coupling algorithm is overviewed which is discussed in Chapter 3. This research area is in connection with the subject area of anisotropic turbulence modelling in that way that the numerical procedure developed for solving the Navier–Stokes equations—by considering the Reynolds stress tensor as a source term—can also be extended to solving the Reynolds equations. In the latter case, the solution of the scalar transport equations of the employed engineering turbulence model have to be taken under consideration. The formulation of the contribution to the knowledge can be found in English and Hungarian languages at the end of the chapters.

[2]Könözsy, L., "Multiphysics CFD Modelling of Incompressible Flows at Low and Moderate Reynolds Numbers", PhD Thesis, Department of Engineering Physics, College of Aeronautics, Cranfield University, Cranfield, Bedfordshire, United Kingdom, 2012.

Összefoglalás

Ez a habilitációs füzet a szerzőnek az irodalomban már megjelent tudományos cikkein és könyvein alapulú eredményeinek áttekintő bemutatása, amely összenyomhatatlan közegek áramlásra esetén három kutatási terület vizsgálatával foglalkozik. A kutatómunka hátterének ismertetését az 1. Fejezet tartalmazza. Ezután egy új anizotróp Reynolds-féle feszültségtenzor egyenletének a bevezetésére kerül sor annak fizikai hátterének bemutatásával együtt, amely az alakváltozási eleméleten nyugvó Boussinesq hipotézisnek és a sebességingadozások háromdimenziós hasonlósági elméletének egyesítésén alapszik. Ez az elméleti fejlesztőmunka a jelenlegi turbulencia kutatás területén új tudományos eredménynek tekinthető, mert a szerző ismeretei szerint az előző két elmélet egyesítésére más kutatók korábban sem elméleti, sem gyakorlati szempontból nem tettek kísérletet. A bevezetett anizotróp Reynolds-féle feszültségtenzor új egyenlete módosítja a Reynolds-Átlagolt Navier–Stokes (RANS) egyenletek megoldására összpontosító, az iparban használt turbulencia modellekben szereplő tagokat, így módosítja a Reynolds-féle mozgásegyenlet forrástagját és a turbulencia jelenségének leírásában szerepet játszó turbulens energia produkciójára vonatkozó tagokat. Az itt ismertetett elméleti fejlesztések és gyakorlati eredmények eltérnek a szerző PhD értekezésében[1] (2004) tárgyalt számítási módszertől, amely a turbulens örvénytranszport középsebességtérben érvényes egyenletének görbevonalú forgásszimmetrikus megoldására vonatkozó numerikus eljárás kidolgozásával foglalkozott. Itt fontos megjegyezni, hogy mindkét esetben a turbulencia jelenségének anizotróp természete jelentős szerepet játszott, és a turbulens örvénytranszport elmélete mindkét esetben kiindulási pontként szolgált, amelyek a turbulens áramlások örvényes természete miatt a kutatómunka során nélkülözhetetlenek.

A szerző által bevezetett új anizotróp Reynolds-féle feszültségtenzor új műszaki szempontból jelentős zárási modellek kidolgozását követeli meg. Ezért a habilitációs füzet második tématerülete a momentum transzport elméleten alapuló Menter-féle k-ω nyírófeszültségtranszport (SST) műszaki turbulencia modell anizotróp módosításával egy új turbulencia modell fejlesztésének áttekintése, amelynek matematikai megfogalmazása az irodalomban korábban nem volt ismert. Ennek kapcsán a turbulens kinetikus energia k produkciójára és a fajlagos disszipáció arány ω transzportjának produkciójára vonatkozóan új tagok levezetésére kerül sor, amely egy új hibrid műszaki turbulencia

[1] Könözsy, L., "Kétdimenziós Nyíróáramlások Számítása a Turbulens Örvénydiffúzió Differenciálegyenletének Megoldásával", PhD Értekezés, Miskolci Egyetem, Sályi István Gépészeti Tudományok Doktori Iskola, Miskolc-Egyetemváros, Magyarország, 2004.

modell matematikai megfogalmazásához vezet. Az új Reynolds-féle feszültségtenzorral és az új hibrid anizotróp turbulencia modellel kapott számítási eredményeket terjedelmi korlátok miatt két alapfeladat esetén mérési eredményekkel is összehasonlítjuk, különös tekintettel a Reynolds-féle feszültségek eloszlására vonatkozóan. A kifejlesztett új hibrid anizotróp turbulencia modell validálása több műszaki alapprobléma esetére is el lett végezve, amelyek a szerző cikkeiben és könyveiben megtalálhatóak. Ezt azért is fontos hangsúlyozni, mert a Taylor [1]–von Kármán [2]–Kolmogorov [3] izotróp turbulencia elméletén alapuló modellek fejlesztői elsődlegesen a mérnöki gyakorlatban fontos Reynolds-átlagolt középsebességtér és nyomástér adatrendszerének megközelítően vagy műszaki szempontból elfogadhatóan pontos előállítását tartják a fizikai vizsgálat céljának, miközben az anizotróp Reynolds-féle feszültségek pontos eloszlását elhanyagolják. Így az irodalomban ismert izotróp turbulencia elméletén alapuló modellek az anizotróp Reynolds-féle feszültségeloszlás elhanyagolásának következtében a turbulencia mélyebb belső mechanizmusának vizsgálatára csak korlátozottan alkalmasak. A Reynolds-féle feszültségek anizotrópiájának figyelembe vétele mind fizikai, mind műszaki szempontból fontos, mert a legtöbb gyakorlatban előforduló áramlástani probléma esetén a falak hatása érvényesül, amelyek közelében a Reynolds feszültségek anizotrópiájának hatása is felerősödik. Tehát a turbulencia jelenségében fellépő fizikai hatások matematikai szempontból is pontosabb leírása mind a tudományos, mind az ipari problémák megoldásának esetén nélkülözhetetlen feladat. A anizotróp turbulencia modellezésének területén elért előrelépéseket és az új tudományos eredmények összefoglalását a 2. Fejezet tárgyalja.

A habilitációs füzet harmadik tématerülete az összenyomhatatlan közegek áramlására érvényes Navier–Stokes mozgásegyenletek numerikus megoldásának területén a szerző által végzett kutatómunka néhány legutóbb elért eredményét mutatja be. A nyomástér-sebességtér összekapcsolására vonatkozó új megközelítés és megoldási módszer lett kifejlesztve a hiperbolikus és elliptikus nyomástér-sebességtér zárási egyenletein alapuló módszerek egyesítésén keresztül. Az ide vonatkozó matematikai megközelítés alapjait és kezdeti eredményeit a szerző Cranfieldi Egyetemen, az Egyesült Királyságban készített második PhD értékezése[2] (2012) számítási példákon keresztül tárgyalta, amelyek kiindulási pontoknak tekinthetőek. Itt az utóbbi módszer tovább fejlesztéséből és validálásából származó eredményekkel foglalkozunk, amelyek 2012 után lettek publikálva. Továbbá, egy új pszeudo-tranziens kétlépcsős nyomástér-sebességtér összekapcsolási algoritmust is áttekintünk, amelyet a 3. Fejezet ismertet. Ez a kutatási terület úgy kapcsolódik az anizotróp turbulencia modellezéséhez, hogy a Navier–Stokes mozgásegyenletek megoldására kidolgozott numerikus eljárás—a Reynolds-féle feszültségtenzor forrástagként való figyelembevételével—a Reynolds-féle mozgásegyenletek megoldására is kiterjeszthető. Ez utóbbi esetben az alkalmazott műszaki turbulencia modell skalár transzportegyenleteinek megoldására is tekintettel kell lenni. Az új tudományos eredmények megfogalmazása angol és magyar nyelven a fejezetek végén megtalálhatóak.

[2]Könözsy, L., "Multiphysics CFD Modelling of Incompressible Flows at Low and Moderate Reynolds Numbers", PhD Thesis, Department of Engineering Physics, College of Aeronautics, Cranfield University, Cranfield, Bedfordshire, United Kingdom, 2012.

Nomenclature

Symbol	Unit	Description
$\mathbf{g}$	m/s^2	Gravitational vector field
$\underline{\underline{\mathrm{I}}}$	–	Unit tensor
k	m^2/s^2	Turbulent kinetic energy
$\mathbf{u}$	m/s	Velocity vector
$\mathbf{u}'$	m/s	Velocity fluctuation vector
u, v, w	m/s	Scalar velocity components
$u_\infty, v_\infty, w_\infty$	m/s	Reference velocity values
$\mathbf{U}$	–	Dimensionless velocity vector
U, V, W	–	Dimensionless scalar velocity components
L	m	Reference length
p	Pa	Pressure field
P	–	Dimensionless pressure field
Re	–	Reynolds number
s_h	m	Step-height of a sudden expansion channel
$\underline{\underline{\mathrm{S}}}$	$1/s$	Rate-of-strain tensor
t	s	Time
x, y, z	m	Cartesian coordinates
X, Y, Z	–	Dimensionless Cartesian coordinates
β	–	Closure function in Chapter 2
β		Numerical convergence parameter in Chapter 3
$\beta^\star$	–	Closure constant in Chapter 2
γ	–	Closure function in Chapter 2
γ_s	–	Safety-factor
Θ	$kg/(m{\cdot}s^2)$	Principal turbulent (Reynolds) shear stress
μ	$Pa{\cdot}s$	Dynamic viscosity
μ_t	$Pa{\cdot}s$	Dynamic eddy (turbulent) viscosity
μ_Θ	–	Dimensionless scalar weight parameter
ν	m^2/s	Kinematic viscosity
ν_t	m^2/s	Kinematic eddy (turbulent) viscosity
$\underline{\underline{\tau}}^{RA}$	$kg/(m{\cdot}s^2)$	Anisotropic Reynolds stress tensor

ρ	kg/m^3	Fluid density
ρ_∞	kg/m^3	Reference density
ω	$1/s$	Specific dissipation rate
ω_P	$-$	Relaxation factor for the pressure
$\mathbf{\Omega}$	$1/s$	Mean vorticity vector
$\mathbf{\Omega}'$	$1/s$	Vorticity fluctuation vector

Abbreviations

1D, 2D, 3D	One-, Two-, Three-Dimensional
AC	Artificial Compressibility
CB	Characteristics-based
CFD	Computational Fluid Dynamics
CFL	Courant-Friedrichs-Lewy
DNS	Direct Numerical Simulation
FDM	Finite Difference Method
FEM	Finite Element Method
FMG-FAS	Full-MultiGrid, Full-Approximation-Storage
FVM	Finite Volume Method
FSAC-PP	Fractional-Step Artificial Compressibility with Pressure-Projection
FS-PP	Fractional-Step Pressure-Projection
ILES	Implicit Large Eddy Simulation
MAC	Marker-and-Cell
MCB	Multi-directional Characteristics-based
PP	Pressure-Projection
PVC	Pressure-Velocity Coupling
RST	Reynolds Stress Transport
SIMPLE	Semi-Implicit Method for Pressure-Linked Equations
SOR	Successive Over-Relaxation
SST	Shear-Stress Transport
STM	Stochastic Turbulence Model
WENO	Weighted Essentially Non-Oscillatory

Operators

∇	Nabla differential operator
∇^2	Second-order Laplacian differential operator
$\otimes$	Tensor product
$\cdot\cdot$	Double dot product of two second-rank tensors

Chapter 1

Introduction

The author of this habilitation booklet started his academic teaching and research career at the University of Miskolc, Hungary. After graduating as an MSc student in mechanical engineering (1999), he started to teach practical classes and computer laboratory sessions as a PhD student (1999-2002) at different higher education levels. He gave theoretical lectures as an Assistant Lecturer (2002-2005) and an Assistant Professor (2005-2006). During that time, he was studying mathematical and mechanical engineering science subjects in particular attention to fluid mechanics, mathematical physics and numerical analysis.

The author of this review booklet conducted research in the field of computational fluid dynamics (CFD), mathematical modelling and numerical analysis focusing on a numerical method development for solving the mean turbulent vorticity transport equation in straight and rotationally-symmetric curvilinear computational domains which are relevant in practice. He received his PhD degree (2004) in mechanical engineering sciences from the István Sályi Doctoral School of Mechanical Engineering Sciences, University of Miskolc, Hungary. After being a visiting researcher at the University of Siegen (2003) and the Otto von Guericke University of Magdeburg (2005), Germany and a postdoctoral research fellow at the University of Leoben (2006-2008), Austria; then he received his second PhD degree (2013) at Cranfield University, United Kingdom where he is currently a Reader (Associate Professor) in Fluid Mechanics and Computational Engineering.

The author's fundamental research area focuses on the numerical solution of partial differential equations and their computer code implementation through benchmark problems relevant to engineering practice. His research pays particular attention to the mathematical and physical descriptions of tensorial relationships arise in the theory of anisotropic turbulence with their practical applications. His other related research area is the development of pressure-velocity coupling or closure models for solving the incompressible Navier–Stokes equations including their validation through practical examples.

This booklet is a summary of the author's research works based on a broad review of a few of his published peer-reviewed articles and books after 2004 to summarise a few theoretical and practical advances: a) in the field of anisotropic turbulence in Chapter 2, and b) in the development of pressure-velocity closure models for solving the incompressible Navier–Stokes equations in the context of pseudo-transient methods in Chapter 3.

Chapter 2

Advances in Anisotropic Turbulence Modelling for Incompressible Flows

2.1 Introduction

In the field of two-equation Reynolds-Averaged Navier–Stokes (RANS) turbulence modelling, there is a scientific and industrial demand for new mathematical formulations of the anisotropic Reynolds stress tensor, because the already existing and widely used Boussinesq hypothesis (1877) [4], [5] does not represent the physically correct behaviour of the anisotropic Reynolds stress distribution for turbulent flows. Therefore, a possible way to find a plausible approach on the physically correct mathematical description of the anisotropic Reynolds stress tensor is the unification of two or more existing and validated hypotheses. Könözsy (2019) [6, pp. 109-111] proposed the unification of the Boussinesq hypothesis (2.14) [4] and the three-dimensional anisotropic similarity hypothesis of turbulent velocity fluctuations (2.19) [7], [8] in a single tensor equation (2.25). In this Chapter, two research subjects have been summarised after a very short literature review and its critical assessment in Section 2.2. A brief overview of the derivation of the recently proposed new hypothesis on the anisotropic Reynolds stress tensor (2.25) [6, pp. 105-126] has been described in Section 2.3. An overview of the development of an anisotropic hybrid k-ω Shear-Stress Transport/Stochastic Turbulence Model (SST/STM) closure approach [6, pp. 105-126]—which is an anisotropic modification to the two-equation k-ω SST model of Menter [9], [10]—has been discussed in Section 2.4. In terms of the numerical prediction of the anisotropic Reynolds stress distributions in turbulent flows, simulation results have been overviewed in Section 2.5. For the sake of simplicity, incompressible turbulent flows have been considered in this habilitation booklet[1].

[1]The hypothesis and theory in the author's previously published work overviewed here in Chapter 2 were used with permission of Springer Nature BV, Switzerland, from the book entitled as "A New Hypothesis on the Anisotropic Reynolds Stress Tensor for Turbulent Flows", Author: László Könözsy, Volume I, Chapter 5, pp. 105-126, 1st. Edition 2019; the permission conveyed through Copyright Clearance Center, Inc., https://www.copyright.com/

2.2 A brief literature review and its critical assessment

The literature on turbulence modelling is very extensive and the anisotropic nature of the turbulence phenomenon can be modelled and simulated in many different ways. The Direct Numerical Simulation (DNS) is the most accurate approach up to date to predict accurately the fluctuating behaviour of turbulent flows where the unsteady Navier–Stokes equations are solved numerically on the finest possible computational mesh ignoring the time-averaged source terms in the Reynolds momentum equation (2.2). The DNS is a computationally demanding numerical technique due to the required high spatial resolution of the computational mesh and very small time-step size. Therefore, researchers use the DNS technique for simple and small geometries to carry out numerical investigations to understand deeper the physics of turbulence. The application of the DNS technique for industrially relevant complex and large-scale geometries is not yet feasible due to the long computational time. Another possible way to simulate the anisotropic nature of turbulent flows is to use Reynolds Stress Transport (RST) models in which case a transport equation has to be solved for each Reynolds stress. In that case, turbulence modelling play an important role. For incompressible turbulent flows, Daly and Harlow (1970) [11] derived Reynolds stress transport equations to take into account the anisotropic behaviour of Reynolds stresses. Launder, Reece and Rodi (1975) [12] proposed a RST closure model which is called LRR model with a particular attention to the prediction of the pressure-strain correlations. An effective-viscosity hypothesis was proposed by Pope (1975) [13] where the Reynolds stress tensor was described with a tensor polynomial involving the rate-of-strain and vorticity tensors. To predict accurately the anisotropic Reynolds stress distribution in the near-wall region, Speziale, Sarkar and Gatski (1990) [14] proposed a RST closure model which is called SSG model. With the combination of the SSG and LRR closure models, Eisfeild and Brodersen (2005) [15] developed the SSG/LRR-ω RST model for aerospace applications. For three-dimensional turbulent flows behind bluff bodies, a modified hybrid SSG/LRR-ω RST closure model was proposed by Klajbár et al. (2016) [16] using a simplified diffusion approach. A detailed overview can be found in the work of Pope [17] on RST closure models and DNS with their applications.

Another possible way to model the anisotropic behaviour of Reynolds stresses relevant to our subject is the anisotropic modification to the widely used Boussinesq hypothesis (2.14) [4] in the framework of two-equation RANS models [18]. Craft et al. (1996) [19] proposed a cubic eddy-viscosity approach to capture accurately the physical behaviour of the Reynolds stresses and the effect of streamline curvature. For simulating anisotropic transitional turbulent flows, Craft et al. (1997) [20] proposed a non-linear eddy viscosity model based on a cubic relationship among the stress, rate-of-strain and vorticity tensors. Abe et al. (2003) [21] proposed closure approximations to study the anisotropic behaviour of Reynolds stresses in the near-wall region in the framework of non-linear eddy viscosity models. In the context of the two-equation k-ω SST closure model [9], [10], Vitillo et al. (2015) [22] proposed a non-linear eddy viscosity formulation based anisotropic shear stress transport (ASST) approach and validated it for different benchmark problems.

All of these non-linear eddy viscosity two-equation engineering turbulence models are relying on the anisotropic modification to the Boussinesq hypothesis (2.14) [4] which are computationally less demanding than the DNS approach and RST models. Therefore, two-equation RANS models are used in industry in a daily basis and are still in the centre of research interest in the context of anisotropic engineering turbulence modelling.

Within the family of k-ω formulation-based turbulence models, the k-ω SST closure model of Menter [9], [10], [23] is a widely used and validated RANS model [18], [24], because of its advantageous properties, i.e., it can predict accurately the mean fluid flow in the boundary and is capable of capturing adverse pressure gradients [23]. Therefore, an anisotropic modification [6, pp. 105-126] to the k-ω SST model [9], [10], [23] in the context of linear eddy viscosity approaches was desirable due to low computational cost and expectedly high accuracy for wide range of engineering applications. The three-dimensional (3D) anisotropic similarity hypothesis of turbulent velocity fluctuations (2.19) proposed by Czibere (2001, 2006) [7], [8] is a different approach compared to the rate-of-strain tensor formulation-based Boussinesq hypothesis (2.14) (1877) [4]. The 3D similarity theory of turbulent velocity fluctuations [7], [8] is a further extension of the 2D von Kármán [25]–[27] hypothesis on oscillatory motions to 3D turbulent flows excluding the presence of the rate-of-strain tensor. Therefore, Könözsy (2019) [6, pp. 109-111] unified the Boussinesq hypothesis (1877) [4] and the 3D anisotropic similarity hypothesis (2001, 2006) [7], [8] in a single tensor equation (2.25) which was previously a gap in the knowledge in field of turbulence research. The unification of these two different theories led to the development of a two-equation anisotropic hybrid k-ω SST/STM closure model which could be a step forward in modelling the physically correct behaviour of Reynolds stress distributions for incompressible turbulent flows. Note that the unification of the Boussinesq hypothesis [4] and the 3D anisotropic similarity hypothesis [7], [8] led to a hypothesis on the anisotropic Reynolds stress tensor (2.25) is a different approach compared to other works in this field in [19], [20], [22], [28]–[31].

2.3 Unification of the Boussinesq hypothesis and the three-dimensional mechanical similarity theory of turbulent velocity fluctuations

Könözsy (2019) [6, pp. 109-111] proposed a new Reynolds stress tensor through the anisotropic modification to the Boussinesq hypothesis [4] which led to the unification of the deformation theory [4] and the three-dimensional anisotropic similarity theory of turbulent velocity fluctuations [7], [8]. We overview and summarise here the main steps of the unification of these two hypotheses on the anisotropic Reynolds stress tensor.

Turbulent flows are inherently three-dimensional, unsteady, anisotropic and vortical flows [24]. Therefore, let us consider the Reynolds-averaged governing equations of incompressible, isothermal, viscous turbulent flows as a starting point. The continuity equations of the mean and fluctuating velocity and vorticity fields [18], respectively, are

$$\nabla \cdot \mathbf{u} = \nabla \cdot \mathbf{u}' = \nabla \cdot \boldsymbol{\Omega} = \nabla \cdot \boldsymbol{\Omega}' = 0, \tag{2.1}$$

and the Reynolds momentum equation [18] is

$$\rho\frac{\partial \mathbf{u}}{\partial t}+\rho\mathbf{u}\cdot(\nabla\otimes\mathbf{u})=\rho\mathbf{g}-\nabla p+\mu\nabla^2\mathbf{u}+\nabla\cdot\underline{\underline{\tau}}^R, \tag{2.2}$$

and the mean vorticity transport equation [32] is

$$\frac{\partial \boldsymbol{\Omega}}{\partial t}+\mathbf{u}\cdot(\nabla\otimes\boldsymbol{\Omega})-\boldsymbol{\Omega}\cdot(\nabla\otimes\mathbf{u})=\nu\nabla^2\boldsymbol{\Omega}+\nabla\times\overline{(\mathbf{u}'\times\boldsymbol{\Omega}')}, \tag{2.3}$$

and the fluctuating vorticity transport equation [32] is

$$\frac{\partial \boldsymbol{\Omega}'}{\partial t}+\mathbf{u}'\cdot(\nabla\otimes\boldsymbol{\Omega}')-\boldsymbol{\Omega}'\cdot(\nabla\otimes\mathbf{u}')=\nu\nabla^2\boldsymbol{\Omega}+\boldsymbol{\Omega}\cdot(\nabla\otimes\mathbf{u}'), \tag{2.4}$$

where $\mathbf{u}$, $\mathbf{u}'$ and $\boldsymbol{\Omega}$, $\boldsymbol{\Omega}'$ are the mean and fluctuating velocity and vorticity fields, respectively; ρ, μ and ν are the density, dynamic and kinematic viscosities of the fluid, respectively; $\mathbf{g}$ is the gravity field, p is the pressure field, and $\underline{\underline{\tau}}^R$ is the second-rank symmetrical Reynolds stress tensor. In the governing Eqs. (2.1)–(2.4), the mathematical symbols '$\cdot$', '$\otimes$' and '$\times$' stand for the dot, tensor (dyad) and vector (cross) products, respectively; and the twice underline '=' denotes a second-rank tensor, and the overbar notation refers to Reynolds time-averaging. It is known from the field of fluid flow kinematics that the mean and fluctuating velocity gradient tensors $\nabla\otimes\mathbf{u}$ and $\nabla\otimes\mathbf{u}'$ can be decomposed as

$$\nabla\otimes\mathbf{u}=\frac{1}{2}\left[(\nabla\otimes\mathbf{u})+(\nabla\otimes\mathbf{u})^T\right]+\frac{1}{2}\left[(\nabla\otimes\mathbf{u})-(\nabla\otimes\mathbf{u})^T\right]=\underline{\underline{S}}+\underline{\underline{\Omega}}, \tag{2.5}$$

$$\nabla\otimes\mathbf{u}'=\frac{1}{2}\left[(\nabla\otimes\mathbf{u}')+(\nabla\otimes\mathbf{u}')^T\right]+\frac{1}{2}\left[(\nabla\otimes\mathbf{u}')-(\nabla\otimes\mathbf{u}')^T\right]=\underline{\underline{S}}'+\underline{\underline{\Omega}}', \tag{2.6}$$

where the symmetrical part of these sums is the mean and fluctuating rate-of-strain tensors $\underline{\underline{S}}$, $\underline{\underline{S}}'$ and the anti-symmetric part of these sums is the mean and fluctuating vorticity tensors $\underline{\underline{\Omega}}$, $\underline{\underline{\Omega}}'$, respectively. Using the double-decompositions (2.5) and (2.6), the governing transport Eqs. (2.2)–(2.4) for viscous fluid flows can also be written [18] as

$$\rho\frac{\partial \mathbf{u}}{\partial t}+\rho\mathbf{u}\cdot\left(\underline{\underline{S}}+\underline{\underline{\Omega}}\right)=\rho\mathbf{g}-\nabla p+\mu\nabla^2\mathbf{u}+\nabla\cdot\underline{\underline{\tau}}^R, \tag{2.7}$$

$$\frac{\partial \boldsymbol{\Omega}}{\partial t}+\mathbf{u}\cdot(\nabla\otimes\boldsymbol{\Omega})-\boldsymbol{\Omega}\cdot\left(\underline{\underline{S}}+\underline{\underline{\Omega}}\right)=\nu\nabla^2\boldsymbol{\Omega}+\nabla\times\overline{(\mathbf{u}'\times\boldsymbol{\Omega}')}, \tag{2.8}$$

$$\frac{\partial \boldsymbol{\Omega}'}{\partial t}+\mathbf{u}'\cdot(\nabla\otimes\boldsymbol{\Omega}')-\boldsymbol{\Omega}'\cdot\left(\underline{\underline{S}}'+\underline{\underline{\Omega}}'\right)=\nu\nabla^2\boldsymbol{\Omega}+\boldsymbol{\Omega}\cdot\left(\underline{\underline{S}}'+\underline{\underline{\Omega}}'\right), \tag{2.9}$$

which system of transport equations can also be expressed as follows:

$$\rho\frac{\partial \mathbf{u}}{\partial t}+\rho\mathbf{u}\cdot\underline{\underline{S}}+\rho\mathbf{u}\cdot\underline{\underline{\Omega}}=\rho\mathbf{g}-\nabla p+\mu\nabla^2\mathbf{u}+\nabla\cdot\underline{\underline{\tau}}^R, \tag{2.10}$$

$$\frac{\partial \boldsymbol{\Omega}}{\partial t} + \mathbf{u}\cdot(\nabla \otimes \boldsymbol{\Omega}) - \boldsymbol{\Omega}\cdot\underline{\underline{S}} + \boldsymbol{\Omega}\cdot\underline{\underline{\Omega}} = \nu\nabla^2\boldsymbol{\Omega} + \nabla\times\overline{(\mathbf{u}'\times\boldsymbol{\Omega}')}, \tag{2.11}$$

$$\frac{\partial \boldsymbol{\Omega}'}{\partial t} + \mathbf{u}'\cdot(\nabla \otimes \boldsymbol{\Omega}') - \boldsymbol{\Omega}'\cdot\underline{\underline{S}}' - \boldsymbol{\Omega}'\cdot\underline{\underline{\Omega}}' = \nu\nabla^2\boldsymbol{\Omega} + \boldsymbol{\Omega}\cdot\underline{\underline{S}}' + \boldsymbol{\Omega}\cdot\underline{\underline{\Omega}}'. \tag{2.12}$$

We can see from the transport Eqs. (2.10)–(2.12) that the second-rank symmetrical Reynolds stress tensor $\underline{\underline{\tau}}^R = -\rho\overline{\mathbf{u}'\otimes\mathbf{u}'}$, and the velocity $\mathbf{u}'$ and vorticity $\boldsymbol{\Omega}'$ fluctuations are physically related to the mean $\underline{\underline{S}}$ and fluctuating $\underline{\underline{S}}'$ rate-of-strain tensors, and the mean $\underline{\underline{\Omega}}$ and fluctuating $\underline{\underline{\Omega}}'$ vorticity tensors, respectively. Furthermore, the fluctuating vorticity field $\boldsymbol{\Omega}'$, the fluctuating rate-of-strain tensor $\underline{\underline{S}}'$ and the fluctuating vorticity tensor $\underline{\underline{\Omega}}'$ are physically related to the mean vorticity field $\boldsymbol{\Omega}$ based on Eq. (2.12). These points indicate that the anisotropic Reynolds stress tensor $\underline{\underline{\tau}}^R$, i.e., the time-averaged velocity fluctuation tensor in the momentum Eq. (2.2) can be related to the mean rate-of-strain tensor $\underline{\underline{S}}$ and mean vorticity field $\boldsymbol{\Omega}$ or its magnitude $|\boldsymbol{\Omega}|$, because the fluid flow undergoes deformation and exhibits local rigid body rotation when three-dimensional turbulence occurs. The local vorticity magnitude can be computed in Cartesian x_1, x_2, x_3 coordinate system as

$$|\boldsymbol{\Omega}| = \sqrt{\left(\frac{\partial u_3}{\partial x_2} - \frac{\partial u_2}{\partial x_3}\right)^2 + \left(\frac{\partial u_1}{\partial x_3} - \frac{\partial u_3}{\partial x_1}\right)^2 + \left(\frac{\partial u_2}{\partial x_1} - \frac{\partial u_1}{\partial x_2}\right)^2}, \tag{2.13}$$

where u_1, u_2, u_3 are the mean velocity components. For incompressible turbulent flows, according to the deformation theory based Boussinesq hypothesis [4], the anisotropic Reynolds stress tensor $\underline{\underline{\tau}}^R$ in the momentum Eq. (2.2) is physically related to the mean rate-of-strain (deformation) tensor $\underline{\underline{S}}$ and the turbulent kinetic energy k of the flow as

$$\underline{\underline{\tau}}^R = -\rho\overline{\mathbf{u}'\otimes\mathbf{u}'} = 2\mu_t\underline{\underline{S}} - \frac{2}{3}\rho k\underline{\underline{\mathrm{I}}}, \tag{2.14}$$

where μ_t is the dynamic eddy viscosity which represents an increased molecular diffusion in the momentum transfer due to the effect of turbulence and defined [6] by

$$\mu_t = \rho\nu_t, \tag{2.15}$$

where ν_t is the kinematic eddy viscosity coefficient. In the generalised Boussinesq hypothesis (2.14) [4], the mean rate-of-strain (deformation) tensor can be expressed as

$$\underline{\underline{S}} = \frac{1}{2}\left[(\nabla\otimes\mathbf{u}) + (\nabla\otimes\mathbf{u})^T\right] = \frac{1}{2}\sum_{i=1}^{3}\left[\sum_{j=1}^{3}\left(\frac{\partial u_j}{\partial x_i} + \frac{\partial u_i}{\partial x_j}\right)\cdot\left(\mathbf{e}_i\otimes\mathbf{e}_j\right)\right] \equiv \frac{1}{2}\left(\frac{\partial u_j}{\partial x_i} + \frac{\partial u_i}{\partial x_j}\right), \tag{2.16}$$

where the symbol '≡' denotes the use of Einstein's summation convention [33] in which case the summation symbol is omitted when using the Cartesian index notation [34], [35];

and the turbulent kinetic energy k is defined [18] by

$$k = \frac{\overline{\mathbf{u}' \cdot \mathbf{u}'}}{2} = \frac{1}{2}\sum_{i=1}^{3}\overline{u_i' \cdot u_i'} \equiv \frac{1}{2}\overline{u_i' u_i'}, \tag{2.17}$$

and the second-rank unit tensor [35] is

$$\underline{\underline{\mathrm{I}}} = \mathbf{e}_1 \otimes \mathbf{e}_1 + \mathbf{e}_2 \otimes \mathbf{e}_2 + \mathbf{e}_3 \otimes \mathbf{e}_3 = \sum_{i=1}^{3} \mathbf{e}_i \otimes \mathbf{e}_i \equiv \delta_{ij} = \begin{cases} 1 \text{ if } i = j \\ 0 \text{ if } i \neq j \end{cases}, \tag{2.18}$$

which is the Kronecker detla δ_{ij} when using index notation [35]. We can see from Eq. (2.14) that the Boussinesq hypothesis [4] takes into account the contribution of the mean deformation tensor $\underline{\underline{S}}$ (2.16) to the momentum transfer through Reynolds momentum Eq. (2.10) which is a physically plausible hypothesis due to the fact that each control volume of the fluid continuum undergoes deformation. It means that the Boussinesq hypothesis (2.14) [4] ignores the physical contribution of the rigid body rotation of the fluid flow to the turbulent momentum transfer which is present in the governing Eqs. (2.10)–(2.12). Therefore, let us consider another hypothesis on the Reynolds stress tensor based on the three-dimensional mechanical similarity theory of turbulent velocity fluctuations—proposed by Czibere (2001, 2006) [7], [8]—which takes into account the anisotropic distribution of the local vorticity magnitude $|\boldsymbol{\Omega}|$ (2.13) through the product of the principal turbulent shear stress Θ and the rotation $\underline{\underline{G}}$ of the deviatoric similarity tensor $\underline{\underline{H}}^{\star}$ as

$$\underline{\underline{\tau}}^{RCZ} = -\rho\overline{\mathbf{u}' \otimes \mathbf{u}'} = \Theta\underline{\underline{G}} - \frac{2}{3}\rho k\underline{\underline{\mathrm{I}}}, \tag{2.19}$$

where the dominant turbulent shear stress Θ can be modelled through the product of the dynamic eddy viscosity μ_t (2.15) and the local vorticity magnitude $|\boldsymbol{\Omega}|$ [10], [36] as

$$\Theta = -\rho\overline{u_1' u_2'} = \mu_t |\boldsymbol{\Omega}| = \rho a_1 k, \tag{2.20}$$

which is also proportional to the turbulent kinetic energy k according to Bradshaw [36], where $a_1 = 0.3$ is a constant. In the Reynolds stress tensor (2.19), the tensor $\underline{\underline{G}}$ is a dimensionless symmetrical tensor which represents the transformation (rotation) of the deviatoric similarity tensor $\underline{\underline{H}}^{\star}$ between the fluctuating natural orthogonal coordinate system x_1', x_2', x_3' and the physical coordinate system x_1, x_2, x_3 [6]. The elements of the dimensionless anisotropic rotated deviatoric similarity tensor $\underline{\underline{G}}$ can be computed [8] as

$$\underline{\underline{G}} = \underline{\underline{E}} \cdot \underline{\underline{H}}^{\star} \cdot \underline{\underline{E}}^{T}, \quad \text{where} \quad E_{ij} = \mathbf{e}_i \cdot \mathbf{e}_j' \quad \text{and} \quad E_{ji}^{T} = \mathbf{e}_j \cdot \mathbf{e}_i', \quad (i, j = 1, 2, 3), \tag{2.21}$$

where by taking into account the Galilean invariant property of the anisotropic Reynolds stress tensor as a physical requirement, Könözsy (2019) [6] modified the unit base vectors $\mathbf{e}_1'$, $\mathbf{e}_2'$, $\mathbf{e}_3'$ of the locally fluctuating coordinate system x_1', x_2', x_3' compared to the original

theory in [7], [8]. The Galilean invariant fluctuating unit base vectors [37] are

$$\mathbf{e}'_1 = \mathbf{e}'_2 \times \mathbf{e}'_3, \quad \mathbf{e}'_2 = \frac{\triangle\mathbf{u}^{(t)} \times \mathbf{\Omega}^{(t)}}{\left|\triangle\mathbf{u}^{(t)} \times \mathbf{\Omega}^{(t)}\right|}, \quad \mathbf{e}'_3 = -\frac{\mathbf{\Omega}^{(t)}}{\left|\mathbf{\Omega}^{(t)}\right|}, \tag{2.22}$$

where the velocity difference can be computed between two consecutive time points as

$$\triangle\mathbf{u}^{(t)} = \mathbf{u}^{(t)} - \mathbf{u}^{(t-\triangle t)}, \tag{2.23}$$

and $\mathbf{\Omega}^{(t)}$, $\left|\mathbf{\Omega}^{(t)}\right|$ denote the Galilean invariant mean vorticity vector and its magnitude (2.13) at time point t [6], [37], respectively. For Unsteady RANS (URANS) turbulence modelling, the use of Eqs. (2.22)–(2.23) is required. However, for modelling fully-developed (stationary) turbulent flows, i.e., in the case of RANS approach, a practical engineering assumption is to compute the velocity difference between the local mean velocity and the nearest wall velocity as $\triangle\mathbf{u}^{(n)} = \mathbf{u}^{(n)} - \mathbf{u}_{wall}$ at the iteration step (n) to preserve formally the Galilean invariant formulation of the unit base vectors (2.22). Furthermore, note that when fully-developed (stationary) turbulent flows ($t = 0$) are modelled, the Galilean invariance of Eqs. (2.21)–(2.23) should not arise due to the fact that the Galilean transformation equations always consider unsteady ($t \neq 0$) physical problems [6]. Using Eq. (2.21) in the computation of the elements of the Reynolds stress tensor (2.19) of the 3D similarity theory of turbulent velocity fluctuations [8], a modified deviatoric similarity tensor $\underline{\underline{H}}^{\star}$ was proposed by Könözsy (2021) [37], [38] for engineering simulations as

$$\underline{\underline{H}}^{\star} = \begin{bmatrix} \lambda^{\star}_{11}H^{\star}_{11} & H^{\star}_{12} & H^{\star}_{13} \\ H^{\star}_{21} & \lambda^{\star}_{22}H^{\star}_{22} & H^{\star}_{23} \\ H^{\star}_{31} & H^{\star}_{32} & \lambda^{\star}_{33}H^{\star}_{33} \end{bmatrix} = \begin{bmatrix} -\lambda^{\star}_{11}\cdot 0.7312 & 1 & 0.4093 \\ 1 & \lambda^{\star}_{22}\cdot 0.5223 & 0.0520 \\ 0.4093 & 0.0520 & \lambda^{\star}_{33}\cdot 0.2089 \end{bmatrix}, \tag{2.24}$$

where $\lambda^{\star}_{11}$, $\lambda^{\star}_{22}$, $\lambda^{\star}_{33}$ are anisotropic scale factors which can be adjusted based on experimental and/or DNS data [37], [38], and the elements of the modified symmetrical deviatoric similarity tensor $H^{\star}_{i,j}$ $(i, j = 1, 2, 3)$ can be computed based on a stochastic turbulence model (STM) [7] or its variants [38]. One can see more details about the implementation of a variant of the 3D STM in a MATLAB code which can be found in [38, pp. 165-178].

2.3.1 Anisotropic modification to the Boussinesq hypothesis

We can see from the Reynolds stress tensor Eqs. (2.14) and (2.19) that the Boussinesq hypothesis (2.14) [4] and the hypothesis (2.19) of the 3D mechanical similarity theory of turbulent velocity fluctuations [8] on the anisotropic Reynolds stress tensors are two different theories. The Boussinesq hypothesis (2.14) [4] takes into account the deformation of the fluid continuum volume through the mean rate-of-strain tensor $\underline{\underline{S}}$ (2.16), although it ignores the contribution of the rigid body rotation to the turbulent momentum transfer. The anisotropic Reynolds stress tensor (2.19) of the 3D similarity theory [8] takes into account the local magnitude of the vorticity field $|\mathbf{\Omega}|$ (2.13) through the principal

turbulent shear stress Θ (2.20) and its scalar product with the dimensionless symmetrical rotated deviatoric similarity tensor $\underline{\underline{G}}$ (2.21) which represents a rotational motion of the fluid through the local mechanical similarity of 3D turbulent velocity fluctuations [6]. In other words, the anisotropic Reynolds stress tensor (2.19) of the 3D similarity theory [8] takes into account the rotational motion of the fluid flow, although it ignores the contribution of the deformation $\underline{\underline{S}}$ (2.16) to the turbulent momentum transfer. Therefore, it is desirable to unify these two different theories, i.e., the Boussinesq hypothesis (2.14) [4] and the 3D mechanical similarity theory of turbulent velocity fluctuations (2.19) [8] on the anisotropic Reynolds stress tensor, because the deformation and the rotation of the fluid continuum volume are both present in the turbulent momentum transfer. For engineering applications, using Eqs. (2.14) and (2.19), the unification of these two hypotheses/theories was carried out and proposed by Könözsy (2019) [6] as follows:

$$\boxed{\underline{\underline{\tau}}^{RA} = -\rho\overline{\mathbf{u}' \otimes \mathbf{u}'} = 2\mu_t\underline{\underline{S}} + \mu_\Theta\Theta\underline{\underline{G}} - \frac{2}{3}\rho k\underline{\underline{\mathrm{I}}},} \tag{2.25}$$

which can also be written in index notation using Eqs. (2.16)–(2.18) as

$$\boxed{\tau_{ij}^{RA} = -\rho\overline{u_i'u_j'} = 2\mu_t S_{ij} + \mu_\Theta\Theta G_{ij} - \frac{2}{3}\rho k\delta_{ij},} \tag{2.26}$$

where μ_Θ ($0 < |\mu_\Theta| \leq 1$) is the dimensionless scalar weight parameter to adjust the magnitude of the second term $\mu_\Theta\Theta\underline{\underline{G}}$ in conjunction with experimental and/or DNS data for different engineering problems. The sign of the weight parameter μ_Θ is negative ($\mu_\Theta < 0$) if the unit base vector $\mathbf{e}_3'$ in Eq. (2.22) has a negative sign. Otherwise, the scalar weight parameter μ_Θ is positive ($\mu_\Theta > 0$), because the sign of μ_Θ is related to the sign of the turbulent rotational motion in the momentum transfer [37]. The hypothesis on the anisotropic Reynolds stress tensor (2.25)–(2.26) proposed by Könözsy (2019) [6] is an anisotropic modification to the Boussinesq hypothesis (2.14) [4] based on the 3D similarity hypothesis of turbulent velocity fluctuations [8]. The new hypothesis on the anisotropic Reynolds stress tensor (2.25) takes into account the contribution of the mean rate-of-strain (deformation) tensor $2\mu_t\underline{\underline{S}}$, the local mechanically similar mean rotational motion $\mu_\Theta\Theta\underline{\underline{G}}$, and the turbulent kinetic energy $-(2/3)\rho k\underline{\underline{\mathrm{I}}}$ to the turbulent momentum transfer.

Using Eq. (2.20) for the definition of the principal turbulent shear stress Θ [6], [36], the anisotropic Reynolds stress tensor (2.25)–(2.26) can also be formulated as

$$\underline{\underline{\tau}}^{RA} = -\rho\overline{\mathbf{u}' \otimes \mathbf{u}'} = 2\mu_t\underline{\underline{S}} + \mu_\Theta\mu_t|\boldsymbol{\Omega}|\underline{\underline{G}} - \frac{2}{3}\rho k\underline{\underline{\mathrm{I}}}, \tag{2.27}$$

where the elements of the mean rate-of-strain tensor $\underline{\underline{S}}$ (2.16), the magnitude of the vorticity vector $|\boldsymbol{\Omega}|$ (2.13), the elements of the dimensionless transformed deviatoric similarity tensor $\underline{\underline{G}}$ (2.21) can be computed based on the local mean velocity components u_1, u_2, u_3; μ_Θ is an appropriately chosen dimensionless scalar weight parameter which can be

selected in conjunction with experimental and/or DNS data (e.g., $\mu_\Theta = -0.025$ [38]); ρ is a material property which is constant for incompressible flows; and the dynamic eddy viscosity coefficient μ_t and the turbulent kinetic energy k appear to be two unknowns. Therefore, to solve the Reynolds momentum Eq. (2.2) using the anisotropic Reynolds stress tensor $\underline{\underline{\tau}}^R = \underline{\underline{\tau}}^{RA}$ (2.25), a closure model has to be sought for the dynamic eddy viscosity μ_t and the turbulent kinetic energy k. Using the new hypothesis on the anisotropic Reynolds stress tensor (2.25), Könözsy (2019, 2021) [6], [37] proposed an anisotropic hybrid k-ω SST/STM closure model which is the result of the anisotropic modification to the k-ω SST engineering turbulence model of Menter (1992, 1994) [9], [10].

2.4 The anisotropic hybrid k-ω SST/STM closure model

For modelling incompressible turbulent flows in relation to engineering applications, the main steps of the theoretical development of an anisotropic hybrid k-ω SST/STM closure model have been summarised here based on the works of Könözsy (2019, 2021) [6], [37]. The new anisotropic Reynolds stress tensor $\underline{\underline{\tau}}^{RA}$ (2.25) has been employed as a modification to the k-ω SST closure model of Menter (1992, 1994) [9], [10] instead of using the Boussinesq hypothesis (2.14) [4] on the Reynolds stress tensor. The abbreviation STM stands for a Stochastic Turbulence Modelling approach [7], [38], because the elements of the dimensionless modified deviatoric similarity tensor $H^\star_{i,j}$ $(i, j = 1, 2, 3)$ (2.24) are computed based on a 3D STM approach in the dimensionless rotated deviatoric similarity tensor $\underline{\underline{G}}$ (2.21). Therefore, it is reasonable to name the modified anisotropic version of the k-ω SST closure model as anisotropic hybrid k-ω SST/STM closure model.

2.4.1 Anisotropic modification to the k-ω SST closure model

The k-ω SST engineering turbulence model of Menter [9], [10] is very well-documented and highly cited in the literature, because its formulation uses the advantageous features of the k-ω and k-ε closure models simultaneously and validated in comparison with many industrially relevant engineering applications with success [39]. Therefore, let us consider the mathematical derivation steps of the anisotropic modification to the k-ω SST closure model of Menter [9], [10] to formulate an engineering turbulence model using the new hypothesis based on Eq. (2.25) on the anisotropic Reynolds stress tensor $\underline{\underline{\tau}}^{RA}$. For incompressible turbulent flows, the continuity equation can be written as

$$\nabla \cdot \mathbf{u} = 0, \tag{2.28}$$

and the Reynolds momentum Eq. (2.2) can also be written with the use of the anisotropic Reynolds stress tensor $\underline{\underline{\tau}}^{RA}$ (2.25) which is framed below

$$\rho \frac{\partial \mathbf{u}}{\partial t} + \rho \mathbf{u} \cdot (\nabla \otimes \mathbf{u}) = \rho \mathbf{g} - \nabla p + \mu \nabla^2 \mathbf{u} + \boxed{\nabla \cdot \underline{\underline{\tau}}^{RA}}, \tag{2.29}$$

and the transport equation of the turbulent kinetic energy k [6], [37] is

$$\rho\frac{\partial k}{\partial t}+\rho(\mathbf{u}\cdot\nabla)k=\boxed{\underline{\underline{\tau}}^{RA}\cdot\cdot(\nabla\otimes\mathbf{u})}-\rho\beta^{\star}\omega k+\nabla\cdot\left[(\mu+\sigma_k\rho\nu_t)\nabla k\right], \tag{2.30}$$

and the specific dissipation rate $\omega=\varepsilon_k/(\beta^{\star}k)$ transport equation [6], [37] is

$$\rho\frac{\partial\omega}{\partial t}+\rho(\mathbf{u}\cdot\nabla)\omega=\boxed{\frac{\gamma}{\nu_t}\left[\underline{\underline{\tau}}^{RA}\cdot\cdot(\nabla\otimes\mathbf{u})\right]}-\rho\beta\omega^2+$$

$$+\nabla\cdot\left[(\mu+\sigma_\omega\rho\nu_t)\nabla\omega\right]+2\rho(1-F_1)\sigma_{\omega2}\frac{1}{\omega}\nabla k\cdot\nabla\omega, \tag{2.31}$$

where the symbol '$\cdot\cdot$' denotes the double dot scalar product of two second-rank tensors, and the anisotropic Reynolds stress tensor $\underline{\underline{\tau}}^{RA}$ (2.25) proposed by Könözsy (2019) [6] is

$$\boxed{\underline{\underline{\tau}}^{RA}=-\rho\overline{\mathbf{u}'\otimes\mathbf{u}'}=2\mu_t\underline{\underline{S}}+\mu_\Theta\Theta\underline{\underline{G}}-\frac{2}{3}\rho k\underline{\underline{\mathbf{I}}}.} \tag{2.32}$$

We can see from Eqs. (2.28)–(2.31) that the anisotropic Reynolds stress tensor $\underline{\underline{\tau}}^{RA}$ (2.32) appears a) in the source term of the Reynolds momentum Eq. (2.29), b) in the production term P_k^A of turbulent kinetic energy k Eq. (2.30), and c) in the production term P_ω^A of the specific dissipation rate ω Eq. (2.31), respectively. These framed terms are different compared to the original formulation of the k-ω SST model of Menter [9], [10]. In the anisotropic Reynolds stress tensor $\underline{\underline{\tau}}^{RA}$ Eq. (2.32), the dynamic eddy viscosity μ_t (2.15) can be computed by the vorticity based approximation proposed by Menter [9], [10] as

$$\mu_t=\rho\nu_t=\frac{\rho a_1 k}{\max(a_1\omega,|\mathbf{\Omega}|F_2)}, \tag{2.33}$$

where $0.3\leq a_1\leq 0.31$ is a constant [9], [36], [40], the turbulent kinetic energy k and the specific dissipation rate ω are obtained from the numerical solution of the transport Eqs. (2.30)–(2.31), the local magnitude of the vorticity vector $|\mathbf{\Omega}|$ can be computed based on Eq. (2.13), and F_2 is Menter's second blending function [10] which can be expressed by

$$F_2=\tanh\left[\max\left(\frac{2\sqrt{k}}{\beta^{\star}\omega y};\frac{500\nu}{\omega y^2}\right)^2\right]. \tag{2.34}$$

where ν is the kinematic viscosity of the fluid, $\beta^{\star}=0.09$ is a constant [41]–[43], and y is the distance to the next surface [9], [10], [23]. Menter et al. (2003) [23] also proposed a rate-of-strain tensor magnitude $|\underline{\underline{S}}|$ based formulation for the dynamic eddy viscosity coefficient μ_t. In the context of the anisotropic hybrid k-ω SST/STM closure model, the vorticity formulation-based dynamic eddy viscosity μ_t (2.33) was implemented in [38] to be consistent with the vorticity formulation-based second term $\mu_\Theta\Theta\underline{\underline{G}}$ in Eq. (2.32). In

the anisotropic Reynolds stress tensor (2.32), $\mu_\Theta = -0.025$ is a constant dimensionless scalar weight parameter which was adjusted based on experimental data in conjunction with different academic benchmarks problems and engineering applications in [44], [45]. In the turbulent kinetic energy dissipation term $-\rho\beta^\star\omega k$ which is the second term on the right-hand side of the turbulent kinetic energy k transport Eq. (2.30), the $\beta^\star = 0.09$ is a closure constant; and in the dissipation term $-\rho\beta\omega^2$ of specific dissipation rate ω transport Eq. (2.31), β is a function which can be expressed [10] by

$$\beta = \beta_1 F_1 + \beta_2 (1 - F_1) = 0.075 \cdot F_1 + 0.0828 \cdot (1 - F_1), \tag{2.35}$$

where $\beta_1 = 0.075$ and $\beta_2 = 0.0828$ are given by Menter [10] and Jones & Launder [43], respectively; where F_1 is Menter's first blending function which can be written [23] as

$$F_1 = \tanh\left\langle \left\{ \min\left[\max\left(\frac{\sqrt{k}}{\beta^\star \omega y}; \frac{500\nu}{\omega y^2} \right); \frac{4\sigma_{\omega 2}\rho k}{CD_{k\omega} y^2} \right] \right\}^4 \right\rangle, \tag{2.36}$$

where $\sigma_{\omega 2} = 0.856$ closure constant is taken from Jones & Launder [43], $\kappa = 0.41$ is the von Kármán constant; and the effect of the cross-diffusion in the last term on the right-hand side of the specific dissipation rate ω Eq. (2.31) is taken into account [23] by

$$CD_{k\omega} = \max\left[\frac{2\rho\sigma_{\omega 2}}{\omega} \cdot \left(\frac{\partial k}{\partial x_1}\frac{\partial \omega}{\partial x_1} + \frac{\partial k}{\partial x_2}\frac{\partial \omega}{\partial x_2} + \frac{\partial k}{\partial x_3}\frac{\partial \omega}{\partial x_3} \right); 10^{-10} \right]. \tag{2.37}$$

The γ closure function appears in the first term on the right-hand side of the specific dissipation rate ω transport Eq. (2.31) which represents the production term P_ω^A of the specific dissipation rate ω and can be computed [37] by

$$\gamma = \gamma_1 F_1 + \gamma_2 (1 - F_1) = 0.5531666 \cdot F_1 + 0.4403546 \cdot (1 - F_1), \tag{2.38}$$

where γ_1 and γ_2 constants can be related to other known closure constants [9], [10] as

$$\gamma_1 = \frac{\beta_1}{\beta^\star} - \frac{\sigma_{\omega 1}\kappa^2}{\sqrt{\beta^\star}}, \qquad \gamma_2 = \frac{\beta_2}{\beta^\star} - \frac{\sigma_{\omega 2}\kappa^2}{\sqrt{\beta^\star}}. \tag{2.39}$$

The σ_k and σ_ω closure functions appear in the diffusion terms D_k and D_ω of the turbulent kinetic energy k and specific dissipation rate ω transport Eqs. (2.30) and (2.31), respectively; and their numerical values can be computed [9], [10], [23] by

$$\sigma_k = \sigma_{k1} F_1 + \sigma_{k2} (1 - F_1) = 0.85 \cdot F_1 + (1 - F_1), \tag{2.40}$$

$$\sigma_\omega = \sigma_{\omega 1} F_1 + \sigma_{\omega 2} (1 - F_1) = 0.5 \cdot F_1 + 0.856 \cdot (1 - F_1), \tag{2.41}$$

where $\sigma_{\omega 1} = 0.5$ was given by Menter [10]. We can see that the dynamic eddy viscosity μ_t (2.33) and the closure functions β, γ, σ_k, σ_ω defined by Eqs. (2.35), (2.38), (2.40),

(2.41) are related to Menter's second F_2 (2.34) and first F_1 (2.36) blending functions, respectively, to ensure that the anisotropic hybrid k-ω SST/STM closure model also uses the advantageous features of the k-ω and k-ε engineering turbulence models similar to the k-ω SST/STM model of Menter [9], [10]. To obtain a mathematically consistent formulation of the anisotropic hybrid k-ω SST/STM closure model, the tensor divergence of the anisotropic Reynolds stress tensor $\underline{\underline{\tau}}^{RA}$ (2.32) in the Reynolds momentum Eq. (2.29) and the production terms P_k^A, P_ω^A in the k and ω transport Eqs. (2.30) and (2.31)—where the anisotropic Reynolds stress tensor $\underline{\underline{\tau}}^{RA}$ (2.32) appears—have to be derived next.

2.4.2 Divergence of the anisotropic Reynolds stress tensor

To obtain the final mathematical form of the Reynolds momentum equation (2.29), the divergence of the new anisotropic Reynolds stress tensor $\underline{\underline{\tau}}^{RA}$ (2.32) has to be derived which leads to the momentum equation of the anisotropic hybrid k-ω SST/STM closure model. Using the expression of the symmetrical anisotropic Reynolds stress tensor $\underline{\underline{\tau}}^{RA}$ (2.32), the tensor divergence can be derived [6], [37] as follows:

$$\nabla\cdot\underline{\underline{\tau}}^{RA}=\nabla\cdot\left(2\mu_t\underline{\underline{S}}+\mu_\Theta\Theta\underline{\underline{G}}-\frac{2}{3}\rho k\underline{\underline{\mathrm{I}}}\right)=\nabla\cdot\left\{2\mu_t\frac{1}{2}\left[(\nabla\otimes\mathbf{u})+(\nabla\otimes\mathbf{u})^T\right]+\mu_\Theta\Theta\underline{\underline{G}}-\frac{2}{3}\rho k\underline{\underline{\mathrm{I}}}\right\}=$$

$$=\nabla\cdot\left\{\rho\nu_t\left[(\nabla\otimes\mathbf{u})+(\nabla\otimes\mathbf{u})^T\right]+\mu_\Theta\Theta\underline{\underline{G}}-\frac{2}{3}\rho k\underline{\underline{\mathrm{I}}}\right\}=\nabla\cdot\left\{\rho\nu_t\left[(\nabla\otimes\mathbf{u})+(\nabla\otimes\mathbf{u})^T\right]+\mu_\Theta\Theta\underline{\underline{G}}\right\}$$

$$-\frac{2}{3}\rho\nabla\cdot\left(k\underline{\underline{\mathrm{I}}}\right)=\nabla\cdot\left\{\rho\nu_t\left[(\nabla\otimes\mathbf{u})+(\nabla\otimes\mathbf{u})^T\right]+\mu_\Theta\Theta\underline{\underline{G}}\right\}-\frac{2}{3}\rho\underbrace{\left(\underline{\underline{\mathrm{I}}}\cdot\nabla k\right)}_{=\nabla k}-\frac{2}{3}\rho k\cdot\underbrace{\left(\nabla\cdot\underline{\underline{\mathrm{I}}}\right)}_{=\mathbf{0}}=$$

$$=\nabla\cdot\left\{\rho\nu_t\left[(\nabla\otimes\mathbf{u})+(\nabla\otimes\mathbf{u})^T\right]+\mu_\Theta\Theta\underline{\underline{G}}\right\}-\frac{2}{3}\rho\nabla k=$$

$$=\sum_{j=1}^{3}\left\{\sum_{i=1}^{3}\frac{\partial}{\partial x_i}\left[\rho\nu_t\left(\frac{\partial u_j}{\partial x_i}+\frac{\partial u_i}{\partial x_j}\right)+\mu_\Theta\Theta G_{ij}\right]\cdot\mathbf{e}_j\right\}-\frac{2}{3}\rho\sum_{i=1}^{3}\left(\frac{\partial k}{\partial x_i}\cdot\mathbf{e}_i\right),\tag{2.42}$$

where the divergence of the unit tensor $\underline{\underline{\mathrm{I}}}$ is equal to zero, the dynamic eddy viscosity $\mu_t=\rho\nu_t$ and the principal Reynolds shear stress Θ can be computed based on Eqs. (2.33) and (2.20), the value of the scalar weight parameter $\mu_\Theta=-0.025$ was calibrated by Könözsy (2021) [38], and the elements of the dimensionless rotated deviatoric similarity tensor $\underline{\underline{G}}$ can be computed based on Eqs. (2.21)–(2.23). As a summary, the divergence of the anisotropic Reynolds stress tensor $\underline{\underline{\tau}}^{RA}$ (2.32) can be written in a vector form as

$$\boxed{\nabla\cdot\underline{\underline{\tau}}^{RA}=\nabla\cdot\left\{\rho\nu_t\left[(\nabla\otimes\mathbf{u})+(\nabla\otimes\mathbf{u})^T\right]+\mu_\Theta\Theta\underline{\underline{G}}\right\}-\frac{2}{3}\rho\nabla k.}\tag{2.43}$$

2.4.3 The modified turbulent kinetic energy k production term

The new anisotropic Reynolds stress tensor $\underline{\underline{\tau}}^{RA}$ (2.32) appears in the production term of the turbulent kinetic energy k Eq. (2.30). Therefore, the anisotropic modification to the production term in the turbulent kinetic energy k Eq. (2.30) of the k-ω SST engineering turbulence model of Menter [9], [10] is required to be derived. Let P_k^A denote the production term on the right-hand side of the turbulent kinetic energy k Eq. (2.30), and let us take the double dot inner product of the anisotropic Reynolds stress tensor $\underline{\underline{\tau}}^{RA}$ (2.32) and the velocity gradient tensor $\nabla \otimes \mathbf{u}$ which can be expressed [6], [37] by

$$
\begin{aligned}
P_k^A &= \underline{\underline{\tau}}^{RA} \cdot\cdot (\nabla \otimes \mathbf{u}) = \left(2\mu_t \underline{\underline{S}} + \mu_\Theta \Theta \underline{\underline{G}} - \frac{2}{3}\rho k \underline{\underline{\mathrm{I}}}\right) \cdot\cdot (\nabla \otimes \mathbf{u}) = \\
&= \left\{2\mu_t \frac{1}{2}\left[(\nabla \otimes \mathbf{u}) + (\nabla \otimes \mathbf{u})^T\right] + \mu_\Theta \Theta \underline{\underline{G}} - \frac{2}{3}\rho k \underline{\underline{\mathrm{I}}}\right\} \cdot\cdot (\nabla \otimes \mathbf{u}) = \\
&= \mu_t \left\{\left[(\nabla \otimes \mathbf{u}) + (\nabla \otimes \mathbf{u})^T\right] \cdot\cdot (\nabla \otimes \mathbf{u})\right\} + \mu_\Theta \Theta \left[\underline{\underline{G}} \cdot\cdot (\nabla \otimes \mathbf{u})\right] - \frac{2}{3}\rho k \underbrace{\left[\underline{\underline{\mathrm{I}}} \cdot\cdot (\nabla \otimes \mathbf{u})\right]}_{=\nabla \cdot \mathbf{u} = 0} = \\
&= \rho \nu_t \sum_{i=1}^{3}\left[\sum_{j=1}^{3}\left(\frac{\partial u_j}{\partial x_i} + \frac{\partial u_i}{\partial x_j}\right) \cdot \frac{\partial u_i}{\partial x_j}\right] + \mu_\Theta \Theta \sum_{i=1}^{3}\left(\sum_{j=1}^{3} G_{ij} \cdot \frac{\partial u_i}{\partial x_j}\right),
\end{aligned}
\tag{2.44}
$$

where the divergence-free constraint of the velocity field, i.e., the continuity Eq. (2.28) of incompressible fluid flows has been taken into account, the dynamic eddy viscosity $\mu_t = \rho \nu_t$ and the principal Reynolds shear stress Θ can be computed based on Eqs. (2.33) and (2.20), $\mu_\Theta = -0.025$ [38], and the elements of the rotated deviatoric similarity tensor $\underline{\underline{G}}$ can be computed based on Eqs. (2.21)–(2.23). As a summary, the anisotropic modification (2.44) to the production term P_k^A on the right-hand side of the turbulent kinetic energy k Eq. (2.30) leads to a mathematical expression in a vector form as follows:

$$
\boxed{P_k^A = \rho \nu_t \left\{\left[(\nabla \otimes \mathbf{u}) + (\nabla \otimes \mathbf{u})^T\right] \cdot\cdot (\nabla \otimes \mathbf{u})\right\} + \mu_\Theta \Theta \left[\underline{\underline{G}} \cdot\cdot (\nabla \otimes \mathbf{u})\right].}
\tag{2.45}
$$

2.4.4 The modified specific dissipation rate ω production term

The anisotropic Reynolds stress tensor $\underline{\underline{\tau}}^{RA}$ (2.32) with the factor of γ/ν_t appears in the production term of the specific dissipation rate ω Eq. (2.31). Therefore, the anisotropic modification to the production term in the specific dissipation rate ω Eq. (2.31) of the k-ω SST closure model of Menter [9], [10] is also required to be derived. Let P_ω^A denote the production term on the right-hand side of the specific dissipation rate ω Eq. (2.31), and let us take the double dot inner product of the anisotropic Reynolds stress tensor $\underline{\underline{\tau}}^{RA}$

(2.32) and the velocity gradient tensor $\nabla \otimes \mathbf{u}$ with the factor of γ/ν_t [6], [37], thus

$$
\begin{aligned}
P_\omega^A &= \frac{\gamma}{\nu_t}\left[\underline{\underline{\tau}}^{RA} \cdot\cdot (\nabla \otimes \mathbf{u})\right] = \frac{\gamma}{\nu_t}\left(2\mu_t \underline{\underline{S}} + \mu_\Theta \Theta \underline{\underline{G}} - \frac{2}{3}\rho k \underline{\underline{\mathrm{I}}}\right) \cdot\cdot (\nabla \otimes \mathbf{u}) = \\
&= \frac{\gamma}{\nu_t}\left\{2\mu_t \frac{1}{2}\left[(\nabla \otimes \mathbf{u}) + (\nabla \otimes \mathbf{u})^T\right] + \mu_\Theta \Theta \underline{\underline{G}} - \frac{2}{3}\rho k \underline{\underline{\mathrm{I}}}\right\} \cdot\cdot (\nabla \otimes \mathbf{u}) = \\
&= \frac{\gamma}{\nu_t}\left\{\rho \nu_t \left[(\nabla \otimes \mathbf{u}) + (\nabla \otimes \mathbf{u})^T\right] + \mu_\Theta \Theta \underline{\underline{G}} - \frac{2}{3}\rho k \underline{\underline{\mathrm{I}}}\right\} \cdot\cdot (\nabla \otimes \mathbf{u}) = \\
&= \frac{\gamma}{\nu_t}\rho \nu_t \left\{\left[(\nabla \otimes \mathbf{u}) + (\nabla \otimes \mathbf{u})^T\right] \cdot\cdot (\nabla \otimes \mathbf{u})\right\} + \frac{\gamma}{\nu_t}\mu_\Theta \Theta \left[\underline{\underline{G}} \cdot\cdot (\nabla \otimes \mathbf{u})\right] - \frac{2}{3}\frac{\gamma}{\nu_t}\rho k \underbrace{\left[\underline{\underline{\mathrm{I}}} \cdot\cdot (\nabla \otimes \mathbf{u})\right]}_{=\nabla \cdot \mathbf{u} = 0} = \\
&= \gamma\rho \left\{\left[(\nabla \otimes \mathbf{u}) + (\nabla \otimes \mathbf{u})^T\right] \cdot\cdot (\nabla \otimes \mathbf{u})\right\} + \frac{\gamma}{\nu_t}\mu_\Theta \Theta \left[\underline{\underline{G}} \cdot\cdot (\nabla \otimes \mathbf{u})\right] = \\
&= \gamma\rho \sum_{i=1}^{3}\left[\sum_{j=1}^{3}\left(\frac{\partial u_j}{\partial x_i} + \frac{\partial u_i}{\partial x_j}\right) \cdot \frac{\partial u_i}{\partial x_j}\right] + \frac{\gamma}{\nu_t}\mu_\Theta \Theta \sum_{i=1}^{3}\left(\sum_{j=1}^{3} G_{ij} \cdot \frac{\partial u_i}{\partial x_j}\right),
\end{aligned}
\tag{2.46}
$$

where the continuity Eq. (2.28) of incompressible fluid flows is taken into account again; the closure function γ, the kinematic eddy viscosity ν_t and the dominant turbulent shear stress Θ can be computed based on Eqs. (2.38), (2.33) and (2.20), respectively; the scalar weight parameter $\mu_\Theta = -0.025$ [38], and the elements of the transformed (rotated) deviatoric similarity tensor $\underline{\underline{G}}$ can be computed based on Eqs. (2.21)–(2.23). In the production term P_ω^A (2.46), the scalar factor γ/ν_t appears due to the modification to the dynamic eddy viscosity μ_t (2.33) proposed by Menter [9], [10]. As a summary, the anisotropic modification (2.46) to the production term P_ω^A on the right-hand side of the specific dissipation rate ω Eq. (2.31) leads to a mathematical expression in a vector form as follows:

$$
\boxed{P_\omega^A = \gamma\rho \left\{\left[(\nabla \otimes \mathbf{u}) + (\nabla \otimes \mathbf{u})^T\right] \cdot\cdot (\nabla \otimes \mathbf{u})\right\} + \frac{\gamma}{\nu_t}\mu_\Theta \Theta \left[\underline{\underline{G}} \cdot\cdot (\nabla \otimes \mathbf{u})\right].}
\tag{2.47}
$$

2.4.5 Governing equations of the hybrid k-ω SST/STM closure model

Using the divergence of the anisotropic Reynolds stress tensor $\underline{\underline{\tau}}^{RA}$ (2.43) along with the modified anisotropic production terms P_k^A (2.45) and P_ω^A (2.47) of the turbulent kinetic energy k and the specific dissipation rate ω Eqs. (2.30) and (2.31), respectively; the governing equations of the anisotropic hybrid k-ω SST/STM closure model can be formulated, thus a closed system of differential transport equations has been obtained in [6], [37]. Therefore, for incompressible turbulent flows, the mass conservation Eq. (2.28) is

$$
\nabla \cdot \mathbf{u} = 0,
\tag{2.48}
$$

and the Reynolds momentum Eq. (2.29) of the anisotropic hybrid k-ω SST/STM closure model—using the new hypothesis on the anisotropic Reynolds stress tensor $\underline{\underline{\tau}}^{RA}$ (2.32) and its tensor divergence (2.43)—can be written [6] as

$$\rho\frac{\partial \mathbf{u}}{\partial t}+\rho\mathbf{u}\cdot(\nabla\otimes\mathbf{u})=\rho\mathbf{g}-\nabla p+\mu\nabla^2\mathbf{u}+\nabla\cdot\left\{\rho\nu_t\left[(\nabla\otimes\mathbf{u})+(\nabla\otimes\mathbf{u})^T\right]+\mu_\Theta\Theta\underline{\underline{G}}\right\}-\frac{2}{3}\rho\nabla k, \tag{2.49}$$

and the turbulent kinetic energy k Eq. (2.30) of the anisotropic hybrid k-ω SST/STM closure model using the modified production term P_k^A (2.45) can be expressed [6] by

$$\rho\frac{\partial k}{\partial t}+\rho(\mathbf{u}\cdot\nabla)k=\rho\nu_t\left[(\nabla\otimes\mathbf{u})+(\nabla\otimes\mathbf{u})^T\right]\cdot\cdot(\nabla\otimes\mathbf{u})+$$

$$+\mu_\Theta\Theta\left[\underline{\underline{G}}\cdot\cdot(\nabla\otimes\mathbf{u})\right]-\rho\beta^\star\omega k+\nabla\cdot\left[(\mu+\sigma_k\mu_t)\nabla k\right], \tag{2.50}$$

and the specific dissipation rate ω Eq. (2.31) of the anisotropic hybrid k-ω SST/STM closure model using the modified production term P_ω^A (2.47) can be written [6] as

$$\rho\frac{\partial \omega}{\partial t}+\rho(\mathbf{u}\cdot\nabla)\omega=\gamma\rho\left\{\left[(\nabla\otimes\mathbf{u})+(\nabla\otimes\mathbf{u})^T\right]\cdot\cdot(\nabla\otimes\mathbf{u})\right\}+\frac{\gamma}{\nu_t}\mu_\Theta\Theta\left[\underline{\underline{G}}\cdot\cdot(\nabla\otimes\mathbf{u})\right]-\rho\beta\omega^2+$$

$$+\nabla\cdot\left[(\mu+\sigma_\omega\mu_t)\nabla\omega\right]+2\rho(1-F_1)\sigma_{\omega2}\frac{1}{\omega}\nabla k\cdot\nabla\omega, \tag{2.51}$$

where $\beta^\star=0.09$ is a constant [41]–[43], the scalar weight parameter $\mu_\Theta=-0.025$ is a constant calibrated by Könözsy [38], the dynamic eddy viscosity $\mu_t=\rho\nu_t$ and the principal turbulent shear stress Θ can be computed based on Eqs. (2.33) and (2.20), the elements of the rotated deviatoric similarity tensor $\underline{\underline{G}}$ can be computed based on Eqs. (2.21)–(2.23), Menter's closure functions σ_k, γ, β, σ_ω are relying on Eqs. (2.40), (2.38), (2.35) and (2.41), and $\sigma_{\omega2}=0.856$ is a constant [43]. For incompressible turbulent flows, the governing Eqs. (2.48)–(2.51) of the anisotropic hybrid k-ω SST/STM closure model have been formulated through the unification of the Boussinesq hypothesis (2.14) [4] and the 3D mechanical similarity theory of turbulent velocity fluctuations (2.19) [8] on the anisotropic Reynolds stress tensor $\underline{\underline{\tau}}^{RA}$ (2.32). The aim of the anisotropic modification to the Menter's isotropic k-ω SST engineering turbulence model was to develop a new anisotropic hybrid k-ω SST/STM closure model formulation to ensure an accurate numerical prediction of the Reynolds stress anisotropy in addition to the shear-stress transport. The additional source terms in the governing Eqs. (2.48)–(2.51) of the anisotropic hybrid k-ω SST/STM closure model have been implemented using User-Defined Functions (UDFs) in C programming language in the ANSYS-FLUENT environment and the corresponding computer code has fully been described in the publication of Könözsy [38]. Computational Fluid Dynamics (CFD) simulations for code verification and the anisotropic hybrid k-ω SST/STM closure model validation purposes using the Finite Volume Method (FVM) can also be found in the works of Könözsy [44], [45]. In this habilitation book-

let, the Reynolds stress distribution prediction capabilities of the anisotropic hybrid k-ω SST/STM closure model will be overviewed briefly through two practical test cases next.

2.5 Numerical prediction of anisotropic Reynolds stresses

In this Section[2], two industrially relevant benchmark problems are overviewed for numerically predicting the physical behaviour of anisotropic Reynolds stress distributions with the use of the anisotropic hybrid k-ω SST/STM closure model proposed in [18]. The simulation results for turbulent flows over a flat plate with zero pressure grandient and in a three-dimensional horizontal cylindrical pipe are compared to the k-ω SST model [9], [10], [23] and the experimental works of Klebanoff [46] and Laufer [47].

2.5.1 Reynolds stresses in a 2D turbulent flow over a flat plate

To investigate the accuracy of the anisotropic hybrid k-ω SST/STM closure model in terms of the prediction of Reynolds stress distributions, the turbulent flow over a $3.6576\,m$ long, $1.3716\,m$ wide and $0.00635\,m$ thick aluminium flat plate with zero pressure gradient has been considered here in conjunction with the wind tunnel experiments of Klebanoff [46]. In the experimental setup, the free-stream velocity was kept approximately $15.24\,m/s$ due to the presence of minor velocity fluctuations. The first $0.6096\,m$ of the plate surface was rough, because Klebanoff [46] used the method of artificial thickening of turbulent boundary layers which was proposed earlier by Klebanoff and Diehl [48]. According to Klebanoff [46], the experimental working station was placed at $x = 3.2004\,m$ from the origin O which was considered to be the pointed leading edge of the flat plate. The local Reynolds number was $Re_x = 4.2 \cdot 10^6$ and boundary layer thickness was $\delta_b = 0.0762\,m$ at the location of $x = 3.2004\,m$ where each physical quantity was measured perpendicular to the flat plate along the vertical direction y [46]. The Mach number Ma of the air flow in the wind tunnel was approximately equal to 0.05 which means that the density variation of the air was very small. Therefore, a constant density incompressible fluid flow has been considered in the numerical simulations. The dynamic viscosity μ_{ref} of the air was computed based on the Sutherland law and the reference static temperature was $T_{ref} = 253.65\,K$ [44]. Numerical simulations have been performed by using the ANSYS-FLUENT R19.1 software package with the implementation of the anisotropic hybrid k-ω SST/STM closure model through User-Defined Functions (UDFs) in C programming language [44]. The geometrical setup, i.e., the computational domain and the boundary conditions were aligned with the experimental setup of Klebanoff [46] which are shown

[2]Simulation results on the numerical prediction of anisotropic Reynolds stresses in the author's previously published work overviewed here in Section 2.5 were used with permission of Springer Nature BV, Switzerland, from the book entitled as "A New Hypothesis on the Anisotropic Reynolds Stress Tensor for Turbulent Flows", Author: László Könözsy, Volume II, Chapter 4, pp. 222-231, pp. 244-252; Chapter 5, pp. 362-364, pp. 370-376, 1st. Edition 2021; the permission conveyed through Copyright Clearance Center, Inc., https://www.copyright.com/

in Figure 2.1. Therefore, the average inlet velocity magnitude of $15.1012\,m/s$ has been adjusted that the air flow has to reach the magnitude of the free-stream velocity $15.24\,m/s$ at the location of $x = 3.2004\,m$. The level of the inlet and outlet turbulence intensities $0.02\,\%$ and the magnitude of the turbulent length scale $0.016002\,m$ have been specified based on a parametric study related to the wind tunnel experiments [44]. Klebanoff [46] used a No. 16 floor-sanding paper on the first $0.6096\,m$ of the plate wall and its roughness effect has been considered in the simulations with the wall roughness height of $0.008\,m$ [44]. Klebanoff [46] used the foot (1 foot = $0.3048\,m$) and inch (1 inch = $0.0254\,m$) length units of measure in his work which are also shown in Figure 2.1.

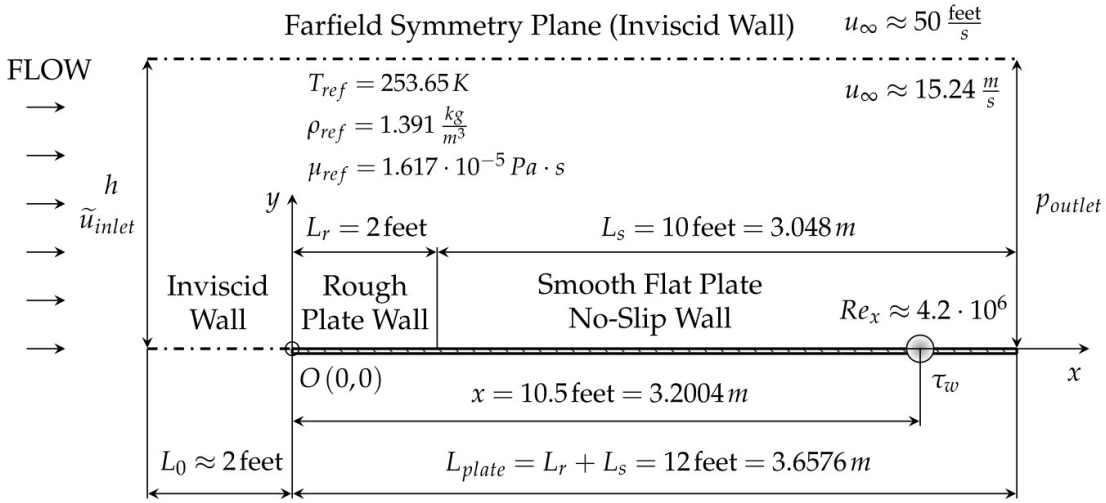

- Geometrical Data: $h = 4.5\,\text{feet} = 1.3716\,m$; $L_0 \approx 2\,\text{feet} = 0.6095939\,m$; $L_r = 2\,\text{feet} = 0.6096\,m$
- Boundary Values: $\widetilde{u}_{inlet} = 15.1012\,\frac{m}{s}$ (Velocity Inlet); $p_{outlet} = 101281.9\,Pa$ (Pressure Outlet)

Figure 2.1: Computational domain and boundary conditions of an incompressible turbulent air flow benchmark problem over a flat plate with zero pressure gradient in conjunction with the experimental work of Klebanoff [46], [44, p. 223][3]

Three different computational meshes such as coarse, medium and fine were employed in the CFD simulations with the numbers of points 35×25 (875), 137×97 (13 289) and 545×385 (209 825) [49] along with the dimensionless wall distance y^+ values of 0.2638320, 0.0648358 and 0.0159163 [44], respectively. For solving the governing Eqs. (2.48)–(2.51) of the anisotropic hybrid k-ω SST/STM closure model for incompressible turbulent flows, the coupled solver method with the pseudo-transient approach was employed—using the ANSYS-FLUENT R19.1 software package with a UDF C code

[3]Figure 2.1 used with permission of Springer Nature BV, Switzerland, from the book entitled as "A New Hypothesis on the Anisotropic Reynolds Stress Tensor for Turbulent Flows", Author: László Könözsy, Volume II, Chapter 4, p. 223, 1st. Edition 2021; the permission conveyed through Copyright Clearance Center, Inc., https://www.copyright.com/

implemented by Könözsy [38, pp. 178-213]—to obtain a fully-developed turbulent flow at the location of $x = 3.2004\,m$ of the flat plate wall. In terms of the spatial discretisation of the convective terms in the transport Eqs. (2.49)–(2.51), the second-order upwind scheme was used for solving the Reynolds momentum Eq. (2.49), and the first-order upwind scheme was employed for solving the turbulent kinetic energy k Eq. (2.50) and the specific dissipation rate ω Eq. (2.51). For the pressure field solution, a second-order approximation was employed in the framework of the pressure-velocity coupling (PVC) approach. The convergence criteria for each physical quantity were set to be equal to 10^{-6}. In the work of Könözsy (2021) [44, pp. 232–236], the impact of the computational mesh resolutions on the accuracy of the numerical simulations was investigated in conjunction with the dimensionless mean velocity distributions along the vertical direction y at the location of $x = 3.2004\,m$ in comparison with the experimental data of Klebanoff [46]. It has been found that the fine mesh with 209 825 computational points (see Figure 2.2) provided the most optimal resolution of the computational domain to obtain accurate numerical results for the dimensionless mean velocity profiles perpendicular to the plate wall at $x = 3.2004\,m$. The mean pressure and skin friction coefficient distributions along the flat plate wall, and the dimensionless turbulent energy production and dissipation profiles along the vertical coordinate y at the location of $x = 3.2004\,m$ were also predicted accurately against the wind tunnel experiments of Klebanoff [46]. One can find more details about these numerical studies in [44, pp. 222–244].

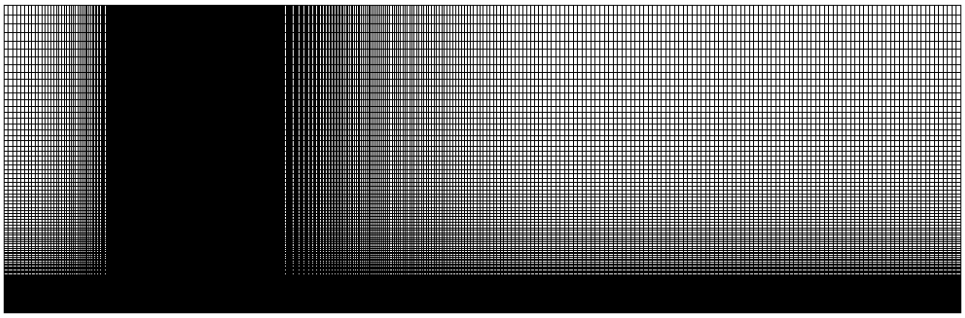

Figure 2.2: The fine mesh consists of 209 825 computational points [44, p. 224][4]

In this habilitation booklet, the CFD results obtained in conjunction with the Reynolds stress distributions along the vertical direction y at the location of $x = 3.2004\,m$ [44] against the experimental data of Klebanoff [46] are discussed here; because the Boussinesq hypothesis-based (2.14) [4] linear eddy viscosity URANS/RANS engineering turbulence models used in the industry are only capable of predicting the isotropic distribution of Reynolds stresses [5] which is a strong limitation of these models. How-

[4]Figure 2.2 used with permission of Springer Nature BV, Switzerland, from the book entitled as "A New Hypothesis on the Anisotropic Reynolds Stress Tensor for Turbulent Flows", Author: László Könözsy, Volume II, Chapter 4, p. 224, 1st. Edition 2021; the permission conveyed through Copyright Clearance Center, Inc., https://www.copyright.com/

ever, the linear eddy viscosity URANS/RANS turbulence models can capture accurately the mean velocity and pressure distributions which are relevant to industrial applications. Klebanoff [46] measured the specific Reynolds stress, i.e., turbulence intensity distributions along a perpendicular line at the location of $x = 3.2004\,m$. Relying on the experimental data obtained for the distribution of turbulence intensities, Klebanoff [46] found that the theory of local isotropy in the near-wall region is questionable, because the turbulent flow is anisotropic in this region in terms of Reynolds stress distributions (2.25). Therefore, the calibration of the scalar weight parameter μ_Θ in the anisotropic Reynolds stress tensor (2.25), the anisotropic scale factors $\lambda_{11}^\star$, $\lambda_{22}^\star$ along with the elements $H_{11}^\star$, $H_{22}^\star$ of the modified deviatoric similarity tensor $\underline{\underline{H}}^\star$ (2.24) was required related to the measurements of Klebanoff [46]. It has been found that the calibrated values of $\mu_\Theta = -0.025$, $\lambda_{11}^\star = -47.5$ and $\lambda_{22}^\star = -0.0065^{-1}$ led to the physically correct numerical values of $\mu_\Theta \lambda_{11}^\star H_{11}^\star = -1.2404$ and $\mu_\Theta \lambda_{22}^\star H_{22}^\star = 0.8036$ in which case $H_{11}^\star = -1.0446$ and $H_{22}^\star = 0.2089$ for two-dimensional fluid flows in the boundary layer [44]. The dimensionless specific Reynolds stresses, i.e., turbulence intensities can be computed [44] as

$$\frac{\mathrm{RMS11}}{u_\infty} = \frac{\sqrt{\overline{u_1' u_1'}}}{u_\infty} = \frac{1}{u_\infty} \cdot \sqrt{\frac{\left|\tau_{11}^{RA}\right|}{\rho_{ref}}}, \quad \text{and} \quad \frac{\mathrm{RMS22}}{u_\infty} = \frac{\sqrt{\overline{u_2' u_2'}}}{u_\infty} = \frac{1}{u_\infty} \cdot \sqrt{\frac{\left|\tau_{22}^{RA}\right|}{\rho_{ref}}}, \tag{2.52}$$

where the abbreviation RMS stands for a root-mean-square value; τ_{11}^{RA} and τ_{22}^{RA} are the first and second main diagonal elements of the anisotropic Reynolds stress tensor (2.26) which are the normal Reynolds stress components; u_∞ is the reference free-stream air velocity; and ρ_{ref} is the reference density of the air. The dimensionless principal Reynolds shear stress, i.e., dimensionless dominant turbulent shear stress can be computed [44], [46] as

$$\frac{2\left|\overline{u_1' u_2'}\right|}{u_\infty^2} = \frac{2}{u_\infty^2} \cdot \frac{\left|\tau_{12}^{RA}\right|}{\rho_{ref}}. \tag{2.53}$$

The dimensionless numerical values of the specific Reynolds stresses, i.e., RMS velocity fluctuations (2.52) and the principal turbulent shear stress (2.53) can be obtained from the CFD simulations with the numerical solution of the governing Eqs. (2.48)–(2.51). The comparison of the numerically predicted dimensionless RMS velocity fluctuations (2.52)—which are the dimensionless RMS specific normal Reynolds stresses (2.52)—with the experimental data of Klebanoff [46] is shown in Figure 2.3. It can be seen that the k-ω SST model [10] predicted identical dimensionless turbulence intensity profiles for each main diagonal elements of the Boussinesq hypothesis-based [4] Reynolds stress tensor (2.14) which means that the k-ω SST model [10] is an isotropic turbulence model and fails to predict the anisotropic behaviour of the Reynolds stress distributions (2.52). The anisotropic hybrid k-ω SST/STM closure model was capable of predicting the physically correct behaviour of the dimensionless specific Reynolds stress distributions (2.52) in comparison with the experimental data of Klebanoff [46], except in the very near-wall region ($y/\delta_b \leq 0.025$) which is shown in Figure 2.3. The reason could be that different

anisotropic scaling is required in the near-wall region compared to the anisotropic scaling used at $y/\delta_b > 0.025$ to predict accurately the measured peak values of the dimensionless RMS velocity fluctuations (2.52) which is indicated by the obtained numerical results. The obtained simulation results suggest that the unification of the Boussinesq hypothesis (2.14) [4] and the three-dimensional similarity theory of turbulent velocity fluctuations (2.19) [8] in conjunction with the new anisotropic Reynolds stress tensor (2.25) can lead to a further improvement in terms of the numerical prediction of the anisotropic RMS velocity fluctuations (2.52) in the context of RANS turbulence modelling. For incompressible turbulent flows, further investigation of the effect of the anisotropic scaling in the near-wall region has been carried out in a three-dimensional industrially relevant long horizontal cylindrical pipe which will be discussed briefly in Subsection 2.5.2.

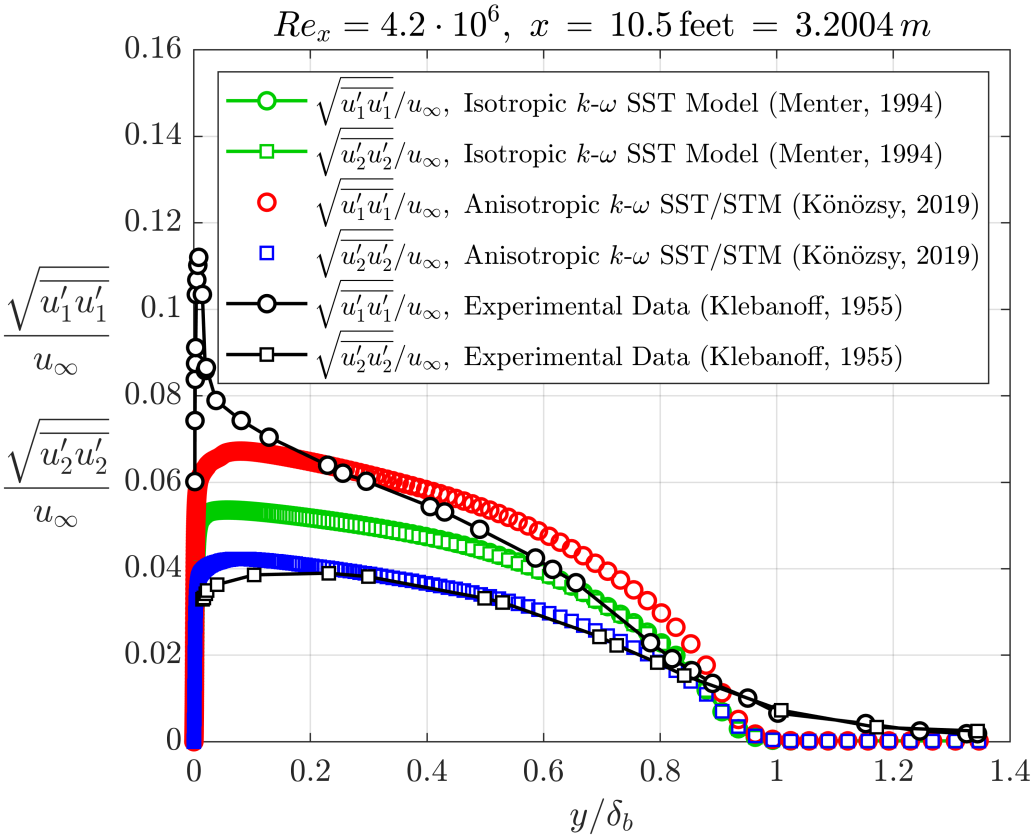

Figure 2.3: Comparison of numerically simulated dimensionless RMS specific Reynolds stress profiles (2.52) at $Re_x = 4.2 \cdot 10^6$ with the experimental data of Klebanoff [46][5]

[5]Figure 2.3 used with permission of Springer Nature BV, Switzerland, from the book entitled as "A New Hypothesis on the Anisotropic Reynolds Stress Tensor for Turbulent Flows", Author: László Könözsy, Volume II, Chapter 4, p. 247, 1st. Edition 2021; the permission conveyed through Copyright Clearance Center, Inc., https://www.copyright.com/

It can be seen in Figure 2.4 that the anisotropic hybrid k-ω SST/STM closure model inherited the advantageous features of the k-ω SST model of Menter [9], [10], [23] in terms of predicting the physically correct behaviour of the dimensionless principal Reynolds shear stress profile. It means that both RANS engineering turbulence models predicted correctly the dimensionless dominant turbulent shear stress distribution (2.53) along the vertical line y/δ_b with minor discrepancies against the experimental data in [46].

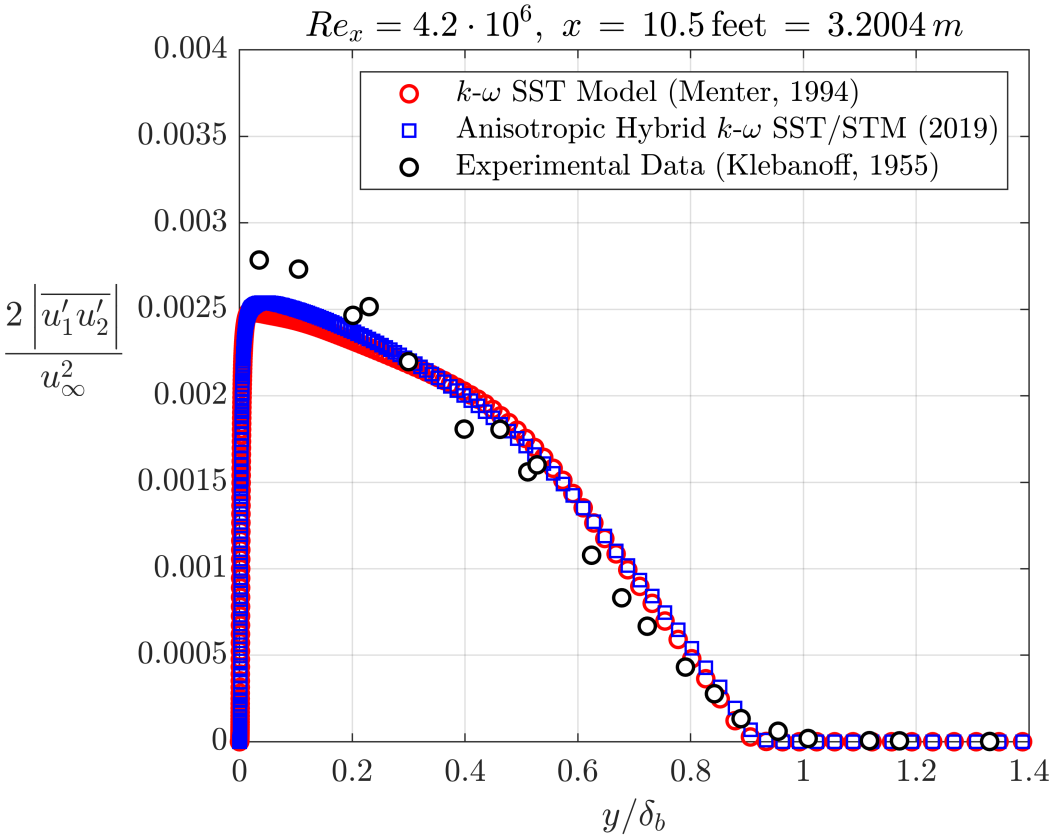

Figure 2.4: Comparison of numerically simulated dimensionless principal Reynolds shear stress profiles (2.53) at $Re_x = 4.2 \cdot 10^6$ with the experimental data of Klebanoff [46][6]

In terms of the dimensionless RMS velocity fluctuations (2.52), the specific Reynolds stress RMS11/u_∞ was slightly overestimated within the boundary layer thickness of $0.3 \lessapprox y/\delta_b \lessapprox 0.9$ (see Figure 2.3). It could be due to the fact that the free-stream velocity u_∞ exhibited approximately $\pm 1.2\%$ small fluctuations in the wind tunnel [44]; therefore, the magnitude of the free-stream velocity u_∞ could vary between $15.05712\,m/s$ and

[6]Figure 2.4 used with permission of Springer Nature BV, Switzerland, from the book entitled as "A New Hypothesis on the Anisotropic Reynolds Stress Tensor for Turbulent Flows", Author: László Könözsy, Volume II, Chapter 4, p. 248, 1st. Edition 2021; the permission conveyed through Copyright Clearance Center, Inc., https://www.copyright.com/

15.42288 m/s [44]. According to Klebanoff and Diehl [48], the development length of approximately 4.32816 m is required for the boundary layer to become fully-developed along the smooth surface of a flat plate wall. This experimental observation indicates that it is worth considering a slightly longer flat plate in the numerical simulations. Therefore, Könözsy [44, pp. 249-252] also investigated a slightly different computational configuration of the boundary layer flow with a 0.6095939 m longer flat plate than the original flat plate length of the experimental setup of Klebanoff [46] in which simulation the total length of the flat plate was 4.2671939 m. For simulating the spatial evolution of the boundary layer development along the solid wall and within the boundary layer thickness of 0.0762 m measured by Klebanoff [46], the height of the domain was reduced from 1.3716 m to 0.1143 m. The inlet velocity of 13.949 m/s was adjusted based on the free-stream velocity of 15.07 m/s by taking into account 1.2% free-stream velocity fluctuation in which case the corresponding local Reynolds number was equal to $Re_x = 4.15 \cdot 10^6$ at the location of $x = 3.2004\,m$. The configuration of the simulation example setup for the extended computational domain with the boundary conditions is shown in Figure 2.5.

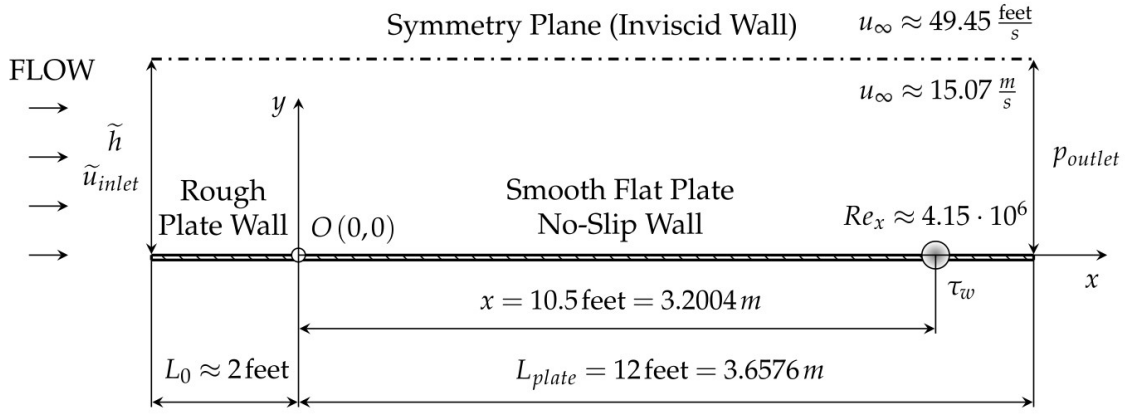

- Geometrical Data: $\widetilde{h} = 4.5\,\text{inches} = 0.1143\,m$; $L_0 \approx 2\,\text{feet} = 0.6095939\,m$
- Boundary Values: $\widetilde{u}_{inlet} = 13.949\ \frac{m}{s}$ (Velocity Inlet); $p_{outlet} = 101281.9\,Pa$ (Pressure Outlet)

Figure 2.5: Extended computational domain and boundary conditions for modelling the boundary layer development with a rough wall in front of the smooth wall [44, p. 250][7]

For the extended length of the two-dimensional computational domain (see Figure 2.5), the numerical simulation was performed with the anisotropic hybrid k-ω SST/STM closure model [6] on the fine mesh using 209 825 computational points (see Figure 2.2). The coupled solver with the pseudo-transient approach was employed with the same spatial

[7]Figure 2.5 used with permission of Springer Nature BV, Switzerland, from the book entitled as "A New Hypothesis on the Anisotropic Reynolds Stress Tensor for Turbulent Flows", Author: László Könözsy, Volume II, Chapter 4, p. 250, 1st. Edition 2021; the permission conveyed through Copyright Clearance Center, Inc., https://www.copyright.com/

discretisation schemes of the convective terms along with the previously calibrated numerical values of $\mu_\Theta \lambda_{11}^\star H_{11}^\star = -1.2404$ and $\mu_\Theta \lambda_{22}^\star H_{22}^\star = 0.8036$ with $H_{11}^\star = -1.0446$ and $H_{22}^\star = 0.2089$ for 2D boundary layer flows related to the modified deviatoric similarity tensor $\underline{\underline{H}}^\star$ (2.24) as discussed above in the case of the original Klebanoff problem [46]. When the length of the smooth plate was extended to $3.6576\,m$ (see Figure (2.5)), the anisotropic hybrid k-ω SST/STM closure model [6] was capable of predicting accurately the dimensionless RMS specific Reynolds stress profiles (2.52) at $Re_x = 4.15 \cdot 10^6 \approx 4.2 \cdot 10^6$ against the experimental data in [46], except in the very near-wall region ($y/\delta_b < 0.025$) which is shown in Figure 2.6. The obtained numerical results indicate that the anisotropic scaling was calibrated correctly for two-dimensional boundary layer flows in conjunction with the new anisotropic Reynolds stress tensor (2.25) proposed in [6]. The near-wall anisotropic scaling will be discussed next for three-dimensional turbulent flows in a long cylindrical pipe in comparison with the experimental data of Laufer [47].

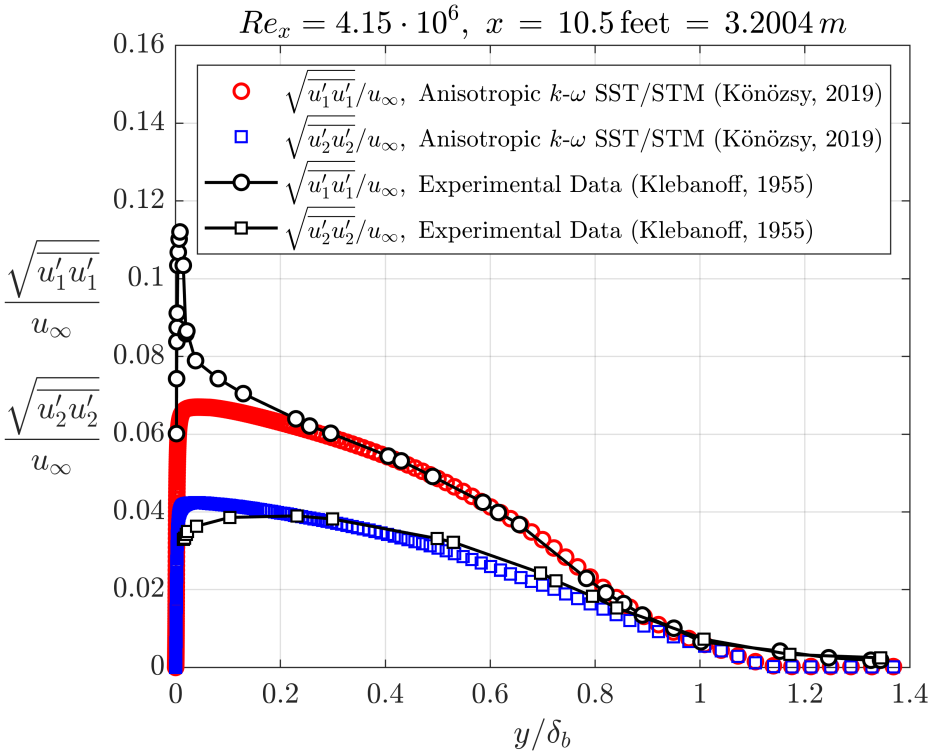

Figure 2.6: Comparison of the simulated dimensionless RMS specific Reynolds stress profiles (2.52) at $Re_x = 4.15 \cdot 10^6 \approx 4.2 \cdot 10^6$ with the experimental data of Klebanoff [46][8]

[8]Figure 2.6 used with permission of Springer Nature BV, Switzerland, from the book entitled as "A New Hypothesis on the Anisotropic Reynolds Stress Tensor for Turbulent Flows", Author: László Könözsy, Volume II, Chapter 4, p. 251, 1st. Edition 2021; the permission conveyed through Copyright Clearance Center, Inc., https://www.copyright.com/

2.5.2 Reynolds stresses in a 3D turbulent flow in a cylindrical pipe

Laufer [47] experimentally investigated fully-developed turbulent air flows in a $7.62\,m$ long steel pipe connected to a $4.8768\,m$ long seamless brass tube with a hydraulic diameter of $D = 0.246888\,m$, i.e., the total length of the pipe was $12.4968\,m$. The first $0.762\,m$ of the pipe was roughened with the use of a gluing floor-sanding paper [47], [44, pp. 288-289]. Laufer [47] also used the experimental method of artificial thickening of boundary layers which was proposed earlier by Klebanoff and Diehl [48]. The rest of the $11.7348\,m$ long pipe wall was smooth. Therefore, the surface roughness of the first $0.762\,m$ of the pipe has been taken into account in the simulations with the roughness height of $0.008\,m$ where the Dirichlet-type no-slip boundary condition was imposed on the cylindrical wall. To ensure the spatial evolution of a fully-developed turbulent flow at the pipe outlet, an extended pipe length of $17.28216\,m$ was used in the simulations. The three-dimensional horizontal cylindrical pipe used in the simulations is shown in Figure 2.7.

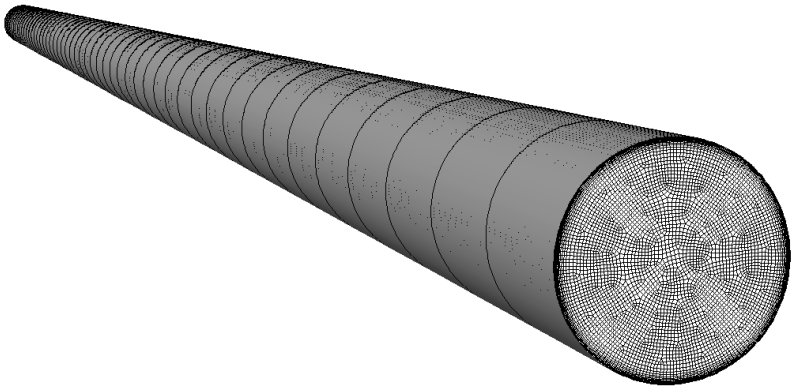

Figure 2.7: Unstructured computational mesh consists of 461 958 cells for simulating turbulent flows in a three-dimensional horizontal cylindrical pipe [45, p. 362][9]

The measurements in [47] were conducted at Reynolds numbers of $Re_m = 50\,000$ and $Re_m = 500\,000$ which were defined by the maximum velocity magnitudes u_{max} of $3.048\,m/s$ and $30.48\,m/s$ reached along the centre-line of the cylindrical pipe. The corresponding average inlet velocity magnitudes are $2.5785\,m/s$ at $Re_m = 50\,000$ and $26.520\,m/s$

[9]Figure 2.7 used with permission of Springer Nature BV, Switzerland, from the book entitled as "A New Hypothesis on the Anisotropic Reynolds Stress Tensor for Turbulent Flows", Author: László Könözsy, Volume II, Chapter 5, p. 362, 1st. Edition 2021; the permission conveyed through Copyright Clearance Center, Inc., https://www.copyright.com/

at $Re_m = 500\,000$ with the air density of $\rho_{ref} = 1.204\,kg/m^3$ and the dynamic viscosity $\mu_{ref} = 1.812055 \cdot 10^{-5}\,Pa \cdot s$ of the air at the static temperature of $T_{ref} = 293\,K$. The outlet pressure was equal to the atmospheric pressure of $101325\,Pa$. The levels of the inlet and outlet turbulence intensities of 0.04 % and 4 % were adjusted based on the experimental work in [47]. The three-dimensional anisotropic specific Reynolds stress distributions, i.e., turbulence intensities were measured by Laufer [47] inside the pipe from $0.0508\,m$ to $0.1016\,m$ far from the pipe outlet ($z \geq 50D$) [45, pp. 370] which can be computed as

$$\frac{\sqrt{\overline{u_1' u_1'}}}{u_\tau} = \frac{1}{u_\tau} \cdot \sqrt{\frac{\left|\tau_{11}^{RA}\right|}{\rho_{ref}}}, \quad \frac{\sqrt{\overline{u_2' u_2'}}}{u_\tau} = \frac{1}{u_\tau} \cdot \sqrt{\frac{\left|\tau_{22}^{RA}\right|}{\rho_{ref}}}, \quad \frac{\sqrt{\overline{u_3' u_3'}}}{u_\tau} = \frac{1}{u_\tau} \cdot \sqrt{\frac{\left|\tau_{33}^{RA}\right|}{\rho_{ref}}}, \tag{2.54}$$

where τ_{11}^{RA}, τ_{22}^{RA} and τ_{33}^{RA} are the first-, second- and third main diagonal elements of the anisotropic Reynolds stress tensor (2.26), and u_τ is the shear velocity. For modelling three-dimensional incompressible turbulent air flows in a horizontal cylindrical pipe in conjunction with the measurements of Laufer [47], the governing Eqs. (2.48)–(2.51) of the anisotropic hybrid k-ω SST/STM closure model were solved with the coupled solver method with the pseudo-transient approach using the ANSYS-FLUENT R19.1 software package with a UDF C code implemented by Könözsy [38, pp. 178-213]. The coupled solver with the pseudo-transient approach was capable of predicting most accurately the spatial evolution of the air flow along the length of the there-dimensional cylindrical pipe. In terms of the spatial discretisation of the convective terms in the governing transport Eqs. (2.49)–(2.51), the second-order upwind scheme was employed for solving the Reynolds momentum Eq. (2.49), the turbulent kinetic energy k Eq. (2.50) and the specific dissipation rate ω Eq. (2.51). The convergence criteria were set to be equal to 10^{-5} and 10^{-7} for the continuity Eq. (2.48) and the transport Eqs. (2.49)–(2.51), respectively. For three-dimensional incompressible high Reynolds number turbulent flows, the calibrated values of $\mu_\Theta = -0.025$, $\lambda_{11}^\star = -57.5$, $\lambda_{22}^\star = -59.5$ and $\lambda_{33}^\star = -77.5$ resulted the physically correct numerical values of $\mu_\Theta \lambda_{11}^\star H_{11}^\star = -1.0511$, $\mu_\Theta \lambda_{22}^\star H_{22}^\star = 0.7769$ and $\mu_\Theta \lambda_{33}^\star H_{33}^\star = 0.4047$ where $H_{11}^\star = -0.7312$, $H_{22}^\star = 0.5223$ and $H_{33}^\star = 0.2089$ in Eq. (2.24) [45, p. 363]. Preliminary CFD simulations were performed on three unstructured meshes such as coarse, medium and fine using 32 219, 193 902 and 461 958 computational cells, respectively. In this habilitation booklet, those results are overviewed for the dimensionless anisotropic specific Reynolds stress distributions (2.54) which were obtained on the fine mesh with $y^+ \approx 0.02$ in comparison with the measurements of Laufer [47]. The simulation results obtained with the anisotropic hybrid k-ω SST/STM closure model [6] are compared to the results obtained with the k-ω SST model of Menter [9], [10], [23] in addition to the comparison with the experimental data in [47]. For both RANS engineering turbulence models employed here, 382 iteration steps were required to predict the fully-developed RMS velocity fluctuation profiles (2.54) and in each iteration step beyond that, the RMS velocity fluctuations (2.54) changed only to a negligible extent [45, p. 370].

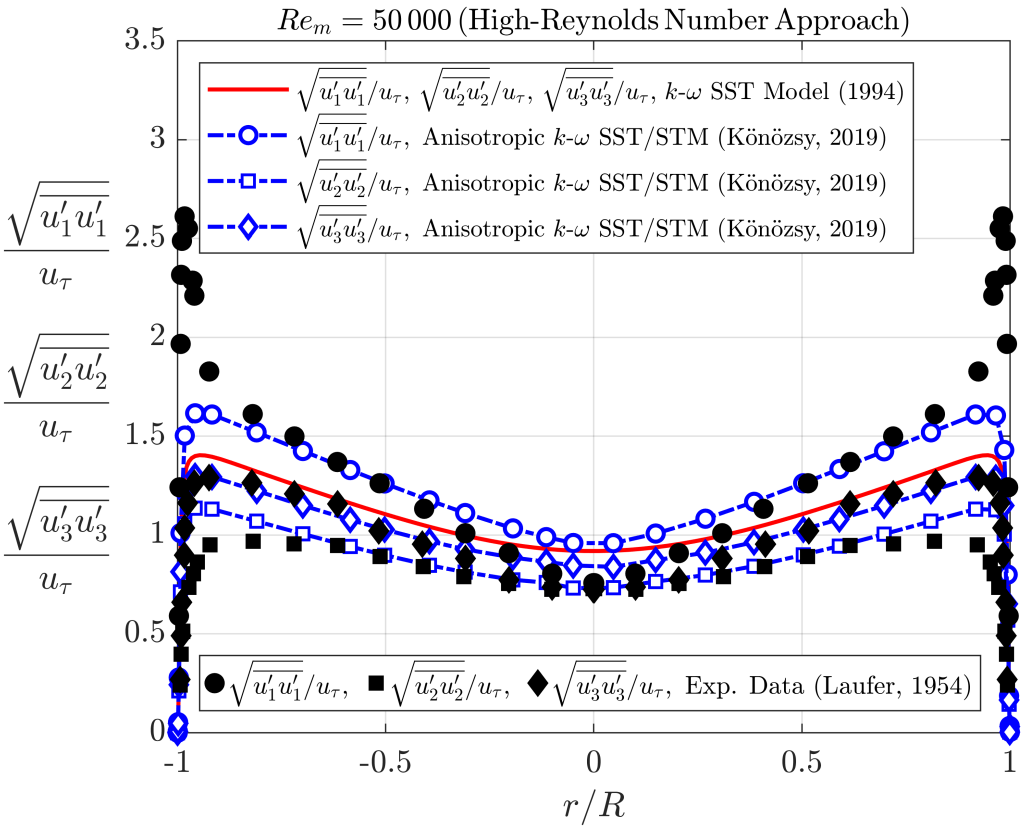

Figure 2.8: Comparison of the simulated fully-developed dimensionless RMS specific Reynolds stress profiles at Re_m = 50000 with the experimental data of Laufer [47][10]

For modelling three-dimensional turbulent flows in a horizontal cylindrical pipe at Re_m = 50000 and Re_m = 500000, a high Reynolnds number turbulence modelling approach was employed in conjunction with the anisotropic hybrid k-ω SST/STM closure model [6] which was described in Section 2.4. Using this approach at Re_m = 50000, it can be seen in Figure 2.8 that the anisotropic hybrid k-ω SST/STM closure model [6] predicted accurately the physical behaviour of the dimensionless RMS specific Reynolds stress profiles (2.54) along the dimensionless radial coordinate r/R against the measurements of Laufer [47] at $z \geq 50D$ [$y^+(r) \gtrapprox 65$], except very near to the cylindrical wall of the pipe [$y^+(r) \lessapprox 65$]; where the coordinate z points in the direction of the pipe axis. The k-ω SST model of Menter [9], [10], [23] predicted the same dimensionless RMS velocity fluctuations (2.54) for each main diagonal element of the Boussinesq hypothesis-based [4] Reynolds stress tensor (2.14) which results from the isotropic nature of the k-ω SST

[10]Figure 2.8 used with permission of Springer Nature BV, Switzerland, from the book entitled as "A New Hypothesis on the Anisotropic Reynolds Stress Tensor for Turbulent Flows", Author: László Könözsy, Volume II, Chapter 5, p. 372, 1st. Edition 2021; the permission conveyed through Copyright Clearance Center, Inc., https://www.copyright.com/

model [9], [10], [23] and is shown with a red continuous line in Figure 2.8. To capture the near-wall dimensionless RMS specific Reynolds stress distributions (2.54), the combination of the low Reynolds number turbulence modelling approach in [50] with a high Reynolds number anisotropic scaling can improve further the computational accuracy of the dimensionless RMS velocity fluctuations (2.54) in the near-wall region at $y^+(r) \lessapprox 65$. The calibrated values of $\mu_\Theta = -0.025$, $\lambda^\star_{11} = -159.5$, $\lambda^\star_{22} = -109.5$ and $\lambda^\star_{33} = -97.5$ resulted the numerical values of $\mu_\Theta \lambda^\star_{11} H^\star_{11} = -2.9157$, $\mu_\Theta \lambda^\star_{22} H^\star_{22} = 1.4298$ and $\mu_\Theta \lambda^\star_{33} H^\star_{33} = 0.5092$ where $H^\star_{11} = -0.7312$, $H^\star_{22} = 0.5223$ and $H^\star_{33} = 0.2089$ in Eq. (2.24) [45, p. 371] leading to the physically correct behaviour of the RMS specific Reynolds stress distributions (2.54) in the near-wall region [$y^+(r) \lessapprox 65$] at $Re_m = 50\,000$ (see Figure 2.9). The low Reynolds number turbulence modelling approach in conjunction with the k-ω type two-equation RANS turbulence models are well documented in [42], [50].

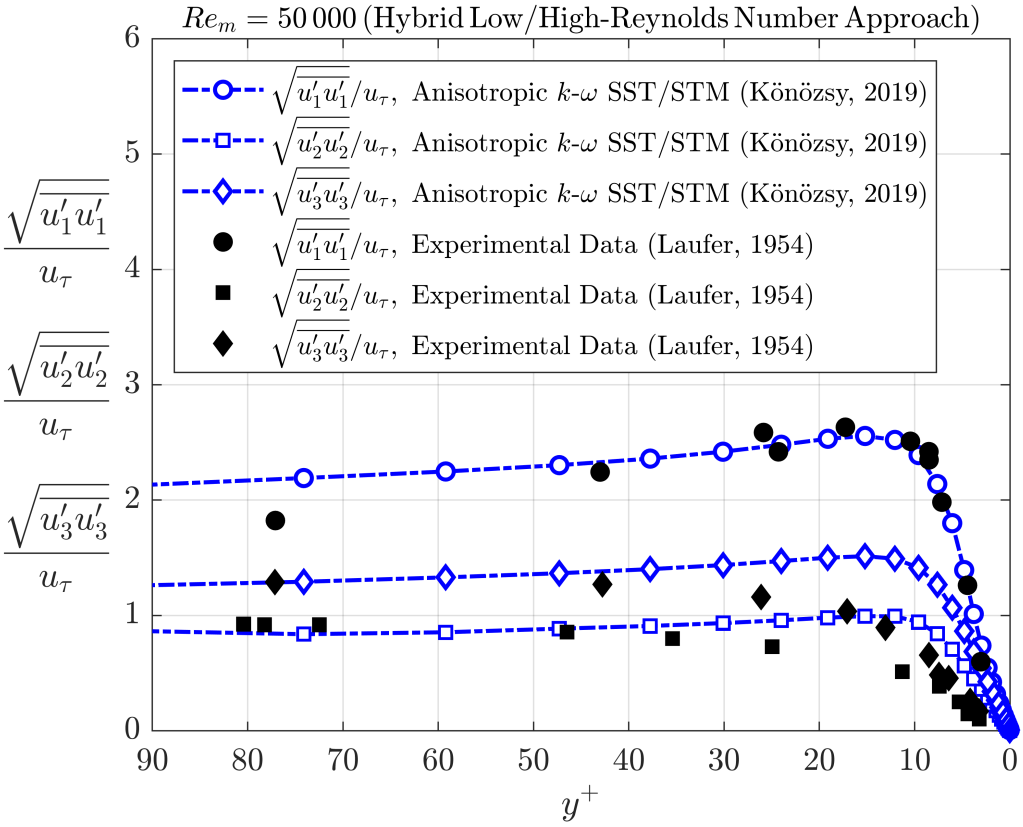

Figure 2.9: Comparison of the simulated fully-developed near-wall dimensionless RMS specific Reynolds stress profiles at $Re_m = 50\,000$ with the measurements of Laufer [47][11]

[11] Figure 2.9 used with permission of Springer Nature BV, Switzerland, from the book entitled as "A New Hypothesis on the Anisotropic Reynolds Stress Tensor for Turbulent Flows", Author: László Könözsy, Volume II, Chapter 5, p. 372, 1st. Edition 2021; the permission conveyed through Copyright Clearance Center, Inc., https://www.copyright.com/

It means that different turbulence modelling approaches and anisotropic scaling are required at $y^+(r) \lessapprox 65$ and $y^+(r) \gtrapprox 65$ with the anisotropic hybrid k-ω SST/STM closure model [6] to capture the near-wall peak fluctuations measured by Laufer [47]. Using the high Reynolds number turbulence modelling approach at $Re_m = 500\,000$ [50], it can be seen in Figure 2.10 that the anisotropic hybrid k-ω SST/STM closure model [6] predicted the physically correct behaviour of the dimensionless RMS velocity fluctuation profiles (2.54) along the dimensionless radial coordinate r/R against the measurements of Laufer [47] at $y^+(r) \gtrapprox 65$, except very near to the wall of the pipe [$y^+(r) \lessapprox 65$]; in which case the simulated Reynolds stress distributions became fully-developed at $z \geq 60D$. The k-ω SST model of Menter [9], [10], [23] predicted again the same dimensionless RMS velocity fluctuations (2.54) for each main diagonal element of the Boussinesq hypothesis-based [4] Reynolds stress tensor (2.14) similar to the case at $Re_m = 50\,000$.

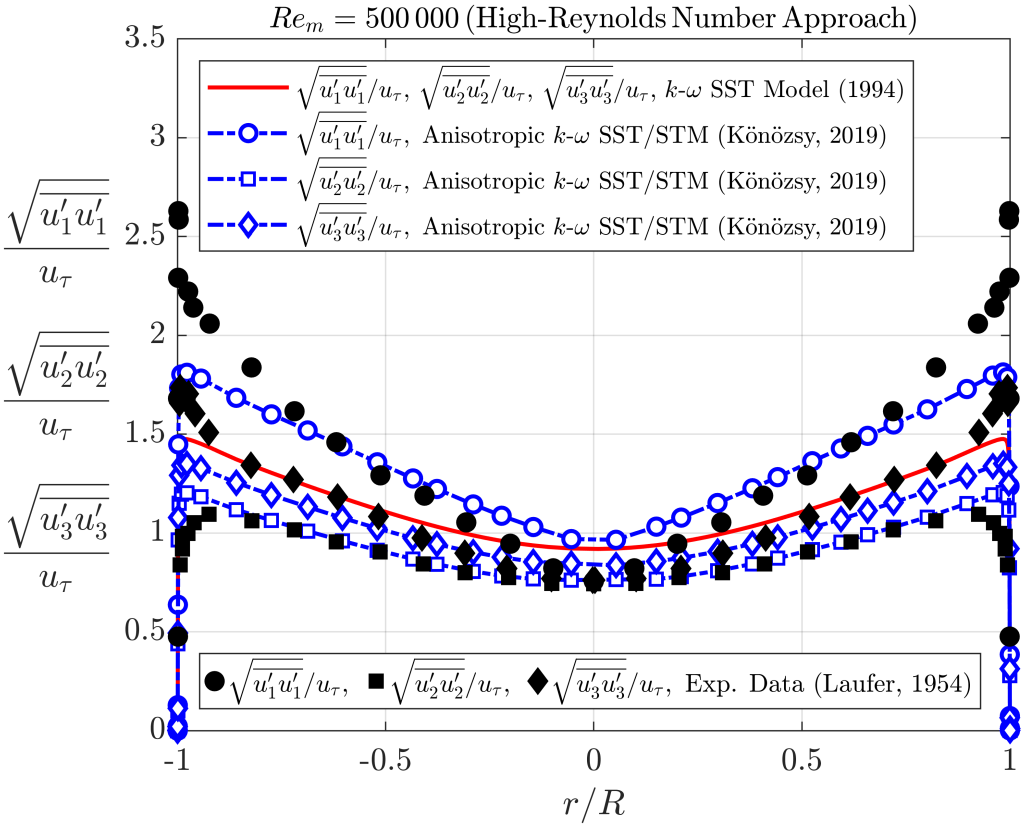

Figure 2.10: Comparison of the simulated fully-developed dimensionless RMS specific Reynolds stress profiles at $Re_m = 500\,000$ with the experimental data of Laufer [47][12]

[12]Figure 2.10 used with permission of Springer Nature BV, Switzerland, from the book entitled as "A New Hypothesis on the Anisotropic Reynolds Stress Tensor for Turbulent Flows", Author: László Könözsy, Volume II, Chapter 5, p. 373, 1st. Edition 2021; the permission conveyed through Copyright Clearance Center, Inc., https://www.copyright.com/

The physical behaviour of the dimensionless RMS velocity profiles (2.54) was captured correctly with the anisotropic hybrid k-ω SST/STM closure model [6] in the near-wall region [$y^+(r) \lessapprox 65$] at Re_m = 500 000 using again the combination of the low Reynolds number turbulence modelling approach in [50] with the high Reynolds number anisotropic scaling near to the pipe wall which is shown in Figure 2.11. As the Reynolds number increased, additional anisotropic scaling was required as indicated by the factor of 3/4 and 5/4 for the second and third dimensionless anisotropic RMS specific Reynolds stresses in Eq. (2.54) which are shown on the vertical axis of Figure 2.11 at Re_m = 500 000. The simulation results suggest that advances have been achieved with the development of the anisotropic hybrid k-ω SST/STM closure model [6] compared to the k-ω SST model [9], [10], [23] in terms of more accurate numerical prediction of the physical behaviour of anisotropic Reynolds stresses (2.26) in the field of engineering turbulence modelling.

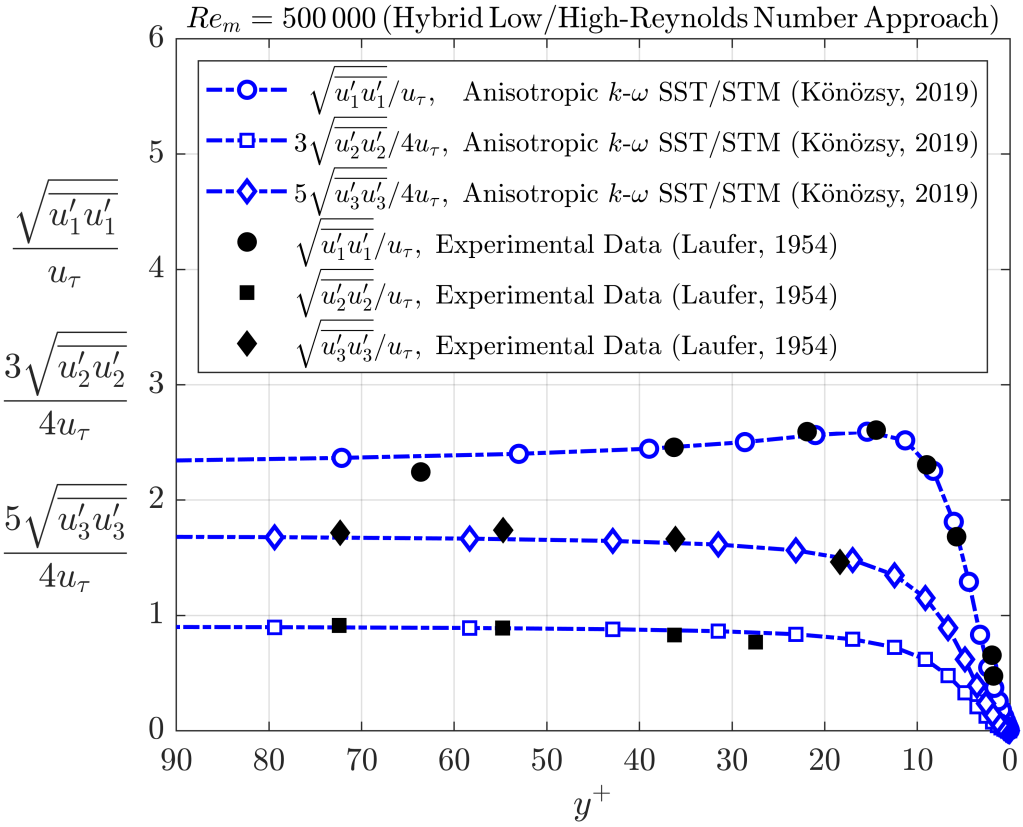

Figure 2.11: Comparison of the simulated fully-developed near-wall dimensionless RMS specific Reynolds stress profiles at Re_m = 500 000 with the measurements of Laufer [47][13]

[13] Figure 2.11 used with permission of Springer Nature BV, Switzerland, from the book entitled as "A New Hypothesis on the Anisotropic Reynolds Stress Tensor for Turbulent Flows", Author: László Könözsy, Volume II, Chapter 5, p. 373, 1st. Edition 2021; the permission conveyed through Copyright Clearance Center, Inc., https://www.copyright.com/

2.6 Summary of the contribution to the knowledge

The author of this habilitation booklet has started to conduct theoretical research on mathematical and physical descriptions of tensorial relationships in conjunction with the theory and practice of anisotropic turbulence since 2014. Relying on the theoretical development and numerical simulations overviewed in Chapter 2 which were carried out after the author received his PhD degree (2004) from the University of Miskolc, Hungary, a few conclusions can be summarised in thesis points as novel research advances from the past 10 years and contribution to the knowledge as follows:

1. Through the unification of Boussinesq hypothesis (2.14) [4] and the three-dimensional anisotropic similarity hypothesis of turbulent velocity fluctuations (2.19) [7], [8], a new anisotropic Reynolds stress tensor has been derived, proposed and introduced in the form of a single tensor Eq. (2.25) as follows [6, pp. 109-111], [T1, pp. 109-111]:

$$\underline{\underline{\tau}}^{RA} = -\rho\overline{\mathbf{u}'\otimes\mathbf{u}'} = 2\mu_t\underline{\underline{S}} + \mu_\Theta\Theta\underline{\underline{G}} - \frac{2}{3}\rho k\underline{\underline{\mathrm{I}}}. \tag{2.55}$$

   1.1. The new anisotropic Reynolds stress tensor (2.55) takes into account the contribution of the mean rate-of-strain tensor $2\mu_t\underline{\underline{S}}$, the local mechanically similar mean rotational motion $\mu_\Theta\Theta\underline{\underline{G}}$, and the turbulent kinetic energy $-(2/3)\rho k\underline{\underline{\mathrm{I}}}$ to the turbulent momentum transfer [6, pp. 109-111], [T1, pp. 109-111].

   1.2. A dimensionless scalar weight parameter μ_Θ $(0 < |\mu_\Theta| \leq 1)$ has been introduced to adjust the magnitude of the second term $\mu_\Theta\Theta\underline{\underline{G}}$ in the anisotropic Reynolds stress tensor (2.55) [37, p. 127], [T2, p. 127].

   1.3. A modified deviatoric similarity tensor (2.24) has been introduced [37, p. 122], [T2, p. 122] with anisotropic scale factors $\lambda_{11}^\star$, $\lambda_{22}^\star$, $\lambda_{33}^\star$ for engineering applications which can be calibrated based on experimental and/or Direct Numerical Simulation (DNS) data [38, p. 158], [T3, p. 158].

2. By using the anisotropic Reynolds stress tensor (2.55), the k-ω SST turbulence model [9], [10] has been further extended to anisotropic turbulent flows leading to a new anisotropic hybrid k-ω SST/STM closure model [6, pp. 117-126], [T1, pp. 117-126], thus an anisotropic variant of the k-ω SST model has been developed in [37], [T2].

   2.1. A new anisotropic production term P_k^A (2.45) of the turbulent kinetic energy k Eq. (2.50) has been derived based on the anisotropic Reynolds stress tensor (2.55) which can be written as follows [6, pp. 121-122], [T1, pp. 121-122]:

$$P_k^A = \rho\nu_t\left\{\left[(\nabla\otimes\mathbf{u}) + (\nabla\otimes\mathbf{u})^T\right]\cdot\cdot(\nabla\otimes\mathbf{u})\right\} + \mu_\Theta\Theta\left[\underline{\underline{G}}\cdot\cdot(\nabla\otimes\mathbf{u})\right]. \tag{2.56}$$

2.2. A new anisotropic production term P_{ω}^{A} (2.47) of the specific dissipation rate ω Eq. (2.51) has been derived based on the anisotropic Reynolds stress tensor (2.55) which can be written as follows [6, pp. 122-124], [T1, pp. 122-124]:

$$\boxed{P_{\omega}^{A} = \gamma\rho\left\{\left[(\nabla\otimes\mathbf{u})+(\nabla\otimes\mathbf{u})^{T}\right]\cdot\cdot(\nabla\otimes\mathbf{u})\right\}+\frac{\gamma}{\nu_{t}}\mu_{\Theta}\Theta\left[\underline{\underline{G}}\cdot\cdot(\nabla\otimes\mathbf{u})\right].} \tag{2.57}$$

2.3. A UDF C code has been developed and implemented in the environment of the ANSYS-FLUENT software package in conjunction with new source terms (2.56)–(2.57) of the anisotropic hybrid k-ω SST/STM closure model which was published by the author in [38, pp. 178-213], [T3, pp. 178-213].

2.4. The verification of the UDF C computer code and the validation of the anisotropic hybrid k-ω SST/STM closure model (2.48)–(2.51) have been carried out for benchmark problems compared to experimental data available in the literature which are relevant to engineering applications [44], [T4], [45], [T5].

2.5. The numerical value of the dimensionless scalar weight parameter μ_{Θ} has been calibrated based on simulations in conjunction with the experimental data of Klebanoff [46] and Laufer [47]. It has been found that the numerical value of the parameter μ_{Θ} is equal to -0.025 [44], [T4], [45], [T5].

2.6. It has been found that the implemented anisotropic hybrid k-ω SST/STM closure model (2.48)–(2.51) is capable of predicting accurately the physically correct behaviour of anisotropic Reynolds stress distributions for high Re turbulent flows in comparison with the experimental data of Klebanoff [46] and Laufer [47] at $y^{+} \gtrapprox 65$ (see Figures 2.3, 2.4, 2.6, 2.8, 2.10) [44, pp. 244-252], [T4, pp. 244-252], [45, pp. 370-376], [T5, pp. 370-376].

2.7. In the near-wall region at $y^{+} \lessapprox 65$, a hybrid high/low Re number turbulence modelling approach is required to be employed with the numerical values of $\mu_{\Theta}\lambda_{11}^{\star}H_{11}^{\star} = -2.9157$, $\mu_{\Theta}\lambda_{22}^{\star}H_{22}^{\star} = 1.4298$ and $\mu_{\Theta}\lambda_{33}^{\star}H_{33}^{\star} = 0.5092$ where $H_{11}^{\star} = -0.7312$, $H_{22}^{\star} = 0.5223$ and $H_{33}^{\star} = 0.2089$ in Eq. (2.24) for accurately predicting the anisotropic Reynolds stress distributions in comparison with the experimental data of Laufer [47] [45, p. 371], [T5, p. 371].

2.8. It has been found that the new anisotropic Reynolds stress tensor (2.55) in conjunction with the 3D similarity theory [8] is valid in the near-wall region at $y^{+} \lessapprox 65$ (see Figures 2.9 and 2.11) [45, pp. 372-373], [T5, pp. 372-373].

2.7 Új tudományos eredmények összefoglalása

E habilitációs füzet szerzője 2014 óta foglalkozik olyan elméleti kutatásokkal, amelyek az anizotróp turbulencia elméletével és gyakorlatával összefüggésben a tenzoriális kapcsolatok matematikai és fizikai leírására irányul. Az 2. Fejezetben áttekintett elméleti fejlesztések és numerikus szimulációk alapján, amelyeket a szerző a PhD fokozatának (2004) a Miskolci Egyetemen, Magyarországon történő megszerzése után végzett, néhány konklúzió mint az elmúlt 10 év új kutatási előrelépései és a tudományos ismereteinkhez való hozzájárulás a következő tézispontokban foglalható össze:

1. A Boussinesq hipotézis (2.14) [4] és a turbulens sebességingadozások háromdimenziós anizotróp hasonlósági hipotézisének (2.19) [7], [8] egyesítésével egy új anizotróp Reynolds-féle feszültségtenzort vezettem le, javasoltam és bevezettem egyetlen tenzoregyenlet (2.25) formájában az alábbi szerint [6, pp. 109-111], [T1, pp. 109-111]:

$$\boxed{\underline{\underline{\tau}}^{RA} = -\rho\overline{\mathbf{u}'\otimes\mathbf{u}'} = 2\mu_t\underline{\underline{S}} + \mu_\Theta\Theta\underline{\underline{G}} - \frac{2}{3}\rho k\underline{\underline{\mathrm{I}}}.} \tag{2.58}$$

   1.1. Az új anizotrop Reynolds-féle feszültségtenzor (2.58) figyelembe veszi az átlagolt alakváltozási sebesség tenzornak $2\mu_t\underline{\underline{S}}$, a helyi mechanikailag hasonló forgómozgásnak $\mu_\Theta\Theta\underline{\underline{G}}$, és a turbulens kinetikus energiának $-(2/3)\rho k\underline{\underline{\mathrm{I}}}$ a turbulens impulzuscserére gyakorolt hatását [6, pp. 109-111], [T1, pp. 109-111].

   1.2. Bevezettem egy dimenziótlan skalár súlyozási paramétert μ_Θ $(0 < |\mu_\Theta| \leq 1)$ az anizotróp Reynolds-féle feszültségtenzor (2.58) második tagja $\mu_\Theta\Theta\underline{\underline{G}}$ nagyságrendjének beállítására [37, p. 127], [T2, p. 127].

   1.3. Bevezettem egy módosított hasonlósági deviátor tenzort (2.24) [37, p. 122], [T2, p. 122] anizotróp lépték tényezőkkel $\lambda^\star_{11}$, $\lambda^\star_{22}$, $\lambda^\star_{33}$ együtt műszaki alkalmazásokhoz, amelyek kísérleti és/vagy Direkt Numerikus Szimulációs (DNS) adatok alapján kalibrálhatók [38, p. 158], [T3, p. 158]. .

2. Az anizotróp Reynolds-féle feszültségtenzor (2.58) felhasználásával a k-ω SST turbulencia modellt [9], [10] kiterjesztettem anizotróp turbulens áramlásokra, amely egy új anizotróp hibrid k-ω SST/STM zárási modellhez vezetett [6, pp. 117-126], [T1, pp. 117-126], így kifejlesztettem a k-ω SST modell egy anizotróp változatát [37], [T2].

   2.1. Levezettem a turbulens kinetikus energia k (2.50) egyenletére egy új anizotróp produkciós tagot P_k^A (2.45) az anizotróp Reynolds-féle feszültségtenzor (2.58) alapján, amely a következőképpen írható [6, pp. 121-122], [T1, pp. 121-122]:

$$\boxed{P_k^A = \rho\nu_t\left\{\left[(\nabla\otimes\mathbf{u}) + (\nabla\otimes\mathbf{u})^T\right]\cdot\cdot(\nabla\otimes\mathbf{u})\right\} + \mu_\Theta\Theta\left[\underline{\underline{G}}\cdot\cdot(\nabla\otimes\mathbf{u})\right].} \tag{2.59}$$

2.2. Levezettem a fajlagos disszipáció arány ω (2.51) egyenletére egy új anizotróp produkciós tagot P_ω^A (2.47) az anizotróp Reynolds-féle feszültségtenzor (2.58) alapján, amely az alábbi szerint írható [6, pp. 122-124], [T1, pp. 122-124]:

$$\boxed{P_\omega^A = \gamma\rho\left\{\left[(\nabla\otimes\mathbf{u})+(\nabla\otimes\mathbf{u})^T\right]\cdot\cdot(\nabla\otimes\mathbf{u})\right\}+\frac{\gamma}{\nu_t}\mu_\Theta\Theta\left[\underline{\underline{G}}\cdot\cdot(\nabla\otimes\mathbf{u})\right].} \tag{2.60}$$

2.3. Egy UDF C kódot fejlesztettem ki az anizotróp hibrid k-ω SST/STM zárási modell új forrástagjaival (2.59)–(2.60) összefüggésben, és implementáltam az ANSYS-FLUENT szoftvercsomag környezetben, amelyet ennek a füzetnek a szerzője a [38, pp. 178-213], [T3, pp. 178-213] munkájában publikált.

2.4. Az UDF C számítógépes kód verifikációját és az anizotróp hibrid k-ω SST/STM zárási modell (2.48)–(2.51) validálását mintafeladatokon végeztem el összehasonlítva az irodalomban elérhető kísérleti adatokkal, amelyek mérnöki alkalmazások szempontjából relevánsak [44], [T4], [45], [T5].

2.5. A dimenziótlan skalár súlyozási paraméter μ_Θ értékét szimulációk alapján Klebanoff [46] és Laufer [47] kísérleti adataival összefüggésben kalibráltam. Megállapítottam, hogy a μ_Θ paraméter értéke -0.025 [44], [T4], [45], [T5].

2.6. Megállapítottam, hogy az anizotróp hibrid k-ω SST/STM zárási modell (2.48)–(2.51) alkalmas az anizotróp Reynolds-féle feszültségeloszlások fizikailag helyes viselkedésének pontos becslésére nagy Re számú turbulens áramlások esetén Klebanoff [46] és Laufer [47] kísérleti adataival összehasonlítva, amikor $y^+ \gtrapprox 65$ (lásd 2.3, 2.4, 2.6, 2.8, 2.10 ábrákat) [44, pp. 244-252], [T4, pp. 244-252], [45, pp. 370-376], [T5, pp. 370-376].

2.7. A falközeli régióban $y^+ \lessapprox 65$ esetén, egy hibrid nagy/kis Re számú turbulencia modellezési megközelítés alkalmazása szükséges a $\mu_\Theta\lambda_{11}^\star H_{11}^\star = -2.9157$, $\mu_\Theta\lambda_{22}^\star H_{22}^\star = 1.4298$ és $\mu_\Theta\lambda_{33}^\star H_{33}^\star = 0.5092$ számértékekkel, ahol $H_{11}^\star = -0.7312$, $H_{22}^\star = 0.5223$ és $H_{33}^\star = 0.2089$ a (2.24) egyenletben, hogy az anizotróp Reynolds-féle feszültségeloszásokat Laufer [47] kísérleti adataival összehasonlítva pontosan lehessen becsülni [45, p. 371], [T5, p. 371].

2.8. Megállapítottam, hogy az új anizotróp Reynolds-féle feszültségtenzor (2.58) a 3D hasonlósági elmélettel [8] összefüggésben érvényes a falközeli régióban $y^+ \lessapprox 65$ esetén (lásd 2.9 és 2.11 ábrákat) [45, pp. 372-373], [T5, pp. 372-373].

Chapter 3

Advances in the Numerical Solution of the Navier–Stokes Equations

3.1 Introduction

In this Chapter, the third subject area of this habilitation booklet focuses on the overview of the author's research work in the field of the numerical solution of Navier–Stokes equations for incompressible fluid flows in the context of pseudo-transient methods. A new unified approach and numerical procedure have been developed for pressure-velocity (PV) field coupling which is relying on the unification of the Artificial Compressibility (AC) and Fractional-Step Pressure-Projection (FS-PP) methods of Chorin [51], [52]. The foundations for unifying the hyperbolic-type (AC) and the pressure-Poisson equation based elliptical-type (FS-PP) method led to a unified FSAC-PP formulation which was proposed, derived and implemented by Könözsy (2012) [53] at Cranfield University, United Kingdom. Following that, Könözsy and Drikakis (2014) [54] published a comprehensive work on the unification of the AC and FS-PP formulations along with the validation of the unified FSAC-PP numerical solution procedure for benchmark problems. Therefore, after a brief literature review of different solution frameworks of the incompressible Navier–Stokes equations in Section 3.2, the unification of the AC and FS-PP formulations has been overviewed along with a brief presentation of validated simulation results based on the work of Könözsy and Drikakis (2014) [54] in Section 3.3. For the sake of simplicity, only the stationary formulation of the FSAC-PP method has been considered here. In addition to that, some validation results have been reviewed based on the works of Teschner, Könözsy and Jenkins (2018, 2019) [55], [56]. The review of these previous works has of relevance in terms of better understanding the motivation behind the development of a two-stage pseudo-transient Navier–Stokes solver derived, proposed and implemented by Könözsy (2017) [57] which will be overviewed in Section 3.4.

3.2 A brief literature review and its critical assessment

For solving the incompressible Navier–Stokes equations, the development of new numerical solution frameworks or further improve existing algorithms in conjunction with different numerical schemes is a current state-of-the-art research field. Therefore, within the context of this brief literature review, we consider the governing equations of three solution frameworks which are relevant to our subject. Therefore, let us consider the set of governing equations for incompressible and isothermal fluid flows as follows:

$$\nabla \cdot \mathbf{u} = 0, \tag{3.1}$$

$$\frac{\partial \mathbf{u}}{\partial t} + (\mathbf{u} \cdot \nabla)\,\mathbf{u} = -\frac{1}{\rho}\nabla p + \nu \nabla^2 \mathbf{u} + \mathbf{g}, \tag{3.2}$$

where t is the real time, $\mathbf{u}$ is the velocity field, p is the pressure field, ρ is the density of the fluid, ν is the kinematic viscosity of the fluid, and $\mathbf{g}$ is the gravitational vector field. For incompressible fluid flows, the mass conservation or continuity Eq. (3.1) expresses the divergence-free physical constraint for the velocity field which means that the continuum element does not undergo any volumetric expansion or compression. The vector form of the Navier–Stokes momentum Eq. (3.2) mathematically describe the physical behaviour of Newtonian fluids for laminar flows at Reynolds numbers of $Re < 2320$. To solve initial and boundary value problems numerically for the system of Eqs. (3.1)–(3.2), a pressure equation has to be derived, because the pressure and velocity field computations have to be coupled with each other. Therefore, each Navier–Stokes solver for incompressible flows constructs a solution framework for coupling the velocity and pressure field which is called Pressure-Velocity Coupling (PVC) method or scheme. To derive different PVC schemes, the Navier–Stokes Eq. (3.2) can be expressed in a semi-discrete form [58] as

$$\frac{\mathbf{u}^{(n+1)} - \mathbf{u}^{(n)}}{\triangle t} = -\frac{1}{\rho}\nabla p^{(n+1)} - [(\mathbf{u} \cdot \nabla)\,\mathbf{u}]^{(n)} + \nu \nabla^2 \mathbf{u}^{(n)} + \mathbf{g}, \tag{3.3}$$

where $\triangle t$ is the time step, and the superscript notations $(n+1)$ and (n) denote the corresponding time-levels in the numerical iteration procedure. The advantage of the semi-discrete mathematical description of different solution frameworks for the Navier–Stokes Eq. (3.2) is that different pressure-velocity (PV) coupling closure models can be presented in an understandable way through them. Therefore, it has been used frequently below.

3.2.1 Marker and Cell Pressure-Projection (MAC-PP) method (1965)

For solving viscous fluid flow problems with free surfaces, Harlow and Welch (1965) [59] developed the Marker-and-Cell (MAC) projection method. In that case, the divergence of the Navier–Stokes Eq. (3.3) with the assumption that the continuity Eq. (3.1) is satisfied

at the next time-level $(n+1)$, i.e., $\nabla \cdot \mathbf{u}^{(n+1)} = 0$ leads to a pressure-Poisson equation as

$$\nabla^2 p^{(n+1)} = \frac{\rho}{\triangle t} \nabla \cdot \left\{ \mathbf{u}^{(n)} - \triangle t \left[(\mathbf{u} \cdot \nabla) \mathbf{u} \right]^{(n)} + \triangle t \, \nu \nabla^2 \mathbf{u}^{(n)} \right\}, \tag{3.4}$$

where $p^{(n+1)}$ stands for the projection of the pressure field into a divergence-free velocity field at time-level $(n+1)$. If the mass conservation (continuity) Eq. (3.1) is satisfied at time-level (n), then the pressure-Poisson Eq. (3.4) simplifies to

$$\nabla^2 p^{(n+1)} = -\rho \nabla \cdot \left[(\mathbf{u} \cdot \nabla) \mathbf{u} \right]^{(n)}, \tag{3.5}$$

which can also be derived by taking the divergence of the Navier–Stokes Eq. (3.2). The MAC abbreviation is related to the staggered arrangement of the primitive variables u, v, w, p where the discrete pressure field p is located at the centre of each computational cell, and the discrete velocity components u, v and w are placed in x, y and z directions at each side of the control volume in the spatial discretisation scheme, respectively. The MAC method was developed in Los Alamos and the reason for using the staggered arrangement of the velocity and pressure field variables is to avoid possible non-physical pressure oscillations in the numerical solution. After re-arranging the semi-discrete form of the Navier–Stokes Eq. (3.3), the velocity field at time-level $(n+1)$ can be computed based on the projected pressure field $p^{(n+1)}$ and the predicted velocity field at time-level (n) as

$$\mathbf{u}^{(n+1)} = \mathbf{u}^{(n)} - \frac{\triangle t}{\rho} \nabla p^{(n+1)} - \triangle t \left[(\mathbf{u} \cdot \nabla) \mathbf{u} \right]^{(n)} + \triangle t \, \nu \nabla^2 \mathbf{u}^{(n)} + \triangle t \, \mathbf{g}. \tag{3.6}$$

Könözsy (2017) [57] proposed a pseudo-transient pressure evolution equation, i.e., a two-stage pseudo-transient pressure projection solution method to overcome the oscillatory pressure field behaviour for incompressible stationary flows when the primitive variables u, v, w, p have a collocated arrangement on the structured computational mesh points.

3.2.2 Artificial Compressibility (AC) method (1967)

For stationary flows, Chorin (1967) [51] introduced a perturbed continuity equation which involves a pseudo-transient pressure term in the continuity Eq. (3.1). The real-time derivative on the right-hand side of the Navier–Stokes Eq. (3.2) was replaced with a pseudo-time derivative for solving steady-state problems. The governing Eqs. (3.1)–(3.2) was transformed by Chorin [51] into a system of hyperbolic-type equations as follows:

$$\frac{1}{\beta} \frac{\partial p}{\partial \tau} + \nabla \cdot \mathbf{u} = 0, \tag{3.7}$$

$$\frac{\partial \mathbf{u}}{\partial \tau} + (\mathbf{u} \cdot \nabla) \mathbf{u} = -\frac{1}{\rho} \nabla p + \nu \nabla^2 \mathbf{u} + \mathbf{g}, \tag{3.8}$$

where β is the artificial compressibility (AC) parameter which is responsible for the convergence of the numerical solution, and τ is the pseudo-time. Peyret and Taylor [60]

pointed out that the pseudo-transient pressure term $\partial p/\partial \tau$ in the perturbed continuity Eq. (3.7) has no physical meaning until the stationary numerical solution is achieved. The AC method of Chorin [51] is also called pseudo-compressibility method in the literature [61], although the density of the fluid ρ still remains constant in the numerical solution and the AC method does not take into account any real compressibility effect. Therefore, the AC method of Chorin [51] is a pseudo-transient pressure-velocity (PV) coupling scheme for solving incompressible fluid flow problems. The governing Eqs. (3.7)–(3.8) of the pseudo-transient AC method can be written in a semi-discrete vector form as

$$\frac{1}{\beta}\frac{p^{(n+1)}-p^{(n)}}{\triangle\tau}+\nabla\cdot\mathbf{u}^{(n)}=0, \tag{3.9}$$

$$\frac{\mathbf{u}^{(n+1)}-\mathbf{u}^{(n)}}{\triangle\tau}=-\frac{1}{\rho}\nabla p^{(n+1)}-[(\mathbf{u}\cdot\nabla)\mathbf{u}]^{(n)}+\nu\nabla^2\mathbf{u}^{(n)}+\mathbf{g}, \tag{3.10}$$

where the superscripts $(n+1)$ and (n) denote pseudo-time level in the numerical iterations. After re-arranging Eqs. (3.9)–(3.10), the AC method of Chorin [51] leads to a two-stage algorithm for solving incompressible fluid flow problems as follows:

$$p^{(n+1)}=p^{(n)}-\beta\triangle\tau\nabla\cdot\mathbf{u}^{(n)}, \tag{3.11}$$

$$\mathbf{u}^{(n+1)}=\mathbf{u}^{(n)}-\frac{\triangle\tau}{\rho}\nabla p^{(n+1)}-\triangle\tau[(\mathbf{u}\cdot\nabla)\mathbf{u}]^{(n)}+\triangle\tau\nu\nabla^2\mathbf{u}^{(n)}+\triangle\tau\mathbf{g}, \tag{3.12}$$

where each term can be disretised with numerical approximation schemes, e.g., in the context of Finite Difference Method (FDM) and Finite Volume Method (FVM) using explicit, implicit or semi-implicit numerical solution approaches. In terms of the discretisation of the non-linear convective term in Eq. (3.12), a characteristics-based (CB) scheme was derived by Drikakis et al. [62] in the context of Godunov-type discretisation methods. The CB scheme proposed Drikakis et al. [62] was further extended to three-dimensional problems using a non-linear, Full-MultiGrid, Full-Approximation-Storage (FMG-FAS) algorithm [63], [64]. Zamzamian and Razavi [65] proposed a multidimensional, characteristics-based upwind approach and validated it for different benchmark problems in the framework of the AC formulation (3.11)–(3.12) of Chorin [51]. The AC method can solve accurately the governing Eqs. (3.11)–(3.12) for stationary fluid flows. For solving unsteady physical problems, a dual-time stepping procedure has to be employed as described in [54], [66]. For low and very low Reynolds number flows ($Re < 1$), the numerical solution with the AC method can lead to slow convergence rates [60]. However, Monokrousos et al. (2024) [61] recently published a work in the context of finite difference (FD) methods on how to overcome the low Re number limitation of the AC method with a high-order numerical treatment of the pressure boundary condition.

3.2.3 Fractional-Step Pressure Projection (FS-PP) method (1968)

For solving unsteady incompressible fluid flow problems, Chorin (1968) [52] and Temam (1969) [67] proposed a Fractional-Step Pressure-Projection (FS-PP) method in which case an elliptic-type pressure-Poisson equation has to be solved in addition to the Navier–Stokes Eq. (3.2). Chorin [52] splitted the numerical solution procedure into three stages using the Helmholtz-Hodge decomposition [68]–[72]. In the first step, an intermediate velocity field prediction was introduced where the contribution of the pressure gradient term to the flow field on the right-hand side of the Navier–Stokes Eq. (3.2) was neglected. In the second step, a pressure-Poisson equation is solved numerically in conjunction with the intermediate velocity field. In the third step, the intermediate velocity field is projected into a divergence-free velocity field satisfying the continuity Eq. (3.1) at time-level $(n+1)$. The semi-discrete system of equations of two fractional time-steps can be written as

$$\frac{\mathbf{u}^{\star}-\mathbf{u}^{(n)}}{\triangle t} = -\left[(\mathbf{u}\cdot\nabla)\,\mathbf{u}\right]^{(n)} + \nu\nabla^2\mathbf{u}^{(n)} + \mathbf{g}, \tag{3.13}$$

$$\frac{\mathbf{u}^{(n+1)}-\mathbf{u}^{\star}}{\triangle t} = -\frac{1}{\rho}\nabla p^{(n+1)}, \tag{3.14}$$

where $\mathbf{u}^{\star}$ is the intermediate velocity field which is not divergence-free ($\nabla\cdot\mathbf{u}^{\star}\neq 0$). The intermediate velocity field $\mathbf{u}^{\star}$ can be predicted based on the velocity field solution at time-level (n) and can be derived from Eq. (3.13) as

$$\mathbf{u}^{\star} = \mathbf{u}^{(n)} + \triangle t\left\{\nu\nabla^2\mathbf{u}^{(n)} - \left[(\mathbf{u}\cdot\nabla)\,\mathbf{u}\right]^{(n)} + \mathbf{g}\right\}, \tag{3.15}$$

and by taking the divergence of the semi-discrete Eq. (3.14) assuming that the divergence-free continuity Eq. (3.1) is satisfied at time-level $(n+1)$, i.e., $\nabla\cdot\mathbf{u}^{(n+1)}=0$, an elliptic-type pressure-Poisson equation can be derived as

$$\nabla^2 p^{(n+1)} = \frac{\rho}{\Delta t}\left(\nabla\cdot\mathbf{u}^{\star}\right), \tag{3.16}$$

which makes a relationship between the projected pressure field $p^{(n+1)}$ at time-level $(n+1)$ and the intermediate velocity field $\mathbf{u}^{\star}$ (3.15). After re-arranging the second fractional step Eq. (3.14), an equation can be obtained to update the velocity field values at time-level $(n+1)$ based on the pressure field $p^{(n+1)}$ solution as

$$\mathbf{u}^{(n+1)} = \mathbf{u}^{\star} - \frac{\triangle t}{\rho}\nabla p^{(n+1)}. \tag{3.17}$$

Advanced, accurate and efficient FS-PP algorithms were developed by Bell et al. [69], Bell and Marcus [70], Almgren et al. [71]. In the context of Finite Element (FE) methods, Codina et al. (1998) [73] developed a semi-implicit CB split algorithm in conjunction with the FS-PP method of Chorin [52]. Note that another class of the PV coupling algorithms is the class of pressure-correction methods which are different from pressure projection

methods and these approaches are not subject of this habilitation booklet. Although, pressure-correction methods are used as a standard approach to the pressure field solution in commercial and industrial CFD software packages. The first pressure-correction algorithm was developed by Patankar and Spalding (1972) [74] introducing a version of the Semi-Implicit Method for Pressure Linked Equations (SIMPLE) algorithm where a pressure-Poisson equation is also employed. More details on pressure-correction methods can be found in the books of Patankar [75], Versteeg and Malalasekera [76], and Ferziger and Perić [77], because different variants of the SIMPLE algorithm exist.

3.2.4 Hybrid pressure-velocity coupling methods

In the context of FEM, Zienkiewicz et al. (1995-1999) [78]–[81] developed a CB split solution method to solve compressible and incompressible fluid flow problems in a unified manner. Nithiarasu (2002, 2004) [82], [83] proposed a CB split AC scheme to use the advantageous features of the AC and velocity correction methods. Tang and Sotiropoulos (2007) [84] proposed a hybrid time-accurate Fractional-Step Artificial Compressibility (FSAC) approach to improve the efficiency of the AC method of Chorin [51]. For solving the Navier–Stokes Eq. (3.2) for incompressible fluid flows, the unification of Chorin's AC [51] and FS-PP [52] pressure-velocity coupling methods was proposed, derived and implemented by Könözsy (2012) [53]. The unification of these two different, i.e., the hyperbolic-type AC [51] and the elliptical-type FS-PP [52] algorithms led to the unified FSAC-PP method [54] in which case initial validated numerical results were obtained for different standard and multiphysics benchmark problems in [53]. Following that, a comprehensive validation of the FSAC-PP method was carried out by Könözsy and Drikakis (2014) [54] in conjunction with a) a characteristics-based (CB) Godunov-type scheme [62] in terms of the discretisation of the non-linear convective terms and b) the use of the FMG-FAS multigrid algorithm [63], [64]. Könözsy and Drikakis (2012) [85] proposed and validated the FSAC-PP method for solving low Mach number variable density flows as well which is not subject of the present overview. Overall, it has been found that the FSAC-PP algorithm in the context of CB Godunov-type discretisation methods has a) advantageous convergence properties along with solving problems accurately at very low Reynolds numbers and b) the interaction between the perturbed continuity Eq. (3.7) and the pressure-Poisson Eq. (3.16) could enhance the efficiency of the numerical solution procedure. Although, the interaction between the pseudo-time evolutionary perturbed continuity Eq. (3.16) and the spatially evolving numerical solution of the pressure-Poisson Eq. (3.16) could lead to minor oscillatory behaviour of the pressure field. Therefore, Könözsy (2017) [57] proposed, derived and implemented a two-stage pseudo-transient pressure-velocity coupling algorithm where a pseudo-time evolutionary pressure transport equation was introduced to reduce the possible oscillatory behaviour of the pressure field solution which will be overviewed and discussed in Section 3.4.

3.3 Unification of the AC and FS-PP solution methods

In this Section, we overview briefly the unification of the artificial compressibility (AC) and Fractional-Step Pressure-Projection (FS-PP) methods of Chorin [51], [52] based on the work of Könözsy and Drikakis (2014) [54][1]which leads to a unified FSAC-PP method for solving incompressible fluid flow problems. The motivation for developing a unified solution algorithm was to combine the advantageous accuracy properties of characteristics-based (CB) Godunov-type schemes [62], [66] with the FS-PP method for solving very low Reynolds Re number fluid flow problems ($Re \ll 1$) arise in engineering practice [54]. Note that very low Re number flows occur, e.g., in microfluidic devices [58]. For the sake of simplicity, the unification of the four-stage FSAC-PP algorithm [54] is overviewed here for solving incompressible steady-state flows in the context of pseudo-transient solution methods. Furthermore, a brief presentation of validated computational results is overviewed here to understand better the motivation for developing a two-stage pseudo-transient algorithm in [57] which will be discussed in Section 3.4.

3.3.1 Overview of the theoretical background

For solving incompressible stationary fluid flow problems, the coupling of the perturbed continuity Eq. (3.7) of the AC method (1967) [51] with the FS-PP algorithm (1968) [52] through replacing the real-time derivative with a pseudo-time derivative in Eqs. (3.15)–(3.17) will lead to a unified pseudo-transient FSAC-PP formulation as follows:

$$\frac{1}{\beta}\frac{p^{(n)}-p^{(n-1)}}{\triangle\tau} = -\nabla\cdot\mathbf{u}^{(n)}, \tag{3.18}$$

$$\frac{\mathbf{u}^{\star}-\mathbf{u}^{(n)}}{\triangle\tau} = -\left[(\widetilde{\mathbf{u}}\cdot\nabla)\widetilde{\mathbf{u}}\right]^{(n)} + \nu\nabla^2\mathbf{u}^{(n)}, \tag{3.19}$$

$$\nabla^2 p^{(n+1)} = \frac{\rho}{\triangle\tau}\left(\nabla\cdot\mathbf{u}^{\star}\right), \tag{3.20}$$

$$\mathbf{u}^{(n+1)} = \mathbf{u}^{\star} - \frac{\triangle\tau}{\rho}\nabla p^{(n+1)}, \tag{3.21}$$

where the superscripts (n), $(n-1)$, $(n+1)$ stand for the pseudo-time level in the numerical iterations, β is a numerical convergence parameter taken from the artificial compressibility (AC) formulation of Chorin [51] (see Subsection 3.2.2), $\triangle\tau$ is the pseudo-time step, $\mathbf{u}$ is the velocity field, $\mathbf{u}^{\star}$ is the intermediate velocity field introduced by Chorin [52] in the context of the FS-PP method (see Subsection 3.2.3), $\widetilde{\mathbf{u}}$ is the velocity field where the tilde

[1]Some parts of the theory and equations overviewed in Section 3.3 were first published in the article entitled as "A Unified Fractional-Step, Artificial Compressibility and Pressure-Projection Formulation for Solving the Incompressible Navier–Stokes Equations", Authors: László Könözsy and Dimitris Drikakis, *Communications in Computational Physics*, Vol. 16, No. 5, pp. 1135-1180, November 2014, ISSN: 1815-2406, published by Global Science Press.

notation indicates the characteristics-based (CB) numerical treatment of the non-linear convective term, ν is the kinematic viscosity of the fluid, and ρ is the density of the fluid. The non-linear convective term is written in a convective form $(\widetilde{\mathbf{u}}\cdot\nabla)\,\widetilde{\mathbf{u}}$ on the right-hand side of the semi-discrete momentum Eq. (3.19) of the intermediate velocity field $\mathbf{u}^{\star}$. To reformulate this term mathematically, let us consider the following vector identity [34] as

$$\nabla\cdot(\mathbf{a}\otimes\mathbf{b}) = (\nabla\cdot\mathbf{a})\,\mathbf{b} + (\mathbf{a}\cdot\nabla)\,\mathbf{b}, \quad \text{thus} \quad (\mathbf{a}\cdot\nabla)\,\mathbf{b} = \nabla\cdot(\mathbf{a}\otimes\mathbf{b}) - (\nabla\cdot\mathbf{a})\,\mathbf{b}, \tag{3.22}$$

where the symbol '$\otimes$' stands for the dyad product [18], and let us substitute $\widetilde{\mathbf{u}} = \mathbf{a} = \mathbf{b}$ in Eq. (3.22) by taking into account the continuity Eq. (3.1) for incompressible flows, thus

$$(\widetilde{\mathbf{u}}\cdot\nabla)\,\widetilde{\mathbf{u}} = \nabla\cdot(\widetilde{\mathbf{u}}\otimes\widetilde{\mathbf{u}}) - \underbrace{(\nabla\cdot\widetilde{\mathbf{u}})}_{=0}\widetilde{\mathbf{u}} = \nabla\cdot(\widetilde{\mathbf{u}}\otimes\widetilde{\mathbf{u}}), \tag{3.23}$$

which means that the convective mathematical form of the non-linear convective term in the semi-discrete momentum Eq. (3.19) can be written in a conservative form $\nabla\cdot(\widetilde{\mathbf{u}}\otimes\widetilde{\mathbf{u}})$. For simulating different incompressible fluid flows, it is convenient to use the dimensionless mathematical form of the governing Eqs. (3.18)–(3.21) of the unified FSAC-PP method. Therefore, let us introduce dimensionless quantities for the temporal and spatial coordinates, scalar velocity components and pressure field [54] as follows:

$$t^{*} = \frac{tu_{\infty}}{L},\ X = \frac{x}{L},\ Y = \frac{y}{L},\ Z = \frac{z}{L},\ U = \frac{u}{u_{\infty}},\ V = \frac{v}{u_{\infty}},\ W = \frac{w}{u_{\infty}},\ P = \frac{p}{\rho_{\infty}u_{\infty}^{2}}, \tag{3.24}$$

where L, u_{∞}, ρ_{∞} are reference quantities for the geometrical length, velocity magnitude and the density of the fluid which are constants in a numerically investigated fluid flow problem [54]. The Reynolds number is $Re = u_{\infty}L/\nu$. Using Eq. (3.24) to non-dimensionalise the original system of Eqs. (3.1)–(3.2), then the dimensionless form of the re-arranged Eqs. (3.18)–(3.21) of the unified FSAC-PP method can be written as

$$P^{(n)} = P^{(n-1)} - \triangle\tau\beta\nabla\cdot\mathbf{U}^{(n)}, \tag{3.25}$$

$$\mathbf{U}^{\star} = \mathbf{U}^{(n)} + \triangle\tau\left[\frac{1}{Re}\nabla^{2}\mathbf{U} - \nabla\cdot\left(\widetilde{\mathbf{U}}\otimes\widetilde{\mathbf{U}}\right)\right]^{(n)}, \tag{3.26}$$

$$\nabla^{2}P^{(n+1)} = \frac{1}{\triangle\tau}\left(\nabla\cdot\mathbf{U}^{\star}\right), \tag{3.27}$$

$$\mathbf{U}^{(n+1)} = \mathbf{U}^{\star} - \triangle\tau\nabla P^{(n+1)}, \tag{3.28}$$

where the β parameter may be estimated for low Re number flows [86] as

$$\beta \gg \left(1 + \frac{4L}{Re}\right)^{2} - 1. \tag{3.29}$$

As an example, for discretising the dimensionless governing Eqs. (3.25)–(3.28) of the unified FSAC-PP method, the dimensionless perturbed continuity Eq. (3.25) can be discretised on a collocated cell-centred rectangular computational mesh using a cell-centred finite difference (FD) approach [62] as follows:

$$P^{(n)}_{i,j,k} = P^{(n-1)}_{i,j,k} - \triangle\tau\beta\left(\frac{U_{i,j,k}-U_{i-1,j,k}}{\triangle X}+\frac{V_{i,j,k}-V_{i,j-1,k}}{\triangle Y}+\frac{W_{i,j,k}-W_{i,j,k-1}}{\triangle Z}\right)^{(n)}, \tag{3.30}$$

where the subscripts i, j, k are related to cell-centred physical quantities, and a first-order backward finite difference approximation is employed on the right-hand side of the discretised dimensionless perturbed continuity Eq. (3.30) which predicts an initial pressure field for the numerical solution of the pressure-Poisson Eq. (3.27). For computing the dimensionless velocity component $U^{\star}$ of the intermediate velocity field (3.26), a hybrid finite difference/finite volume (FD/FV) approach has been employed here [66] as

$$\begin{aligned} U^{\star}_{i,j,k} = U^{(n)}_{i,j,k} + \frac{\triangle\tau}{Re}\Bigg[&\frac{U_{i+1,j,k}-2U_{i,j,k}+U_{i-1,j,k}}{(\triangle X)^2}+\frac{U_{i,j+1,k}-2U_{i,j,k}+U_{i,j-1,k}}{(\triangle Y)^2}+\\ &+\frac{U_{i,j,k+1}-2U_{i,j,k}+U_{i,j,k-1}}{(\triangle Z)^2}\Bigg]^{(n)}-\triangle\tau\Bigg[\frac{\widetilde{U}^2_{i+1/2,j,k}-\widetilde{U}^2_{i-1/2,j,k}}{\triangle X}+\\ &+\frac{\left(\widetilde{V}\widetilde{U}\right)_{i,j+1/2,k}-\left(\widetilde{V}\widetilde{U}\right)_{i,j-1/2,k}}{\triangle Y}+\frac{\left(\widetilde{W}\widetilde{U}\right)_{i,j,k+1/2}-\left(\widetilde{W}\widetilde{U}\right)_{i,j,k-1/2}}{\triangle Z}\Bigg]^{(n)}, \end{aligned} \tag{3.31}$$

where the subscripts i, j, k are related again to cell-centred physical quantities, and $(i-1/2,j,k)$, $(i+1/2,j,k)$, $(i,j-1/2,k)$, $(i,j+1/2,k)$, $(i,j,k-1/2)$, $(i,j,k+1/2)$ indices are related to the left and right-hand side control volume face values of each physical quantity in spatial directions X, Y, Z, respectively; which are appearing in the non-linear convective terms (3.23). For computing the dimensionless velocity component $V^{\star}$ of the intermediate velocity field (3.26), a hybrid FD/FV approach can be employed again [66] as

$$\begin{aligned} V^{\star}_{i,j,k} = V^{(n)}_{i,j,k} + \frac{\triangle\tau}{Re}\Bigg[&\frac{V_{i+1,j,k}-2V_{i,j,k}+V_{i-1,j,k}}{(\triangle X)^2}+\frac{V_{i,j+1,k}-2V_{i,j,k}+V_{i,j-1,k}}{(\triangle Y)^2}+\\ &+\frac{V_{i,j,k+1}-2V_{i,j,k}+V_{i,j,k-1}}{(\triangle Z)^2}\Bigg]^{(n)}-\triangle\tau\Bigg[\frac{\left(\widetilde{U}\widetilde{V}\right)_{i+1/2,j,k}-\left(\widetilde{U}\widetilde{V}\right)_{i-1/2,j,k}}{\triangle X}+\\ &+\frac{\widetilde{V}^2_{i,j+1/2,k}-\widetilde{V}^2_{i,j-1/2,k}}{\triangle Y}+\frac{\left(\widetilde{W}\widetilde{V}\right)_{i,j,k+1/2}-\left(\widetilde{W}\widetilde{V}\right)_{i,j,k-1/2}}{\triangle Z}\Bigg]^{(n)}, \end{aligned} \tag{3.32}$$

and for computing the dimensionless velocity component $W^{\star}$ of the intermediate velocity field (3.26), a hybrid FD/FV approach can also be used [66] as

$$W^{\star}_{i,j,k} = W^{(n)}_{i,j,k} + \frac{\triangle\tau}{Re}\left[\frac{W_{i+1,j,k} - 2W_{i,j,k} + W_{i-1,j,k}}{(\triangle X)^2} + \frac{W_{i,j+1,k} - 2W_{i,j,k} + W_{i,j-1,k}}{(\triangle Y)^2} + \right.$$
$$\left. + \frac{W_{i,j,k+1} - 2W_{i,j,k} + W_{i,j,k-1}}{(\triangle Z)^2}\right]^{(n)} - \triangle\tau\left[\frac{\left(\widetilde{U}\widetilde{W}\right)_{i+1/2,j,k} - \left(\widetilde{U}\widetilde{W}\right)_{i-1/2,j,k}}{\triangle X} + \right.$$
$$\left. + \frac{\left(\widetilde{V}\widetilde{W}\right)_{i,j+1/2,k} - \left(\widetilde{V}\widetilde{W}\right)_{i,j-1/2,k}}{\triangle Y} + \frac{\widetilde{W}^2_{i,j,k+1/2} - \widetilde{W}^2_{i,j,k-1/2}}{\triangle Z}\right]^{(n)}, \tag{3.33}$$

where the second-order Laplacian viscous terms $(1/Re)\nabla^2\mathbf{U}$ are discretised with a second-order accurate central cell-centred FD approximation scheme. The dimensionless pressure-Poisson Eq. (3.27), i.e., the pressure projection step can also be discretised with a second-order accurate central cell-centred FD approximation scheme [54] as follows:

$$\left[\frac{P_{i+1,j,k} - 2P_{i,j,k} + P_{i-1,j,k}}{(\triangle X)^2} + \frac{P_{i,j+1,k} - 2P_{i,j,k} + P_{i,j-1,k}}{(\triangle Y)^2} + \frac{P_{i,j,k+1} - 2P_{i,j,k} + P_{i,j,k-1}}{(\triangle Z)^2}\right]^{(n+1)} =$$
$$= \frac{1}{\triangle\tau}\left(\frac{U^{\star}_{i,j,k} - U^{\star}_{i-1,j,k}}{\triangle X} + \frac{V^{\star}_{i,j,k} - V^{\star}_{i,j-1,k}}{\triangle Y} + \frac{W^{\star}_{i,j,k} - W^{\star}_{i,j,k-1}}{\triangle Z}\right)^{(n)}, \tag{3.34}$$

where the first-order derivatives of the intermediate velocity field $\mathbf{U}^{\star}$ (3.26) are approximated with a first-order backward cell-centred finite difference scheme. The discretised pressure-Poisson Eq. (3.34) has been solved with the Successive Over-Relaxation (SOR) iterative method with a numerical value of the relaxation factor of $\omega_P = 1.7$. It is important to note that in the context of the unified FSAC-PP solution method, the approximate solution of the discretised dimensionless pressure-Poisson Eq. (3.34) is used as a smoothing iteration for the pressure field prediction. Therefore, only a few SOR sub-iteration steps are required to be performed for projecting the pressure field [54], because one of the advantageous features of the unified FSAC-PP solution approach is that the pressure field is obtained through the interaction between the numerical solution of the pseudo-time evolutionary perturbed continuity Eq. (3.25) and the spatially evolving numerical solution of the pressure-Poisson Eq. (3.27); in which case the numerical solution of the discretised dimensionless pressure-Poisson Eq. (3.34) serves to smooth the predicted approximate numerical values of the pressure field. Through comprehensive validations of the unified FSAC-PP method on different benchmark problems, Könözsy and Drikakis (2014) [54], Tsoutsanis et al. (2015) [87], and Teschner et al. (2018, 2019) [55], [56] provided numerical evidence that the FSAC-PP method through the interaction between the numerical solution of the pseudo-time evolutionary perturbed continuity Eq. (3.25) and the spatially

evolving numerical solution of the pressure-Poisson Eq. (3.27) could enhance the efficiency of the numerical solution of the Navier–Stokes Eq. (3.2). Note that the way of the computer code implementation of the FSAC-PP method from a computer programming aspect could also have an impact on its efficiency, e.g., parallelisation. In terms of the specification of the boundary conditions for the pressure field, fully Neumann-type homogeneous boundary conditions can be imposed and satisfied iteratively in which case a pressure value as an additive constant has be known at least in one point of the computational domain to avoid the singularity of the system of linear equations [88]. However, the pressure boundary conditions depend on the investigated specific physical problem in each case. After performing a few SOR sub-iterations for approximating an intermediate numerical solution of the discretised pressure-Poisson Eq. (3.34), the last step of the FSAC-PP algorithm—which is identical to the last step of the FS-PP method [52]—is to update the velocity field values. The velocity field update is carried out based on Eq. (3.28) for each velocity component U, V, W at pseudo-time level $(n+1)$ through the obtained approximate solution of the discretised pressure-Poisson Eq. (3.34) as

$$U_{i,j,k}^{(n+1)} = U_{i,j,k}^{\star} - \triangle\tau \left(\frac{P_{i+1,j,k} - P_{i,j,k}}{\triangle X} \right)^{(n+1)}, \tag{3.35}$$

$$V_{i,j,k}^{(n+1)} = V_{i,j,k}^{\star} - \triangle\tau \left(\frac{P_{i,j+1,k} - P_{i,j,k}}{\triangle Y} \right)^{(n+1)}, \tag{3.36}$$

$$W_{i,j,k}^{(n+1)} = W_{i,j,k}^{\star} - \triangle\tau \left(\frac{P_{i,j,k+1} - P_{i,j,k}}{\triangle Z} \right)^{(n+1)}, \tag{3.37}$$

where the first-order pressure gradient terms on the right-hand side is approximated with a first-order forward cell-centred FD scheme. The computation of the non-linear convective terms $\nabla \cdot \left(\widetilde{\mathbf{U}} \otimes \widetilde{\mathbf{U}} \right)$ for predicting the intermediate velocity field based on the discretised dimensionless scalar Eqs. (3.31)–(3.33) was carried out by using a characteristics-based (CB) Godunov-type numerical approximation [54], [62], [66] which can be derived from the hyperbolic system of Eqs. (3.7)–(3.8) of the AC formulation of Chorin [51]. The tilde notation indicated the CB Godunov-type discretisation of the non-linear convective terms $\nabla \cdot \left(\widetilde{\mathbf{U}} \otimes \widetilde{\mathbf{U}} \right)$ in the discrete scalar Eqs. (3.31)–(3.33) in which case the characteristic velocity components $\widetilde{U}$, $\widetilde{V}$ and $\widetilde{W}$ can be computed [54] as follows:

$$\begin{bmatrix} \widetilde{U} \\ \widetilde{V} \\ \widetilde{W} \end{bmatrix} = \frac{1}{2} \begin{bmatrix} U_1 + U_2 + sign(\lambda_0)(U_1 - U_2) \\ V_1 + V_2 + sign(\lambda_0)(V_1 - V_2) \\ W_1 + W_2 + sign(\lambda_0)(W_1 - W_2) \end{bmatrix}^{(n)} + \begin{bmatrix} \widetilde{X} \\ \widetilde{Y} \\ \widetilde{Z} \end{bmatrix} \left(\frac{P_1 - P_2 + R^*}{2\sqrt{\lambda_0^2 + \beta}} \right)^{(n)}, \tag{3.38}$$

where the subscripts '1' and '2' are related to the left- and right-hand side control volume face values of each velocity component denoted by sub-indices $i-1/2, j, k$ (left), $i+$

$1/2, j, k$ (right), $i, j-1/2, k$ (left), $i, j+1/2, k$ (right), $i, j, k-1/2$ (left), $i, j, k+1/2$ (right) in each spatial direction X, Y, Z, respectively; which can also be called intercell face values of non-linear convective terms $\nabla \cdot \left(\widetilde{\mathbf{U}} \otimes \widetilde{\mathbf{U}}\right)$ in the discretised scalar Eqs. (3.31)–(3.33) in the context of a hybrid FD/FV discretisation approach. These intercell numerical values in Eq. (3.38) are approximated by using a polynomial interpolation, where $\widetilde{X}$, $\widetilde{Y}$, $\widetilde{Z}$ are the spatial components of metrics [62], [66]. The pressure difference $(P_1 - P_2)$ in Eq. (3.38) can be computed based on the numerical solution of the discretised perturbed continuity Eq. (3.30), and the auxiliary function R^* in Eq. (3.38) is expressed [54] by

$$R^* = \lambda_2 \left[\tilde{X}(U_0 - U_1) + \tilde{Y}(V_0 - V_1) + \tilde{Z}(W_0 - W_1)\right]^{(n)}$$

$$-\lambda_1 \left[\tilde{X}(U_0 - U_2) + \tilde{Y}(V_0 - V_2) + \tilde{Z}(W_0 - W_2)\right]^{(n)}. \tag{3.39}$$

The characteristic velocity components $\widetilde{U}$, $\widetilde{V}$, $\widetilde{W}$ (3.38) and the auxiliary function R^* (3.39) can be computed based on the three distinct eigenvalues of the CB scheme [54] as

$$\lambda_0 = \widetilde{U}\widetilde{X} + \widetilde{V}\widetilde{Y} + \widetilde{W}\widetilde{Z}, \tag{3.40}$$

$$\lambda_1 = \lambda_0 + \sqrt{\lambda_0^2 + \beta}, \tag{3.41}$$

$$\lambda_2 = \lambda_0 - \sqrt{\lambda_0^2 + \beta}, \tag{3.42}$$

The characteristic velocity components $\widetilde{U}$, $\widetilde{V}$, $\widetilde{W}$ (3.38) were derived by using the Riemann method [89] for incompressible fluid flows [62], [66] which includes the solution of the local Riemann problem on the computational domain to ensure the numerical prediction of the physically correct fluid flow direction, thus

$$sign(\lambda_0) = \begin{cases} -1 & \lambda_0 > 0 \\ 1 & \lambda_0 < 0 \end{cases}. \tag{3.43}$$

The CB scheme (3.38) is called Godunov-type, because after interpolating the intercell physical quantities denoted by the subscripts '1' and '2' in Eq. (3.38), the solution of the local Riemann problem [66], [89] is included in the numerical prediction of non-linear convective terms $\nabla \cdot \left(\widetilde{\mathbf{U}} \otimes \widetilde{\mathbf{U}}\right)$ in the discretised intermediate momentum Eqs. (3.31)–(3.33) [86]. The discretised system of Eqs. (3.30)–(3.33) and Eqs. (3.35)–(3.37) has been solved explicitly in each computational cell and the discretised pressure-Poisson Eq. (3.34) has been solved with the SOR implicit iterative technique using only a few sub-iteration steps to smooth the pressure field solution. Therefore, the numerical approach overviewed above is a semi-implicit approach to the numerical solution of the governing Eqs. (3.25)–(3.28) of the unified FSAC-PP method [54]. The first-order pseudo-temporal accuracy of the numerical solution of the discretised dimensionless perturbed continuity Eq. (3.30) coupled with the discretised intermediate momentum Eqs. (3.31)–(3.33) was further improved by employing a fourth-order explicit Runge-Kutta pseudo-time integration scheme

[54], [66], [90], where the pseudo-time step size can be derived from an eigenvalue analysis in conjunction with the derivation of the CB Godunov-type scheme (3.38) to provide stability of the explicit numerical solution (see more details in [86]). The pseudo-time step was locally computed, i.e., in each computational cell [54], [66] as

$$\Delta\tau_{i,j,k}^{\text{Inviscid}} = \frac{\text{CFL}_{\text{Inviscid}}}{\left[\max_{\text{m=1-4}}\left(|\lambda_1|,|\lambda_2|\right)_m\right]_{i,j,k}}, \tag{3.44}$$

$$\Delta\tau_{i,j,k}^{\text{Viscous}} = \frac{\text{CFL}_{\text{Viscous}} Re}{4\left[\max_{\text{n=1,2,3}}\left(dl_n\right)\right]_{i,j,k}}, \tag{3.45}$$

where the Courant–Friedrichs–Lewy (CFL) numbers $\text{CFL}_{\text{Inviscid}}$ and $\text{CFL}_{\text{Viscous}}$ are taken into account for the inviscid and viscous terms in the dimensionless governing Eqs. (3.25)–(3.28), and dl_n is the computational cell dimension computed based on the local spatial coordinate directions [54], [66]. To provide the stability of the explicit numerical solution of the discretised system of Eqs. (3.30)–(3.33), the local pseudo-time step size can be computed based on the minimum value of Eqs. (3.44) and (3.45) [54] as

$$\Delta\tau_{i,j,k} = \gamma_s \cdot \min\left(\Delta\tau_{i,j,k}^{\text{Inviscid}}, \Delta\tau_{i,j,k}^{\text{Viscous}}\right), \tag{3.46}$$

where $\gamma_s \in]\,0,1]$ is a safety factor of the numerical stability [91], e.g., $\gamma_s = 0.5$. To ensure stability, consistency and convergence of the numerical procedure, the parameters β (3.29) and γ_s have to be adjusted for each investigated physical problem [60], [92]. To satisfy the continuity Eq. (3.1) for stationary incompressible flows, the FSAC-PP numerical procedure for solving the discretised system of Eqs. (3.30)–(3.33) has to be repeated until each pseudo-time derivative vanishes, i.e., $\left[p^{(n)} - p^{(n-1)}\right]/\triangle\tau$ in the perturbed continuity Eq. (3.25) and $\left[\mathbf{U}^{\star} - \mathbf{U}^{(n)}\right]/\triangle\tau$ in the intermediate velocity field Eq. (3.26) will become equal to zero or a very small user-defined threshold value ε_s [54], thus

$$\max\left(\beta\left|\nabla\cdot\mathbf{U}^{(n+1)} - \nabla\cdot\mathbf{U}^{(n)}\right|, \left|\frac{\mathbf{U}^{(n+1)} - \mathbf{U}^{(n)}}{\Delta\tau}\right|\right) \leq \varepsilon_s. \tag{3.47}$$

Another possible way to measure the numerical convergence of the unified FSAC-PP method is the computation of the maximum value of the Runge-Kutta pseudo-time marching residuals between two consecutive pseudo-time levels [54] as

$$\max\left(\left|\frac{\mathbf{U}_{RK}^{(n+1)} - \mathbf{U}_{RK}^{(n)}}{\Delta\tau}\right|\right) \leq \varepsilon_s, \tag{3.48}$$

where $\mathbf{U}_{RK} = \begin{bmatrix} P/\beta & U & V & W \end{bmatrix}^T$ is a vector which can be defined in conjunction with an explicit fourth-order Runge–Kutta pseudo-time advancing scheme as described in [54]. The pseudo-time marching iterations have to be performed until the stationary numerical solution of Eqs. (3.25)–(3.28) is achieved within a very small threshold value ε_s [54]. To

further accelerate the convergence, i.e., further enhance the efficiency of the FSAC-PP numerical procedure, a full-multigrid and full-approximation storage (FMG-FAS) algorithm [63], [64] was coupled with the numerical solution. Note that the FSAC-PP solution method [54] can be used for solving unsteady incompressible fluid flow problems using a dual-time stepping procedure which was excluded from the present overview. Therefore, one can find the complete description of the FSAC-PP algorithm for unsteady and steady-state incompressible fluid flows in the work of Könözsy and Drikakis (2014) [54].

3.3.2 Overview of simulation results on benchmark problems

The unified FSAC-PP algorithm has been implemented in an in-house FORTRAN 90/95 code. The verification of the code and the validation of the FSAC-PP Navier–Stokes solver were carried out [54] on different benchmark problems in comparison with a simplified analytical solution, simulation results obtained by the AC and FS-PP methods, and computational and/or experimental data already available in the literature. For two-dimensional benchmark test cases, the control cell face values, i.e., intercell flux values of each physical quantity—which are corresponding to grid indices $(i-1/2, j)$, $(i+1/2, j)$, $(i, j-1/2)$ and $(i, j+1/2)$—were approximated by employing first-, second-, third-, fifth- and ninth-order interpolation polynomials in the discretisation of the non-linear convective terms $\nabla\cdot\left(\widetilde{\mathbf{U}}\otimes\widetilde{\mathbf{U}}\right)$ in conjunction with the CB Godunov-type scheme (3.38). In the cases of fifth- and ninth-order interpolations, Weighted Essentially Non-Oscillatory (WENO) schemes have been employed and their implementations are well documented in [86], [93]–[96]. For validation purposes, mesh sensitivity and numerical convergence investigations were carried out by Könözsy and Drikakis (2014) [54] to give insight into the accuracy and efficiency properties of the unified FSAC-PP solution method. The numerical convergence of the unified FSAC-PP method has been presented through the maximum values of Runge–Kutta residuals RK_{maxres} (3.48) versus the total number of multigrid iterations N_{mg}, e.g., see Figure 3.1 and further details in [54].

The first benchmark validataion test problem was a two-dimensional $100\mu m$ long horizontal microfluidic channel with the height of $10\mu m$. The pressure-driven incompressible stationary laminar flow was investigated at different Re numbers from 0.0001 to 10 with the number of 216 numerical simulations. It is always important to assess the performance of a Navier–Stokes solver at very low, moderate and high Re numbers. It is known from the literature [60], [86] that the accuracy and efficiency of the AC method of Chorin [51] could break down at $Re \ll 1$. The motivation behind the development of the unified FSAC-PP method was also to compute accurately and efficiently very low Re number flows ($Re \ll 1$) incorporating the advantageous accuracy properties of the CB Godunov-type discretisation schemes into the FS-PP method of Chorin [52] in conjunction with the discretisation of the non-linear convective terms in the momentum Eqs. (3.31)–(3.33). Könözsy and Drikakis (2014) [54] carried out a detailed and comprehensive validation of the unified FSAC-PP method for laminar flows in a microfluidic channel including a mesh sensitivity study using four different mesh densities; where the very coarse, coarse, medium and fine meshes consisted of 200, 800, 3200 and 7200 (180×40) computational

cells, respectively. The parameter β and the CFL numbers $\text{CFL}_{\text{Inviscid}}$, $\text{CFL}_{\text{Viscous}}$ were equals to 10 and 0.2, 0.15 at $Re = 10$ and 10^6 and 0.015, 0.015 at $Re = 0.0001$ [54], respectively. For solving the discretised pressure-Poisson Eq. (3.34) on the fine mesh in the context of the FSAC-PP method for this test case, the number of the SOR sub-iterations has to be selected between 1 and 10 to ensure a numerically stable interaction between the numerical solution of the perturbed continuity Eq. (3.25) and the pressure-Poisson Eq. (3.27), thus enhancing the efficiency of the FSAC-PP numerical procedure. The complete numerical setup along with the boundary condition specifications can be found in [54].

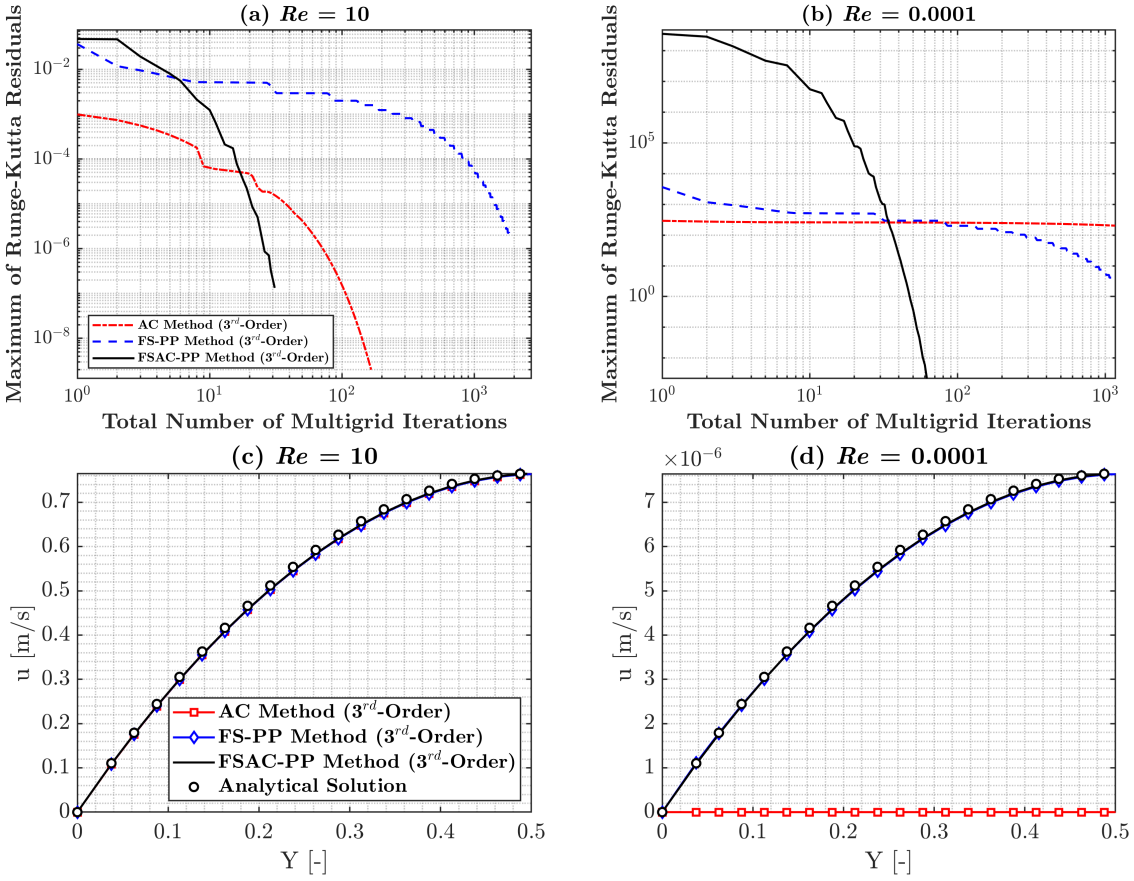

Figure 3.1: Numerical convergence histories of the AC, FS-PP and FSAC-PP methods (a) at $Re = 10$ and (b) at $Re = 0.0001$; and numerically predicted fully-developed velocity profiles at the outlet section of the microfluidic channel in comparison with a simplified analytical solution (c) at $Re = 10$ and (d) at $Re = 0.0001$ [54, pp. 1156-1157][2]

[2]Parts of Figure 3.1 and parts of simulation results overviewed here were first published in the article entitled as "A Unified Fractional-Step, Artificial Compressibility and Pressure-Projection Formulation for Solving the Incompressible Navier–Stokes Equations", Authors: László Könözsy and Dimitris Drikakis, *Communications in Computational Physics*, Vol. 16, No. 5, pp. 1135-1180, November 2014, ISSN: 1815-2406, published by Global Science Press.

Using a third-order interpolation scheme [66], [97] for computing the non-linear convective terms with the CB Godunov-type scheme (3.38) in the momentum Eqs. (3.31)–(3.33), the convergence histories, i.e., the maximum values of Runge–Kutta residuals RK_{maxres} (3.48) versus the total number of multigrid iterations N_{mg} at $Re = 10$ and $Re = 0.0001$ are shown in Figures 3.1(a) and 3.1(b) [54, p. 1157], respectively. At $Re = 10$, the lowest maximum values of Runge–Kutta residuals RK_{maxres} of $0.19995 \cdot 10^{-8}$, $0.18354 \cdot 10^{-5}$, $0.13352 \cdot 10^{-6}$ were achieved with the AC, FS-PP and FSAC-PP solution methods after performing the total numbers of multigrid iterations N_{mg} of 166, 1878 and 31 [54, p. 1158], respectively. At $Re = 0.0001$, the lowest maximum values of Runge–Kutta residuals RK_{maxres} of $0.20293 \cdot 10^{3}$, 3.34202, $0.15059 \cdot 10^{-4}$ were achieved with the AC, FS-PP and FSAC-PP solution methods after performing the total numbers of multigrid iterations N_{mg} of 1165, 1161 and 123 [54, p. 1159], respectively. After performing these numbers of multigrid iterations, the maximum values of Runge–Kutta residuals (3.48) did not exhibit any significant changes. For these two Re numbers, the FSAC-PP method required the smallest number of multigrid iterations to achieve the lowest maximum value of Runge–Kutta residuals (3.48). Using a third-order interpolation scheme [66], [97] for computing the convective terms with the CB scheme (3.38) in Eqs. (3.31)–(3.33), the numerically predicted fully-developed velocity profiles with the AC, FS-PP and FSAC-PP methods in comparison with a simplified analytical solution at the outlet section of the microfluidic channel at $Re = 10$ and $Re = 0.0001$ are shown in Figures 3.1(c) and 3.1(d) [54, p. 1156], respectively. At $Re = 10$, the relative errors of the numerically predicted fully-developed velocity profiles with the AC, FS-PP and FSAC-PP methods in comparison with a simplified analytical solution were within 0.2% when a third-order interpolation scheme was employed for computing the non-linear convective terms with the CB scheme (3.38). However, at $Re = 0.0001$, the AC method failed to predict any physically correct results compared to the FS-PP and FSAC-PP methods and the simplified analytical solution [54]. For pressure-driven incompressible stationary laminar flows in a horizontal microfluidic channel, the simulation results in [54] suggest that in terms of accuracy and efficiency, a further improvement can be achieved with the use of the unified FSAC-PP method in the numerical prediction of laminar flows at low Re numbers.

The two-dimensional shear-driven flow in a unit square cavity is one of the most well-known classical benchmark problems for validating a Navier–Stokes solver. Therefore, as a second test case, two-dimensional laminar flows in a lid-driven unit square cavity were investigated in [54] in conjunction with the AC, FS-PP and FSAC-PP solution methods at $Re = 100$, 400 and 1000. For this benchmark problem, accurate and reliable numerical data are available for the dimensionless velocity profiles along the horizontal- and vertical centre-lines of the unit square cavity which were published by Ghia et al. [98]. The same number of computational mesh points of 129×129, i.e., 128×128 cells was used as in the reference work of Ghia et al. [98]. For each Re number, the parameter β and the CFL numbers $\mathrm{CFL}_{\mathrm{Inviscid}}$, $\mathrm{CFL}_{\mathrm{Viscous}}$ were equals to 10 and 0.5, 0.5 [54], respectively. At the side walls, Dirichlet-type no-slip boundary conditions were imposed, i.e., the dimensionless velocity components U and V were equal to zero. The lid is moving on the top of the

unit square cavity where also Dirichlet-type boundary conditions were imposed as $U_{lid} = 1$ and $V = 0$. The homogeneous Neumann-type boundary conditions for the dimensionless pressure field were iteratively satisfied along the boundary of the cavity. More details on the simulation setup and boundary condition specifications can be found in [54]. The streamline patterns of the primary and secondary vortices numerically predicted with the FSAC-PP method using a 1^{st}-order interpolation scheme for computing the convective terms with the CB scheme (3.38) at $Re = 100$, 400 and 1000 are shown in Figure 3.2.

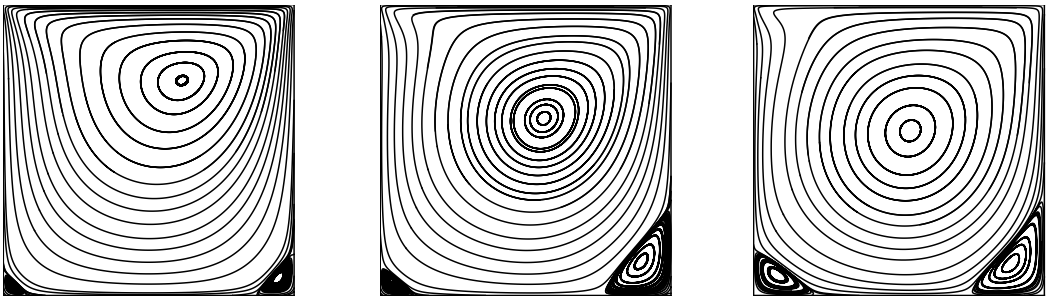

(a) FSAC-PP (1^{st}-Order) [54] (b) FSAC-PP (1^{st}-Order) [54] (c) FSAC-PP (1^{st}-Order) [54]

Figure 3.2: Numerically predicted primary and secondary vortices with the FSAC-PP method in a 2D lid-driven cavity using a 1^{st}-order interpolation scheme for computing the convective terms with the CB scheme (3.38) at $Re = 100$, 400 and 1000 [54, p. 1170][3]

It has been observed that the FSAC-PP method was capable of capturing the physically correct streamline patterns including the secondary vortices at the corners of the unit square cavity at each investigated Re numbers. Furthermore, the FSAC-PP method accurately predicted the dimensionless velocity profiles along the horizontal and vertical centre-lines of the cavity in comparison with the numerical data of Ghia et al. [98] even at $Re = 1000$ when only a 1^{st}-order interpolation scheme was employed which are shown in Figures 3.3(a) and 3.3(b). At $Re = 1000$, the AC and FS-PP methods failed to predict the physically correct distribution of the dimensionless velocity components along the horizontal and vertical centre-lines compared to the reference data of Ghia et al. [98] when a 1^{st}-order interpolation scheme was employed for this 2D shear-driven laminar flow. It could mean that not only the choice of the order of the interpolation scheme has an impact on the accuracy of the numerical solution procedure, i.e., the choice of the pressure-velocity (PV) coupling method matters as well. This observation was pointed out

[3] Streamline patterns of Figure 3.2 with the FSAC-PP method using a 1^{st}-order interpolation scheme for computing the convective terms with the CB scheme (3.38) were first published in the article entitled as "A Unified Fractional-Step, Artificial Compressibility and Pressure-Projection Formulation for Solving the Incompressible Navier–Stokes Equations", Authors: László Könözsy and Dimitris Drikakis, *Communications in Computational Physics*, Vol. 16, No. 5, pp. 1135-1180, November 2014, ISSN: 1815-2406, published by Global Science Press.

by Teschner, Könözsy and Jenkins (2018) [55, p. 11] related to the numerical investigation of the behaviour of the AC and FSAC-PP solution methods for a bifurcating laminar flow in a sudden expansion channel at different *Re* numbers. Note that the use of lower-order interpolation schemes (e.g., 1^{st}-order) in the framework of the FSAC-PP method could also reduce computational times, because the computation of lower-order schemes requires less mathematical operations than the computation of higher-order polynomials for computing the convective terms with the CB Godunov-type scheme (3.38) [54].

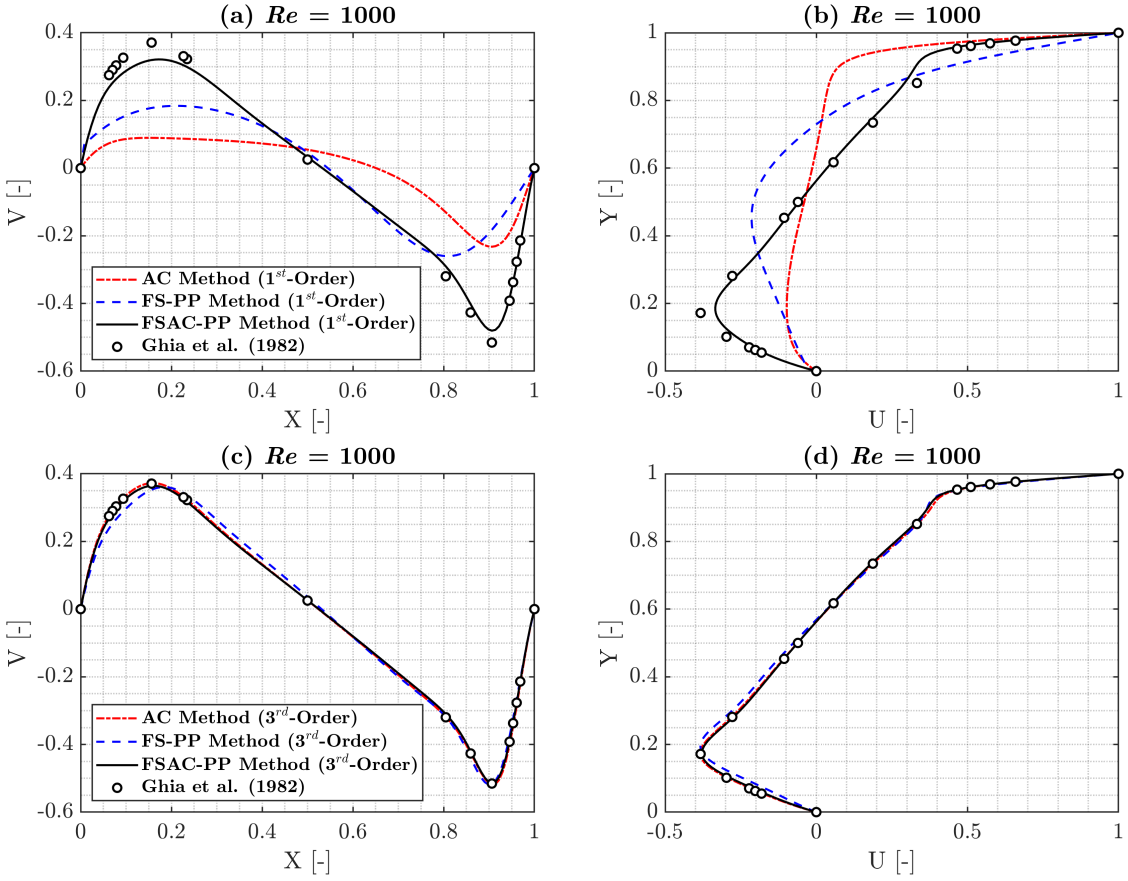

Figure 3.3: Fully-developed dimensionless velocity profiles numerically predicted in a 2D lid-driven cavity with the AC, FS-PP and FSAC-PP methods along the horizontal centre-line using (a) 1^{st}-order and (c) 3^{rd}-order interpolation schemes and along the vertical centre-line using (b) 1^{st}-order and (d) 3^{rd}-order interpolation schemes in comparison with the numerical data of Ghia et al. [98] at $Re = 1000$ [54, p. 1165 & p. 1167][4]

[4]Parts of Figure 3.3 and parts of simulation results overviewed here were first published in the article entitled as "A Unified Fractional-Step, Artificial Compressibility and Pressure-Projection Formulation for Solving the Incompressible Navier–Stokes Equations", Authors: László Könözsy and Dimitris Drikakis, *Communications in Computational Physics*, Vol. 16, No. 5, pp. 1135-1180, November 2014, ISSN: 1815-2406, published by Global Science Press.

It can be seen in Figures 3.3(c) and 3.3(d) that the AC, FS-PP and FSAC-PP methods were capable of accurately predicting the physically correct dimensionless velocity distributions along the horizontal and vertical centre-lines at $Re = 1000$ in comparison with the numerical data of Ghia et al. [98] when a 3^{rd}-order interpolation scheme was employed for computing the convective terms with the CB scheme (3.38). A detailed error analysis related to this benchmark problem can be found in [54]. It has been observed in [54] that the use of at least a 3^{rd}-order interpolation scheme is required for accurately predicting the physically correct fluid flow features at low Re number laminar flows.

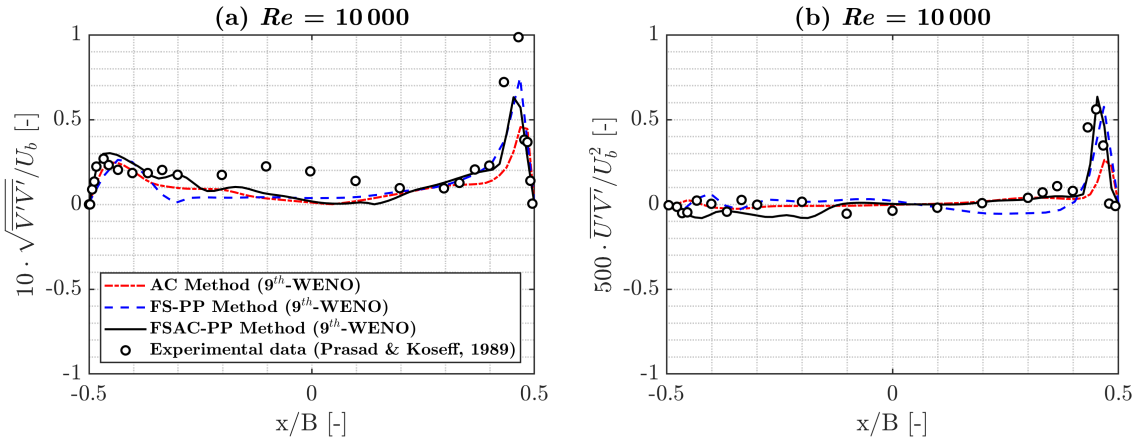

Figure 3.4: Numerically predicted Reynolds stress distributions with the AC, FS-PP and FSAC-PP methods along the horizontal centre-line of a 3D lid-driven cavity; (a) dimensionless Reynolds stress profile of $10 \cdot \sqrt{\overline{V'V'}}/U_b$; and (b) dimensionless principal Reynolds shear stress profile of $500 \cdot \overline{U'V'}/U_b^2$ in comparison with the experimental data of Prasad and Koseff [99] at $Re = 10000$ [54, p. 1176][5]

The unsteady dual-time stepping version of the unified FSAC-PP solution method has been tested in [54] for a turbulent flow in a 3D lid-driven cavity at $Re = 10000$ in the context of the Implicit Large Eddy Simulation (ILES) technique which can also be called "Under-Resolved Direct Numerical Simulation (DNS)" approach [100, p. 475]. In that case, the Navier-Stokes Eq. (3.2) is solved by employing high-resolution Godunov-type schemes in the instantaneous velocity field on a coarser mesh compared to the Kolmogorov scale-like fine mesh resolutions used in DNS techniques [101], [102]. Furthermore, there are no additional source terms involved in the Navier–Stokes Eq. (3.2) and there is no need to solve additional transport equations for turbulence modelling. It

[5]Parts of Figure 3.4 and parts of simulation results overviewed here were first published in the article entitled as "A Unified Fractional-Step, Artificial Compressibility and Pressure-Projection Formulation for Solving the Incompressible Navier–Stokes Equations", Authors: László Könözsy and Dimitris Drikakis, *Communications in Computational Physics*, Vol. 16, No. 5, pp. 1135-1180, November 2014, ISSN: 1815-2406, published by Global Science Press.

is possible to recover the fluctuating velocity field from the numerically simulated instantaneous and computed mean velocity fields; thus the prediction of the elements of the anisotropic Reynolds stress tensor was carried out in [54]. For this benchmark problem, the fine mesh spatial resolution consisted of $64 \times 64 \times 64$ computational points, i.e., $63 \times 63 \times 63$ control volume cells [54, p. 1173]. The 3D cavity length, height and width were equal to $B = 150\,mm$ taken from the experimental work of Prasad and Koseff [99]. The most accurate agreement has been obtained for the non-dimensionalised distributions of the second main diagonal element of the anisotropic Reynolds stress tensor and the principal turbulent shear stress at $Re = 10\,000$ in comparison with the experimental data of Prasad and Koseff [99]; which are shown in Figures 3.4(a) and 3.4(b). It means that the unified FSAC-PP solution method can be employed for solving incompressible turbulent flow problems in the context of the ILES, i.e., Under-Resolved DNS technique which could provide valuable insight into the physical behaviour of the instantaneous and fluctuating velocity fields. Therefore, it can be linked to the development of anisotropic URANS/RANS turbulence modelling approaches which subject area were overviewed in Chapter 2. It has also been found in [54] for the 3D lid-driven cavity test case at $Re = 10\,000$ that the FSAC-PP method required the least computational time compared to the AC and FS-PP solution methods using a 9^{th}-order WENO scheme for computing the non-linear convective terms in the Navier–Stokes Eq. (3.2). Chaudhary, Könözsy and Rana (2022) [100] investigated further the accuracy and efficiency of high-resolution Godunov-type schemes using Under-Resolved DNS technique for simulating nearly hypersonic, unsteady, viscous, compressible, chemically reacting turbulent magnetogasdynamic flows, e.g., behind cuboid geometries. They concluded that the ILES, i.e., Under-Resolved DNS technique in conjunction with high-resolution Godunov-type schemes can accurately capture the physically correct shock structures behind cuboid objects. Therefore, the Under-Resolved DNS technique can be applied to both incompressible and compressible flows with reliable accuracy [101], [102]. However, note that the numerical solution of the compressible Navier–Stokes equations was not the subject of the review presented here.

Teschner, Könözsy and Jenkins (2018, 2019) [55], [56] further investigated the impact of using different numerical schemes on the accuracy of the simulations performed with the AC and FSAC-PP method for different benchmark problems at different Re numbers. One of the benchmark problems was a sudden expansion channel where the numerical investigation of bifurcating laminar flows was carried out at different Re numbers in [55]. In that case, the total length of the computational domain was equal to $30\,s_h$ which was slightly longer than the experimental test section to achieve the fully-developed velocity distribution in the simulations at the outlet section of the sudden expansion channel; where s_h is the step-height [55]. The computational results in [55] were compared to the experimental data of Fearn et al. [103]. The contours of the axial velocity distribution numerically predicted with the AC and FSAC-PP solution methods in a sudden expansion channel [55] are shown in Figures 3.5(a) and 3.5(b). The dimensionless axial velocity profiles predicted by using different numerical schemes for computing the non-linear convective terms at $Re = 80$ are shown in Figures 3.5(c) and 3.5(d).

(a) AC Method (Axial velocity contour) [55, p. 10]

(b) FSAC-PP Method (Axial velocity contour) [55, p. 10]

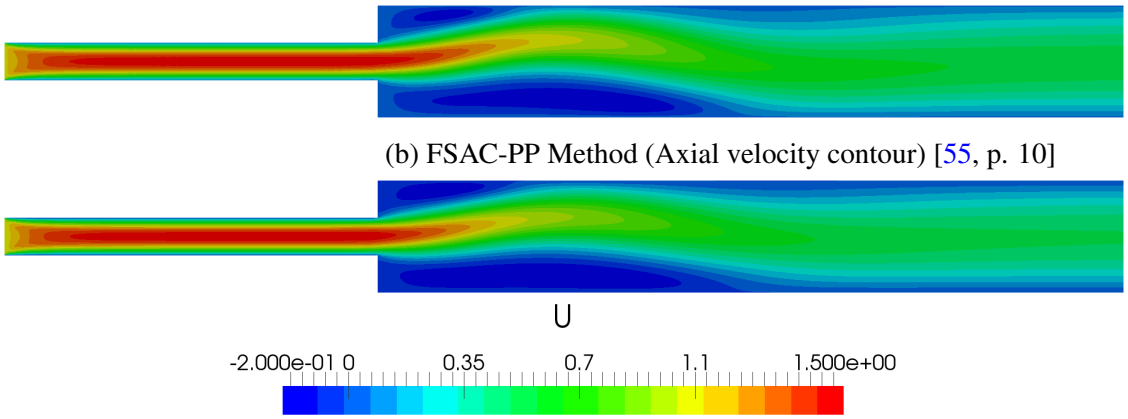

Dimensionless axial velocity profiles [55, pp. 10-11]

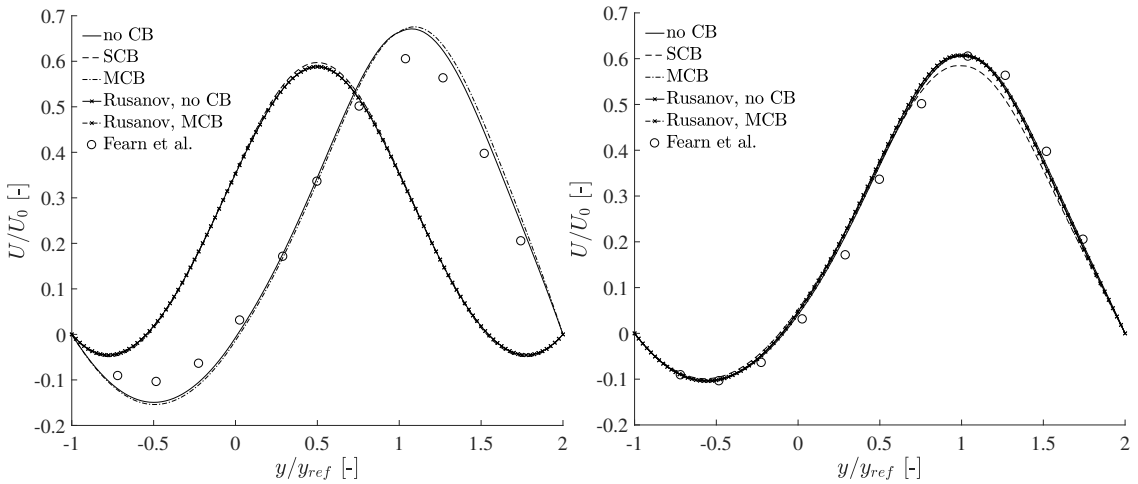

(c) AC Method at $Re = 80$ [55, p. 10]

(d) FSAC-PP Method at $Re = 80$ [55, p. 11]

Figure 3.5: Numerically predicted axial velocity contours with (a) the AC method and (b) the FSAC-PP method and the dimensionless axial velocity profiles along the vertical direction predicted at the location of $x/s_h = 5$ with (c) the AC method and (d) the FSAC-PP method by using different numerical discretisation schemes for computing the non-linear convective terms in laminar flow simulations in a sudden expansion channel in comparison with the experimental data of Fearn et al. [103] at $Re = 80$ [55, pp. 10-11][6]

[6]Parts of Figure 3.5 and simulation results here were first published in the article entitled as "Predicting Non-linear Flow Phenomena Through Different Characteristics-Based Schemes", Authors: Tom-Robin Teschner, László Könözsy and Karl W. Jenkins, *Aerospace*, Vol. 5, No. 1:22, pp. 1-20, 2018, published by Multidisciplinary Digital Publishing Institute under CC BY license.

It can be seen in Figures 3.5(c) and 3.5(d) that the dimensionless axial velocity profiles at the location of $x/s_h = 5$ were accurately predicted with the FSAC-PP method in comparison with the measurement of Fearn et al. [103] at $Re = 80$, irrespective of the numerical scheme employed in the simulations, e.g., single-directional CB (SCB) scheme, multi-directional CB (MCB) scheme [56] with the inclusion of the Rusanov Riemann solver [96] for computing the convective terms. It could mean again that not only the selection of the numerical scheme influences the accuracy of the numerical solution, because the selection of the pressure-velocity (PV) coupling method also matters as was pointed out in [55, p. 11]. For predicting bifurcating laminar flows in a sudden expansion channel at different *Re* numbers, Teschner et al. [55, p. 17] found the FSAC-PP method required the least computational time compared to the AC method and the corresponding CPU time comparisons at different *Re* numbers are shown in Figures 3.6(a) and 3.6(b)

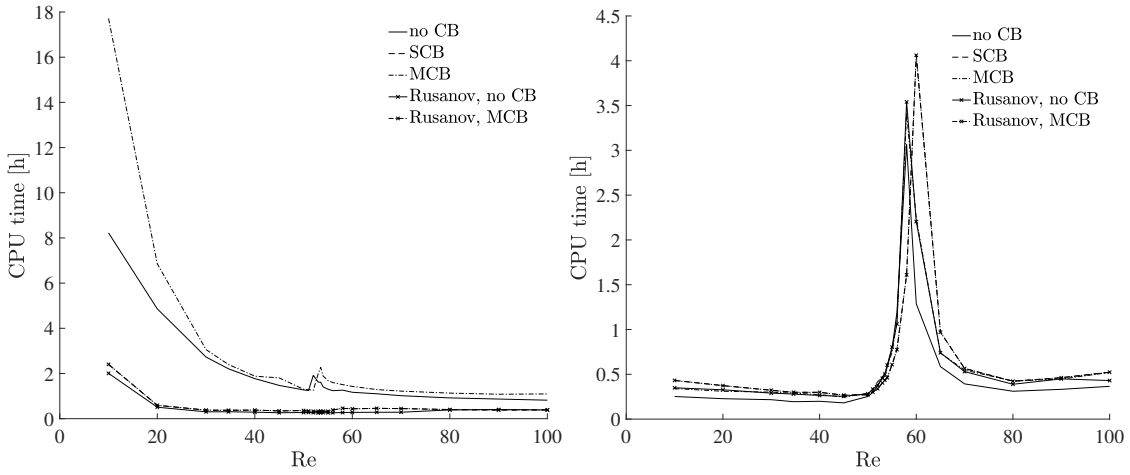

(a) AC Method, *Re* vs. CPU time [55, p. 17] (b) FSAC-PP Method, *Re* vs. CPU time [55, p. 17]

Figure 3.6: Measured CPU times of the AC and FSAC-PP methods for predicting bifurcating laminar flows in a sudden expansion channel at different *Re* numbers [55, p. 17][7]

After reviewing the theoretical background of the unification of the AC and FS-PP methods of Chorin [51], [52] based on the work of Könözsy and Drikakis (2014) [54] and reviewing validated simulation results on different benchmark problems in [54] and [55], it can be concluded that advances have been achieved with the FSAC-PP method in [54], [55] in the terms of accuracy and efficiency in the context of pseudo-transient methods, especially at very low and moderately high *Re* numbers. Therefore, the development of a two-stage pseudo-transient pressure-velocity (PV) coupling solution method, proposed by Könözsy (2017) [57], will be reviewed and discussed in the next Section 3.4.

[7] Figure 3.6 and simulation results here were first published in the article entitled as "Predicting Non-linear Flow Phenomena Through Different Characteristics-Based Schemes", Authors: Tom-Robin Teschner, László Könözsy and Karl W. Jenkins, *Aerospace*, Vol. 5, No. 1:22, pp. 1-20, 2018, published by Multidisciplinary Digital Publishing Institute under CC BY license.

3.4 Development of a two-stage pseudo-transient solution method

3.4.1 Review of the background of the method development

The simulation results reviewed in Subsection 3.3.2 suggest that the pseudo-transient approach to the solution of the stationary Navier–Stokes equations could improve accuracy, efficiency and convergence properties of the numerical procedure for solving incompressible fluid flow problems. Toutant (2017) [104] derived a general and exact pressure evolution equation from the compressible Navier–Stokes equations which could replace the pressure-Poisson equation for incompressible, isothermal flows at low Mach numbers. For incompressible flows, Toutant (2018) [105] validated the general pressure evolution equation for different benchmark problems. Dupuy et al. (2020) [106] proposed an artificial pressure evolution equation for solving the incompressible Navier–Stokes equations and validated it for wall-bounded flows. They highlighted that their approach can improve the accuracy and convergence properties of the numerical solution. Furthermore, there is no need to solve a pressure-Poisson equation when a pressure evolution equation is employed; thus a local system of equations can be obtained and the explicit discretisation of the governing equations is highly parallelisable with low memory requirements [106]. Harlow and Welch (1965) [59] pointed out that the collocated arrangement of the primitive variables, i.e., the collocated placement of the scalar components u, v, w of the velocity vector $\mathbf{u}$ and the pressure p on the computational mesh could lead to an oscillatory pressure field behaviour when a pressure-Poisson equation is solved leading to a non-physical solution of the system of incompressible governing equations. Harlow and Welch (1965) [59] introduced the staggered arrangement of the primitive variables u, v, w, p to overcome this problem and their approach is known as Marker and Cell (MAC) projection method in the literature. The staggered discretisation of the incompressible Navier–Stokes equations was revisited in the literature in many occasions to avoid the oscillatory pressure field solution when a collocated arrangement of the primitive variables u, v, w and p is used on a computational mesh, e.g., in the book of Griebel et al. (1998) [88]. Könözsy (2017) [57][8]proposed, derived and implemented a pseudo-transient pressure evolution equation leading to a two-stage pseudo-transient pressure-velocity (PV) coupling algorithm for solving the incompressible stationary Navier–Stokes equations at low Re numbers. This approach could also replace the solution of a pressure-Poisson equation for incompressible flows and is different from recent developments in [104]–[107]. The motivation behind the development of a two-stage pseudo-transient PV coupling algorithm was to overcome the oscillatory pressure field solution when the primitive variables u, v, w, p have a collocated arrangement on the computational mesh points.

[8]Some parts of the theory and equations overviewed here in Section 3.4 were first published in the work entitled as "Pseudo-Transient Pressure-Momentum Coupling Method for Low-Speed Incompressible Flows", Author: László Könözsy, *In: MultiScience - XXXI. microCAD International Multidisciplinary Scientific Conference, University of Miskolc, Hungary*, CD-ROM, ISBN 978-963-358-132-2, 20-21 April 2017, published by the University of Miskolc.

3.4.2 Derivation of a pseudo-transient pressure evolution equation

In this Section, we review the development of the two-stage pseudo-transient pressure-momentum coupling algorithm proposed by Könözsy (2017) [57] which can be derived either from the MAC pressure projection formulation of Harlow and Welch (1965) [59] or the FS-PP algorithm of Chorin (1968) [52]. From a theoretical point-of-view, as a first step of the derivation of a pseudo-transient pressure evolution equation, it is important to show that the two-stage pressure projection method of Harlow and Welch [59] and the three-stage FS-PP method of Chorin [52] are identical. For the sake of completeness, the FS-PP formulation of Chorin [52] has been considered as the starting point of the derivation overviewed here. Furthermore, the presence of the gravity field $\mathbf{g}$ has been taken into account the system of equations. Therefore, let us consider again the governing equations of incompressible and isothermal fluid flow problems as follows [58]:

$$\nabla \cdot \mathbf{u} = 0, \tag{3.49}$$

$$\frac{\partial \mathbf{u}}{\partial t} + (\mathbf{u} \cdot \nabla)\,\mathbf{u} = \mathbf{g} - \frac{1}{\rho}\nabla p + \nu \nabla^2 \mathbf{u}, \tag{3.50}$$

where t is the physical time, $\mathbf{u}$ is the velocity vector, $\mathbf{g}$ is the vector of the gravity field, p is the hydrodynamic pressure, ρ is density of the fluid density, and ν is the kinematic viscosity of the fluid. To derive a pressure evolution equation to formulate a two-stage pseudo-transient pressure-momentum coupling algorithm for solving incompressible fluid flow problems, a few theoretical preparatory steps need to be discussed here. Therefore, let us recall the intermediate velocity field computation Eq. (3.15) of the FS-PP method of Chorin [52] which is carried out in the first fractional-step as

$$\mathbf{u}^{*} = \mathbf{u}^{(n)} - \Delta t\,[(\mathbf{u} \cdot \nabla)\,\mathbf{u}]^{(n)} + \Delta t\,\nu \nabla^2 \mathbf{u}^{(n)} + \Delta t\,\mathbf{g}, \tag{3.51}$$

where $\mathbf{u}^{\star}$ is the non-divergence-free intermediate velocity field ($\nabla \cdot \mathbf{u}^{\star} \neq 0$) where the pressure gradient term is removed from the Navier–Stokes Eq. (3.50), and the superscript notation (n) denotes the time-level of the numerical iteration procedure. Let us recall the pressure projection step of the FS-PP method of Chorin [52] based on Eq. (3.16) assuming that the continuity Eq. (3.49) will be satisfied at time-level $(n+1)$, i.e., $\nabla \cdot \mathbf{u}^{(n+1)} = 0$, thus the elliptic-type pressure-Poission equation derived by Chorin [52] can be written as

$$\nabla^2 p^{(n+1)} = \frac{\rho}{\Delta t}\left(\nabla \cdot \mathbf{u}^{\star}\right), \tag{3.52}$$

which is projecting the intermediate velocity field (3.51) into a $\nabla \cdot \mathbf{u}^{(n+1)} = 0$ divergence-free velocity field to satisfy the continuity Eq. (3.49) iteratively, and the velocity field update is computed based on Eqs. (3.51) and (3.52) as follows:

$$\mathbf{u}^{(n+1)} = \mathbf{u}^{*} - \frac{\Delta t}{\rho}\nabla p^{(n+1)}. \tag{3.53}$$

In the FS-PP algorithm of Chorin [52] briefly described in Subsection 3.2.3, the numerical solution of Eqs. (3.51), (3.52) and (3.53) has to be repeated until the continuity Eq. (3.49) is satisfied iteratively. At this point, it is important to emphasize that there is relationship between the two-stage projection method of Harlow and Welch [59] and the three-stage FS-PP method of Chorin [52]. The pressure-Poisson Eq. (3.4) derived by Harlow and Welch [59] can be derived based on the FS-PP Eqs. (3.51) and (3.52) as well. Therefore, let us substitute Eq. (3.51) into Eq. (3.52), thus we can obtain Eq. (3.4) [57] as

$$\nabla^2 p^{(n+1)} = \frac{\rho}{\triangle t}\nabla\cdot\left\{\mathbf{u}^{(n)} - \triangle t\left[(\mathbf{u}\cdot\nabla)\,\mathbf{u}\right]^{(n)} + \triangle t\,\nu\nabla^2\mathbf{u}^{(n)}\right\} + \rho\underbrace{(\nabla\cdot\mathbf{g})}_{=0}, \tag{3.54}$$

where the divergence of the gravity field $\mathbf{g}$ vanishes, therefore

$$\nabla^2 p^{(n+1)} = \frac{\rho}{\triangle t}\nabla\cdot\left\{\mathbf{u}^{(n)} - \triangle t\left[(\mathbf{u}\cdot\nabla)\,\mathbf{u}\right]^{(n)} + \triangle t\,\nu\nabla^2\mathbf{u}^{(n)}\right\}, \tag{3.55}$$

which is identical to Eq. (3.4) derived by Harlow and Welch [59]. By the substitution of the intermediate velocity prediction Eq. (3.51) into the velocity field update Eq. (3.53) of the three-stage FS-PP method of Chorin [52], we can obtain

$$\mathbf{u}^{(n+1)} = \mathbf{u}^{(n)} - \frac{\triangle t}{\rho}\nabla p^{(n+1)} - \triangle t\left[(\mathbf{u}\cdot\nabla)\,\mathbf{u}\right]^{(n)} + \triangle t\,\nu\nabla^2\mathbf{u}^{(n)} + \triangle t\,\mathbf{g}, \tag{3.56}$$

which is identical to the velocity update Eq. (3.6) of the projection method derived by Harlow and Welch [59] (see Subsection 3.2.1). It means that both projection methods lead to the same divergence-free velocity distribution (3.56) at time-level $(n+1)$. Furthermore, the pressure-Poisson Eq. (3.55) can also be expressed as

$$\nabla^2 p^{(n+1)} = \frac{\rho}{\Delta t}\left(\nabla\cdot\mathbf{u}\right)^{(n)} - \rho\nabla\cdot\left[(\mathbf{u}\cdot\nabla)\,\mathbf{u}\right]^{(n)} + \rho\nu\nabla^2\left(\nabla\cdot\mathbf{u}\right)^{(n)}, \tag{3.57}$$

where if we assume that the continuity Eq. (3.49) is satisfied at time-level (n) as

$$D = \nabla\cdot\mathbf{u}^{(n)} = 0, \tag{3.58}$$

where D is the dilation term denoted by Harlow and Welch [59]; then, after substituting Eq. (3.58) into (3.57), the pressure-Poisson Eq. (3.57) simplifies to following form as

$$\nabla^2 p^{(n+1)} = -\rho\nabla\cdot\left[(\mathbf{u}\cdot\nabla)\,\mathbf{u}\right]^{(n)}, \tag{3.59}$$

which is identical to Eq. (3.5) (see Subsection 3.2.1). Note that the pressure-Poisson Eq. (3.59) can also be derived by taking the divergence of the Navier–Stokes Eq. (3.50), i.e., Eqs. (3.51)–(3.59) form a consistent system for solving the Navier–Stokes Eq. (3.50) iteratively. Both projection methods arrive to the same pressure-Poisson Eq. (3.55) which can be expressed in another mathematical form. Therefore, let us reformulate the right-

hand side of the pressure-Poisson Eq. (3.59) where the following identity holds as

$$-\rho\nabla\cdot[(\mathbf{u}\cdot\nabla)\mathbf{u}]^{(n)} = -\rho[(\nabla\otimes\mathbf{u})\cdot\cdot(\nabla\otimes\mathbf{u})]^{(n)} - \rho[(\mathbf{u}\cdot\nabla)(\nabla\cdot\mathbf{u})]^{(n)}, \tag{3.60}$$

where the notation '$\cdot\cdot$' denotes the double dot product of two second-rank tensors [57]. For incompressible fluid flows, due to the continuity Eq. (3.49), the total derivative of the dilation is equal to zero [57], thus we can write

$$\frac{\partial D}{\partial t} + (\mathbf{u}\cdot\nabla)D = \frac{\partial(\nabla\cdot\mathbf{u})^{(n)}}{\partial t} + (\mathbf{u}\cdot\nabla)(\nabla\cdot\mathbf{u})^{(n)} = 0, \tag{3.61}$$

which means [57] that

$$-\frac{\partial D}{\partial t} = (\mathbf{u}\cdot\nabla)D = -\frac{\partial(\nabla\cdot\mathbf{u})^{(n)}}{\partial t} = (\mathbf{u}\cdot\nabla)(\nabla\cdot\mathbf{u})^{(n)}. \tag{3.62}$$

Using the vector identity (3.60), the pressure-Poisson Eq. (3.57), obtained by Harlow and Welch (1965) [59] and Chorin (1968) [52], can also be expressed as

$$\nabla^2 p^{(n+1)} = \frac{\rho}{\Delta t}(\nabla\cdot\mathbf{u})^{(n)} - \rho\nabla\cdot[(\mathbf{u}\cdot\nabla)\mathbf{u}]^{(n)} + \rho\nu\nabla^2(\nabla\cdot\mathbf{u})^{(n)} =$$

$$= \frac{\rho}{\Delta t}(\nabla\cdot\mathbf{u})^{(n)} - \rho[(\nabla\otimes\mathbf{u})\cdot\cdot(\nabla\otimes\mathbf{u})]^{(n)} - \rho[(\mathbf{u}\cdot\nabla)(\nabla\cdot\mathbf{u})]^{(n)} + \rho\nu\nabla^2(\nabla\cdot\mathbf{u})^{(n)}, \tag{3.63}$$

where using Eq. (3.62), we can write the pressure-Poisson Eqs. (3.57) and (3.63) as

$$\nabla^2 p^{(n+1)} = \frac{\rho}{\Delta t}D^{(n)} - \rho[(\nabla\otimes\mathbf{u})\cdot\cdot(\nabla\otimes\mathbf{u})]^{(n)} + \rho\frac{\partial D^{(n)}}{\partial t} + \rho\nu\nabla^2 D^{(n)}. \tag{3.64}$$

Using the vector identity (3.60) again, the pressure-Poisson Eq. (3.59) can be written as

$$\nabla^2 p^{(n+1)} = -\rho\nabla\cdot[(\mathbf{u}\cdot\nabla)\mathbf{u}]^{(n)} = -\rho[(\nabla\otimes\mathbf{u})\cdot\cdot(\nabla\otimes\mathbf{u})]^{(n)} - \rho[(\mathbf{u}\cdot\nabla)(\nabla\cdot\mathbf{u})]^{(n)}, \tag{3.65}$$

where using Eq. (3.62), we can write the pressure-Poisson Eqs. (3.59) and (3.65) as

$$\nabla^2 p^{(n+1)} = -\rho[(\nabla\otimes\mathbf{u})\cdot\cdot(\nabla\otimes\mathbf{u})]^{(n)} + \rho\frac{\partial D^{(n)}}{\partial t}. \tag{3.66}$$

The dilation term $D^{(n)}$ and its time derivative at time-level (n) are kept by Harlow and Welch [59] in the pressure-Poisson Eqs. (3.64) and (3.66) to avoid the accumulation of numerical errors in the iteration process [59]. Note that the dilation term $D^{(n)}$ is very small numerical value at each time-level (n), theoretically equal to zero due to the continuity Eq. (3.49) [108]–[110]. Although, it is still important to keep the dilation term $D^{(n)}$ in the numerical procedure to remain consistent with the pressure projection method of Chorin [52] which is relying on the Helmholtz-Hodge decomposition [68]–[72]. Using the pressure-Poisson Eq. (3.64) and the velocity update Eq. (3.56), the two-stage

projection method of Harlow and Welch [59] can be summarised as follows:

$$\nabla^2 p^{(n+1)} = \frac{\rho}{\Delta t} D^{(n)} - \rho \left[(\nabla \otimes \mathbf{u}) \cdot \cdot (\nabla \otimes \mathbf{u}) \right]^{(n)} + \rho \frac{\partial D^{(n)}}{\partial t} + \rho \nu \nabla^2 D^{(n)}, \tag{3.67}$$

$$\mathbf{u}^{(n+1)} = \mathbf{u}^{(n)} - \frac{\triangle t}{\rho} \nabla p^{(n+1)} - \triangle t \left[(\mathbf{u} \cdot \nabla) \mathbf{u} \right]^{(n)} + \triangle t \, \nu \nabla^2 \mathbf{u}^{(n)} + \triangle t \, \mathbf{g}, \tag{3.68}$$

where the pressure-Poisson Eq. (3.67) is identical to the pressure-Poisson Eqs. (3.52) and (3.55) obtained by Harlow and Welch [59] and Chorin [52]. Therefore, the two-stage pressure projection method of Harlow and Welch [59] defined by Eqs. (3.67) and (3.68) is identical to the three-stage FS-PP projection method of Chorin [52]. The only difference between them is how Harlow and Welch [59] and Chorin [52] discretised these equations, although as solution frameworks to the Navier–Stokes Eq. (3.50), they are identical. Both pressure projection methods lead to an approximate divergence-free (3.49) iterative solution of the incompressible Navier–Stokes Eq. (3.50) [57]. The validity of the pressure projection method of Harlow and Welch [59] and the three-stage FS-PP method of Chorin [52] has been proven by thousands of authors in the literature over the past 60 years. It was important to review them, because the pressure-Poisson Eq. (3.66) and the velocity update Eq. (3.68) formed the theoretical basis for the development of a two-stage pseudo-transient pressure-momentum coupling algorithm by introducing a pressure evolution equation instead of solving the pressure-Poisson Eq. (3.55). Furthermore, these pressure projection methods are treated separately by others in the literature.

To introduce a pressure evolution equation in the context of a two-stage pseudo-transient pressure-momentum coupling solution method as a second step of the derivation overviewed here, let us consider the pressure-Poisson Eq. (3.59) which can be derived by taking the divergence of the incompressible Navier–Stokes Eq. (3.55) as follows:

$$-\nabla^2 p^{(n+1)} = \rho \nabla \cdot \left[(\mathbf{u} \cdot \nabla) \mathbf{u} \right]^{(n)}, \tag{3.69}$$

and by multiplying Eq. (3.69) by (-1) and using Eqs. (3.60) and (3.62), the right-hand side of the pressure-Poisson Eq. (3.69) can be reformulated as

$$-\nabla^2 p^{(n+1)} = \rho \left[(\nabla \otimes \mathbf{u}) \cdot \cdot (\nabla \otimes \mathbf{u}) \right]^{(n)} + \rho \left[(\mathbf{u} \cdot \nabla) (\nabla \cdot \mathbf{u}) \right]^{(n)}, \tag{3.70}$$

where the viscous contribution of the dilation term $D^{(n)}$ in Eq. (3.57) vanishes, because it has been assumed that the initial conditions of the velocity field satisfy the divergence-free continuity Eq. (3.49), i.e., $\nabla \cdot \mathbf{u}^{(0)} = 0$ at $t = 0$. Using Eq. (3.62), we can also write

$$-\nabla^2 p^{(n+1)} = \rho \left[(\nabla \otimes \mathbf{u}) \cdot \cdot (\nabla \otimes \mathbf{u}) \right]^{(n)} + \rho (\mathbf{u} \cdot \nabla) D^{(n)}, \tag{3.71}$$

where the dilation term $D^{(n)}$ arises from taking the divergence of the non-linear convective term on the right-hand side of the pressure-Poisson Eq. (3.69). According to Fletcher [111], a second-order elliptic-type Poisson equation can be transformed into a parabolic equation using a pseudo-transient approach which are often used in the context of the

streamfunction-vorticity formulation [111, p. 370]. Therefore, the pressure-Poisson Eq. (3.71) can be transformed into a parabolic pseudo-transient transport equation by introducing a pseudo-transient pressure term on the left-hand side of Eq. (3.71) as follows:

$$\frac{1}{\beta}\frac{\partial p}{\partial \tau} - \nabla^2 p^{(n)} = \rho\left[(\nabla \otimes \mathbf{u}) \cdot\cdot (\nabla \otimes \mathbf{u})\right]^{(n)} + \rho\,(\mathbf{u}\cdot\nabla)\,D^{(n)}, \tag{3.72}$$

where β is a convergence parameter, τ is the pseudo-time, and the second-order Laplacian pressure term $\nabla^2 p^{(n)}$ has to be taken at pseudo-time level (n) in the pseudo-time marching numerical procedure [57]. After re-arranging Eq. (3.72), a pseudo-transient pressure evolution equation can be introduced and obtained [57] as follows:

$$\boxed{\frac{1}{\beta}\frac{\partial p}{\partial \tau} = \nabla^2 p^{(n)} + \rho\left[(\nabla \otimes \mathbf{u}) \cdot\cdot (\nabla \otimes \mathbf{u})\right]^{(n)} + \rho\,(\mathbf{u}\cdot\nabla)\,D^{(n)},} \tag{3.73}$$

which can also be written in a semi-discrete form for numerical computations [57] as

$$\frac{1}{\beta}\frac{p^{(n+1)} - p^{(n)}}{\Delta\tau} = \nabla^2 p^{(n)} + \rho\left[(\nabla \otimes \mathbf{u}) \cdot\cdot (\nabla \otimes \mathbf{u})\right]^{(n)} + \rho\,(\mathbf{u}\cdot\nabla)\,D^{(n)}. \tag{3.74}$$

Using the semi-discrete form of the pseudo-transient pressure evolution Eq. (3.74) and coupling it with the velocity field update Eq. (3.68) of Harlow and Welch [59] and Chorin [52], then a two-stage pseudo-transient pressure-momentum coupling algorithm can be formulated for solving the stationary Navier–Stokes equations [57] as follows:

$$\boxed{p^{(n+1)} = p^{(n)} + \beta\Delta\tau\left\{\nabla^2 p^{(n)} + \rho\left[(\nabla \otimes \mathbf{u}) \cdot\cdot (\nabla \otimes \mathbf{u})\right]^{(n)} + \rho\,(\mathbf{u}\cdot\nabla)\,D^{(n)}\right\},} \tag{3.75}$$

$$\boxed{\mathbf{u}^{(n+1)} = \mathbf{u}^{(n)} - \frac{\triangle\tau}{\rho}\nabla p^{(n+1)} - \triangle\tau\left[(\mathbf{u}\cdot\nabla)\,\mathbf{u}\right]^{(n)} + \triangle\tau\,\nu\nabla^2\mathbf{u}^{(n)} + \triangle\tau\,\mathbf{g},} \tag{3.76}$$

where $\triangle\tau$ is the pseudo-time step, and the superscript notations $(n+1)$ and (n) denote pseudo-time levels in the context of pseudo-transient formulations, i.e., the real-time step $\triangle t$ was replaced by the pseudo-time step $\triangle\tau$ in the velocity field update Eq. (3.68). The pseudo-transient system of equations (3.75) and (3.76) forms a closed system for the primitive variables u, v, w and p which can be employed for solving incompressible, stationary fluid flow problems. Instead of solving the pressure-Poisson Eq. (3.55), a pseudo-transient pressure evolution Eq. (3.75) has to be solved coupled with the local momentum Eq. (3.76) where the iterative solution procedure has to be repeated until each pseudo-time derivative vanishes in Eqs. (3.75) and (3.76), i.e., the stationary solution is achieved iteratively [57]. The two-stage pseudo-transient pressure-momentum coupling algorithm using the scalar discretised forms of the transport partial differential Eqs. (3.75) and (3.76) was implemented in an in-house C code developed by Könözsy (2017) [57]. Therefore, the results of a simulation will be reviewed in the next Subsection 3.4.3.

3.4.3 Laminar flow in a horizontal microfluidic channel

For solving two-dimensional stationary fluid flow problems, the scalar form of the governing Eqs. (3.75) and (3.76) of the two-stage pseudo-transient pressure-velocity coupling algorithm for the primitive variables p, u and v can be written [57] as follows:

$$p^{(n+1)} = p^{(n)} + \beta\Delta\tau\left(\frac{\partial^2 p}{\partial x^2} + \frac{\partial^2 p}{\partial y^2}\right)^{(n)} + \beta\Delta\tau\rho\left[\left(\frac{\partial u}{\partial x}\right)^2 + \left(\frac{\partial v}{\partial y}\right)^2 + 2\frac{\partial v}{\partial x}\frac{\partial u}{\partial y}\right]^{(n)} + \\ + \beta\Delta\tau\rho\left[u\frac{\partial}{\partial x}\left(\frac{\partial u}{\partial x} + \frac{\partial v}{\partial y}\right) + v\frac{\partial}{\partial y}\left(\frac{\partial u}{\partial x} + \frac{\partial v}{\partial y}\right)\right]^{(n)}, \tag{3.77}$$

$$u^{(n+1)} = u^{(n)} - \frac{\Delta\tau}{\rho}\left(\frac{\partial p}{\partial x}\right)^{(n+1)} - \Delta\tau\left(u\frac{\partial u}{\partial x} + v\frac{\partial u}{\partial y}\right)^{(n)} + \Delta\tau\nu\left(\frac{\partial^2 u}{\partial x^2} + \frac{\partial^2 u}{\partial y^2}\right)^{(n)}, \tag{3.78}$$

$$v^{(n+1)} = v^{(n)} - \frac{\Delta\tau}{\rho}\left(\frac{\partial p}{\partial y}\right)^{(n+1)} - \Delta\tau\left(u\frac{\partial v}{\partial x} + v\frac{\partial v}{\partial y}\right)^{(n)} + \Delta\tau\nu\left(\frac{\partial^2 v}{\partial x^2} + \frac{\partial^2 v}{\partial y^2}\right)^{(n)}, \tag{3.79}$$

where u and v are the scalar components of the velocity vector $\mathbf{u}$. The Finite Difference Method (FDM) was used to discretise the scalar system of Eqs. (3.77)–(3.79) with a first-order accurate pseudo-temporal scheme with the pseudo-time step of $\triangle\tau = 4.9 \cdot 10^{-5}$; and the numerical value of the convergence parameter β was equal to 1.0 [57]. The second-order spatial derivatives of the pressure on the right-hand side of the pseudo-transient pressure evolution Eq. (3.77) and the viscous terms on the right-hand sides of the scalar momentum Eqs. (3.78)–(3.79) were approximated with second-order central schemes. The third terms on the right-hand sides of the scalar Navier–Stokes Eqs. (3.78)–(3.79), i.e., the non-linear convective terms were discretised by an upwind scheme proposed by Torrance and Rockett (1969) [112]. The first-order derivatives in the third and fourth terms on the right-hand side of the pseudo-transient pressure evolution Eq. (3.77), arise from taking the divergence of the convective terms in Eq. (3.69), were approximated with second-order accurate central schemes in each spatial direction. For the shake of simplicity, the explicit FD numerical solution of the system of Eqs. (3.77)–(3.79) was implemented in an in-house C code without using any parallel computing; and all simulations were performed on a Dual-Core E5300 2.60 GHz computer on a single CPU.

To investigate the accuracy and numerical convergence properties of the two-stage pseudo-transient algorithm in comparison with the FS-PP method of Chorin [52], a 2D incompressible stationary laminar flow in a horizontal microfluidic channel has been considered at $Re = 10$ as a benchmark problem. For example, low Re number flows occur in microfluidic devices within a very short physical time [58]. The length and height of the microfluidic channel were $2\mu m$ and $1\mu m$, respectively. The computational mesh density was taken similarly to the benchmark test case discussed in Subsection 3.3.2. Therefore, the fine mesh consisted of 7200 (180×40) computational cells [57]. In terms of boundary conditions, the Dirichlet-type no-slip boundary conditions were specified along the

bottom and top walls. A uniform velocity profile was imposed at the inlet section of the microfluidic channel with the magnitude of the average velocity computed based on the *Re* number. At the outlet section, a homogeneous Neumann-type ($\partial p/\partial n = 0$) outflow boundary conditions were specified for the velocity components u and v. In terms of the pressure field, homogeneous Neumann-type boundary conditions ($\partial p/\partial n = 0$) were imposed at the inlet section of the microfluidic channel and along the walls, except at the outlet section, where a Dirichlet-type zero boundary condition was specified for the pressure. The same velocity and pressure boundary conditions were prescribed for both the FS-PP method [52] and the two-stage pseudo-transient algorithm [57]. The residual histories of the FS-PP method [52] and the two-stage pseudo-transient algorithm with the pressure evolution Eq. (3.77) [57] in the L_2-norm are shown in Figures 3.7 and 3.8.

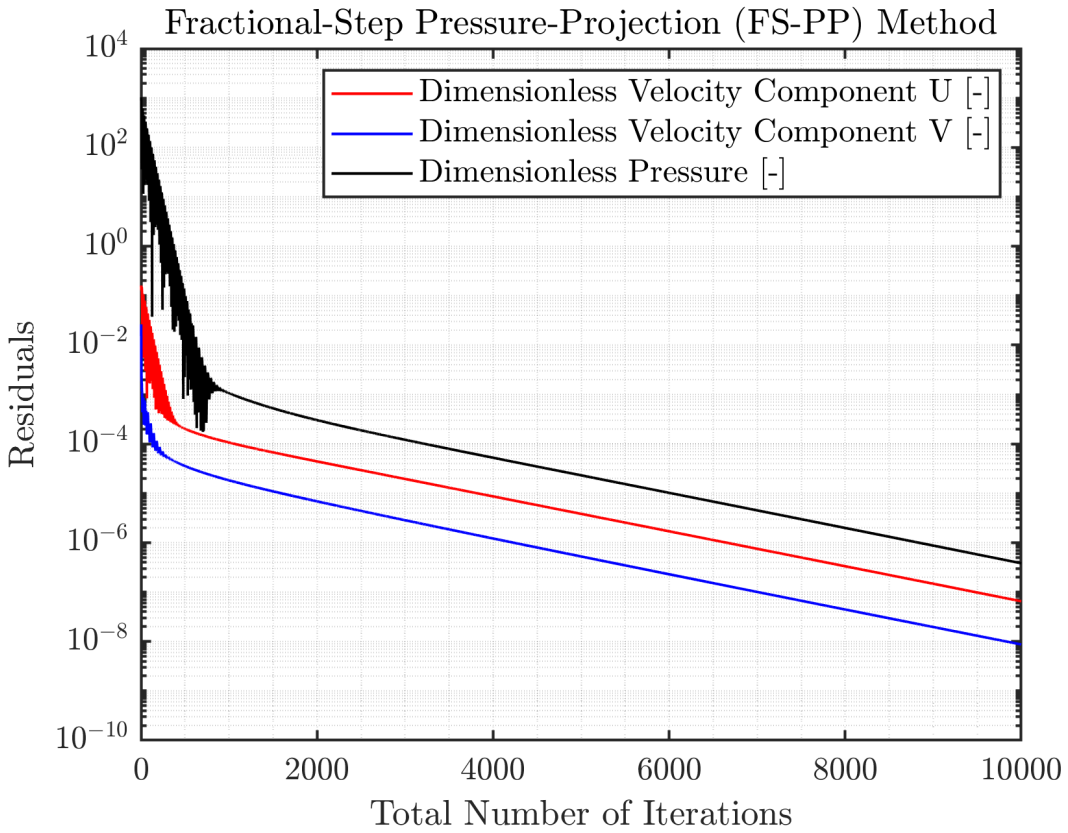

Figure 3.7: Residual histories of the FS-PP method for the dimensionless velocity components U and V, and pressure P in the L_2-norm [57, p. 7][9]

[9]Figure 3.7 presented here in Subsection 3.4.3 was first published in the work entitled as "Pseudo-Transient Pressure-Momentum Coupling Method for Low-Speed Incompressible Flows", Author: László Könözsy, *In: MultiScience - XXXI. microCAD International Multidisciplinary Scientific Conference, University of Miskolc, Hungary*, CD-ROM, ISBN 978-963-358-132-2, 20-21 April 2017, published by the University of Miskolc.

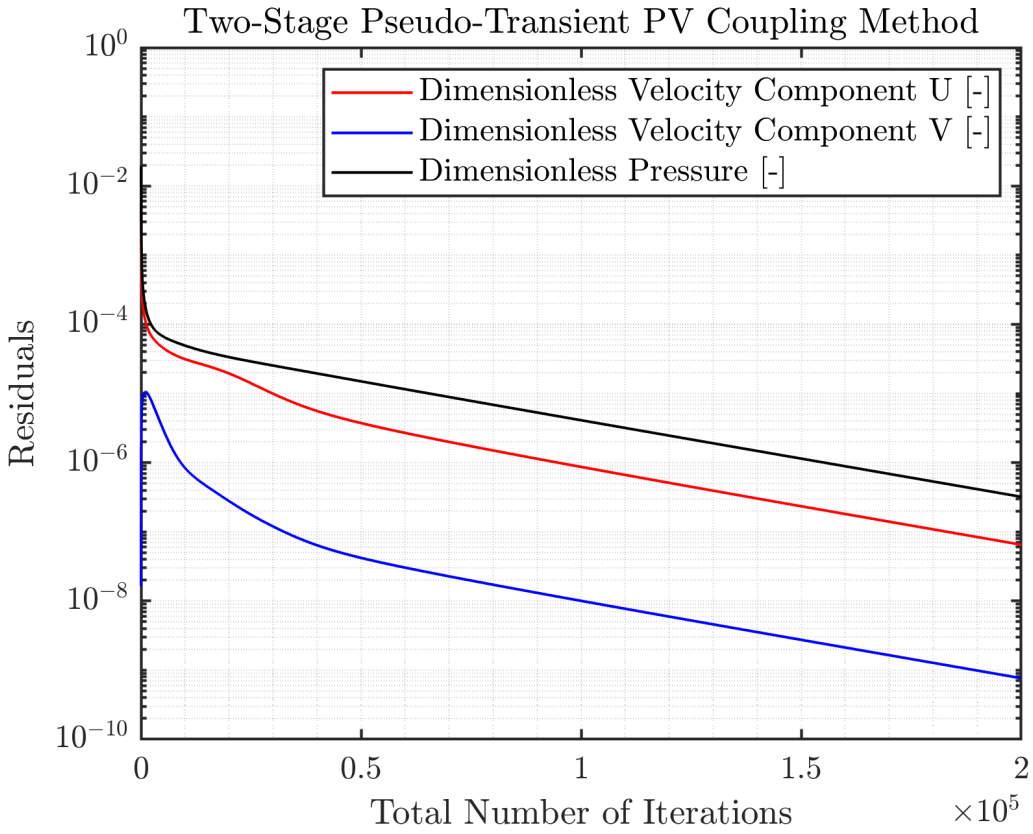

Figure 3.8: Residual histories of the two-stage pseudo-transient algorithm for the dimensionless velocity components U and V, and pressure P in the L_2-norm [57, p. 7][10]

It can be seen in Figure 3.7 that the pressure field solution with the FS-PP method [52] was oscillatory up to ~1000 iterations; while the pressure field solution with the two-stage pseudo-transient algorithm was continuously converging to a small threshold value of 10^{-6} [57] which is shown in Figure 3.8. The FS-PP method [52] and the two-stage pseudo-transient pressure projection algorithm [57] were required to perform 10 000 and 200 000 iterations with the actual computational times of 25 and 36 minutes, respectively, until the fluid flow became fully-developed at the outlet section of the microfluidic channel. The numerically predicted fully-developed dimensionless velocity profiles with the FS-PP method [52] and the two-stage pseudo-transient algorithm [57] in comparison with a simplified analytical solution at the outlet section at $Re = 10$ are shown in Figure 3.9.

[10]Figure 3.8 presented here in Subsection 3.4.3 was first published in the work entitled as "Pseudo-Transient Pressure-Momentum Coupling Method for Low-Speed Incompressible Flows", Author: László Könözsy, *In: MultiScience - XXXI. microCAD International Multidisciplinary Scientific Conference, University of Miskolc, Hungary*, CD-ROM, ISBN 978-963-358-132-2, 20-21 April 2017, published by the University of Miskolc.

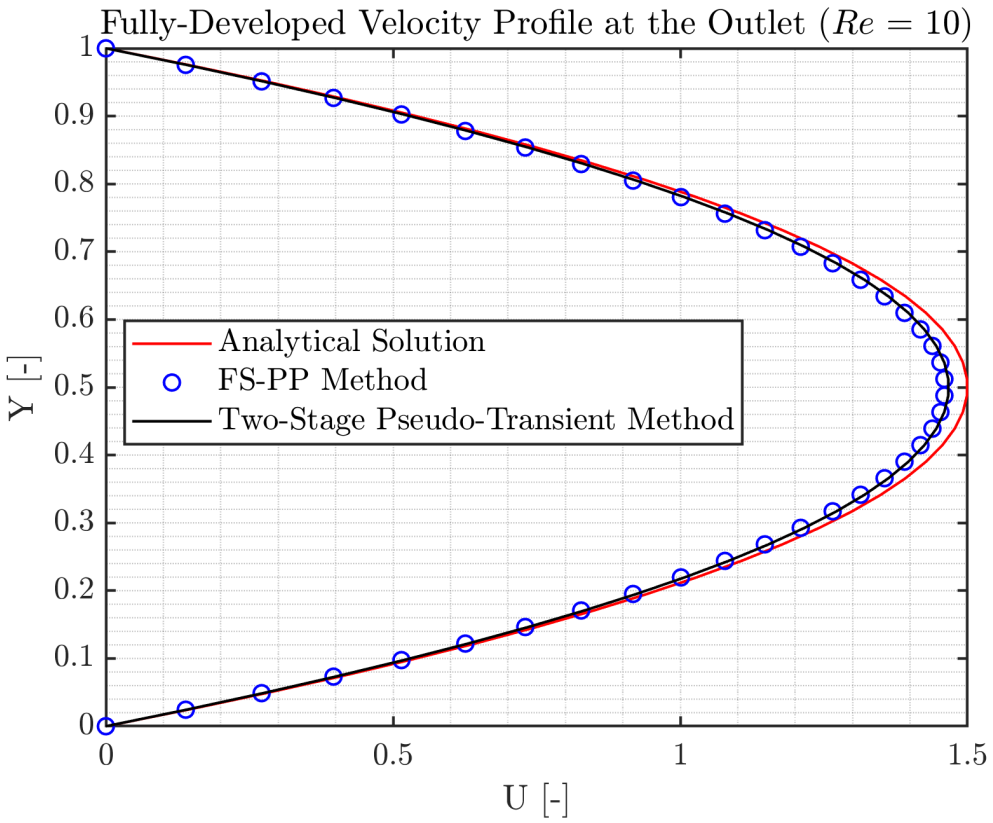

Figure 3.9: Comparison of dimensionless fully-developed velocity profiles non-dimensionalised by the average velocity at the outlet section at $Re = 10$ [57, p. 8][11]

The accurate numerical value of the maximum velocity was slightly under-predicted by both methods in comparison with the analytical solution at the outlet section. For the microfluidic application reviewed here, the maximum relative error of both methods was 2% compared to the analytical solution [57]. The accuracy and efficiency of the numerical solution for both methods could be further improved with the use of a higher than first-order, e.g., Runge–Kutta pseudo-time marching scheme along with an adaptive pseudo-time stepping strategy. In the context of pseudo-transient and FD methods, a higher-order pressure outlet boundary condition treatment is recommended as proposed in [61]. For unsteady flows, a dual-time stepping procedure has to be employed [57]. For this benchmark problem, the computational results suggest that the two-stage pseudo-transient algorithm could remove the oscillatory pressure field behaviour from the numerical solution in comparison with the FS-PP [52] pressure-Poisson solver-based projection method.

[11] Figure 3.9 presented here in Subsection 3.4.3 was first published in the work entitled as "Pseudo-Transient Pressure-Momentum Coupling Method for Low-Speed Incompressible Flows", Author: László Könözsy, *In: MultiScience - XXXI. microCAD International Multidisciplinary Scientific Conference, University of Miskolc, Hungary*, CD-ROM, ISBN 978-963-358-132-2, 20-21 April 2017, published by the University of Miskolc.

3.5 Summary of the contribution to the knowledge

The author of this booklet has started to conduct theoretical research on the development of pressure-velocity (PV) coupling or PV closure models for solving the incompressible Navier–Stokes Eq. (3.2) in the context of pseudo-transient methods since 2008. Relying on the theoretical development and numerical simulations overviewed in Chapter 3 which were carried out after the author received his PhD degree (2004) from the University of Miskolc, Hungary, a few conclusions can be summarised in thesis points as novel research advances from the past 12 years and contribution to the knowledge as follows:

1. The unification of the Artificial Compressibility (AC) and Fractional-Step Pressure-Projection (FS-PP) methods of Chorin [51], [52] led to the development of a unified FSAC-PP method for solving incompressible fluid flow problems in the context of pseudo-transient methods [54, pp. 1142-1148], [T6, pp. 1142-1148]. The stationary variant of the FSAC-PP method related to the characteristics-based (CB) Godunov-type computation of the non-linear convective terms was overviewed in Section 3.3.

    1.1. The FSAC-PP method has been implemented in an in-house FORTRAN 90/95 code. The verification of the code and the validation of the FSAC-PP Navier–Stokes solver have been carried out on different benchmark problems in comparison with a simplified analytical solution, numerical data of Ghia et al. [98] and experimental data of Prasad and Koseff [99] ranging from very low to high Re numbers [54, pp. 1148-1149], [T6, pp. 1148-1149].

    1.2. It has been found that the FSAC-PP method was more accurate and efficient for numerically predicting very low Re number flows ($Re \ll 1$) than the AC [51] and FS-PP [52] methods [54, pp. 1177-1178], [T6, pp. 1177-1178].

    1.3. It has been found that the use of at least a third-order interpolation scheme is required for computing the non-linear convective terms with the CB scheme (3.38) to accurately predict the physically correct behaviour of the fluid flow at low Re number flows [54, p. 1153], [T6, p. 1153].

    1.4. It has been found that the FSAC-PP method was capable of capturing the physically correct streamline patterns of primary and secondary vortices as well as predicting accurately the velocity profiles along the horizontal and vertical centre-lines of a unit square cavity when only a first-order interpolation scheme was employed for computing the convective terms with the CB scheme (3.38) at $Re = 1000$ compared to the numerical data of Ghia et al. [98], see Figures 3.2, 3.3(a) and 3.3(b) [54, pp. 1160-1172], [T6, pp. 1160-1172].

1.5. It has been found that the use of the FSAC-PP method led to more accurate simulation results when lower-order interpolation schemes were employed than using the AC [51] and FS-PP [52] methods [54, p. 1172], [T6, p. 1172]. It could reduce the computational time and maintain the expected accuracy.

1.6. It has been found that the FSAC-PP method can be employed for simulating high Re number turbulent flows in the framework of the Implicit Large Eddy Simulation (ILES) technique—which is an "Under-Resolved Direct Numerical Simulation (DNS)" approach [100, p. 475], [T10, p. 475]—to predict the distribution of Reynolds stresses in a three-dimensional lid-driven cavity compared to the experimental data of Prasad and Koseff [99] at $Re = 10\,000$, see Figures 3.4(a) and 3.4(b) [54], [T6]. For simulating unsteady high Re number turbulent flows with the FSAC-PP method, a dual-time stepping procedure has to be employed [54, pp. 1172-1177], [T6, pp. 1172-1177].

1.7. It has been found that the use of the FSAC-PP method led to more accurate simulation results than using the AC method [51] when a bifurcating laminar flow was investigated in a sudden expansion channel at $Re = 80$ by using different Godunov-type discretisation schemes for computing the non-linear convective terms in comparison with the experimental data of Fearn et al. [103], see Figures 3.5(c) and 3.5(d) [55, pp. 10-11], [T7, pp. 10-11].

1.8. It can be stated that the FSAC-PP method required the least computational time compared to the AC method [51] when a bifurcating laminar flow was investigated in a sudden expansion channel at different Re numbers ranging from 15 to 100, see Figure 3.6 [55, p. 17], [T7, p. 17].

1.9. It can be stated that not only the choice of the order of the interpolation scheme employed in the discretisation has impact on the accuracy of the numerical solution procedure, because the choice of the pressure-velocity (PV) coupling method matters as well [55, p. 11], [T7, p. 11], [56], [T8].

1.10. It can be stated that high-resolution Godunov-type schemes for computing the non-linear convective terms [86], [96] can be employed not only for simulating incompressible fluid flows with high accuracy, but also for nearly hypersonic, unsteady, viscous, compressible, chemically reacting turbulent magnetogasdynamic flows, e.g., behind cuboid geometries [100], [T10].

2. A new pseudo-transient pressure evolution Eq. (3.73) has been derived, proposed and implemented by the author of this booklet as follows (2017) [57, p. 5], [T9, p. 5]:

$$\boxed{\frac{1}{\beta}\frac{\partial p}{\partial \tau} = \nabla^2 p^{(n)} + \rho\left[(\nabla \otimes \mathbf{u}) \cdot\cdot (\nabla \otimes \mathbf{u})\right]^{(n)} + \rho\,(\mathbf{u}\cdot\nabla)\,D^{(n)}.} \tag{3.80}$$

3. By using the pseudo-transient pressure evolution Eq. (3.80), a two-stage pseudo-transient pressure-velocity coupling algorithm has been developed for solving the incompressible stationary Navier–Stokes equations which can be formulated in a semi-discrete form as follows (2017) [57, pp. 5-6], [T9, pp. 5-6]:

$$\boxed{p^{(n+1)} = p^{(n)} + \beta\Delta\tau\left\{\nabla^2 p^{(n)} + \rho\left[(\nabla\otimes\mathbf{u})\cdot\cdot(\nabla\otimes\mathbf{u})\right]^{(n)} + \rho(\mathbf{u}\cdot\nabla)D^{(n)}\right\},} \tag{3.81}$$

$$\boxed{\mathbf{u}^{(n+1)} = \mathbf{u}^{(n)} - \frac{\triangle\tau}{\rho}\nabla p^{(n+1)} - \triangle\tau\left[(\mathbf{u}\cdot\nabla)\mathbf{u}\right]^{(n)} + \triangle\tau\nu\nabla^2\mathbf{u}^{(n)} + \triangle\tau\mathbf{g}.} \tag{3.82}$$

   3.1. The two-stage pseudo-transient pressure-velocity coupling (3.81)–(3.82) algorithm [57], [T9] is a pseudo-transient pressure projection method which can be derived either from projection method of Harlow and Welch [59] or from the FS-PP method of Chorin [52] [57, p. 2], [T9, p. 2].

   3.2. It has been derived and found that the two-stage pressure projection method (3.67)–(3.68) of Harlow and Welch [59] is identical to the three-stage FS-PP method (3.51)–(3.53) of Chorin [52]. The only difference between them is how their equations are discretised, although as solution frameworks to the Navier–Stokes Eq. (3.50), they are identical [57, p. 2-4], [T9, p. 2-4].

   3.3. An in-house C code has been developed for solving numerically the governing Eqs. (3.81)–(3.82) of the two-stage pseudo-transient pressure-velocity coupling algorithm by using the Finite Difference Method (FDM). A first-order accurate forward scheme has been employed for the discretisation of the pseudo-time derivative. An upwind scheme proposed by Torrance and Rockett [112] has been used for computing the non-linear convective terms, and the rest of the spatial discretisation was carried out by employing second-order accurate central schemes [57, p. 6], [T9, p. 6].

   3.4. The verification of the in-house C code and the validation the two-stage pseudo-transient pressure-velocity coupling algorithm (3.81)–(3.82) were carried out on a benchmark problem for simulating a laminar flow in a two-dimensional horizontal microfluidic channel at $Re = 10$. The maximum relative error of the numerical solution was 2% in comparison with a simplified analytical solution at the outlet section of the channel [57, p. 8], [T9, p. 8].

   3.5. It has been found that the two-stage pseudo-transient approach (3.81)–(3.82) could replace the solution of a pressure-Poisson Eq. (3.55) for incompressible flows and overcome the oscillatory pressure field solution in a low Re number flow when the primitive variables u, v, p have a collocated arrangement on the computational mesh points (see Figure 3.8) [57, p. 7], [T9, p. 7].

3.6 Új tudományos eredmények összefoglalása

E habilitációs füzet szerzője 2008 óta foglalkozik olyan elméleti kutatásokkal, amelyek nyomás-sebesség (PV) összekapcsolási vagy PV zárási modellek kifejlesztésére irányulnak, az összenyomhatatlan folyadékáramlásra érvényes Navier–Stokes egyenletek (3.2) megoldására, a pszeudo-tranziens módszerek kontextusában. A 3. Fejezetben áttekintett elméleti fejlesztések és szimulációk alapján, amelyeket a szerző a PhD fokozatának (2004) a Miskolci Egyetemen, Magyarországon történő megszerzése után végzett, néhány konklúzió mint az elmúlt 12 év új kutatási előrelépései és a tudományos ismereteinkhez való hozzájárulás az alábbi tézispontokban foglalható össze:

1. A Chorin-féle Mesterséges Összenyomhatóság (AC) és Időszeleteléses Nyomás-Projekciós (FS-PP) módszereinek [51], [52] egyesítése egy egységes FSAC-PP módszer kifejlesztéséhez vezetett az összenyomhatatlan folyékony közegek áramlására vonatkozó problémák megoldására a pszeudo-tranziens módszerek kontextusában [54, pp. 1142-1148], [T6, pp. 1142-1148]. Az FSAC-PP módszer stacionárius változatát a nem-lineáris konvektív tagok karakterisztikák módszerén alapuló (CB) Godunov-típusú számításával összefüggésben a 3.3 Szakaszban tekintettük át.

   1.1. Az FSAC-PP módszert implementáltam egy saját készítésű FORTRAN 90/95 nyelvű kódba. A számítógépes kód verifikációját és az FSAC-PP Navier-Stokes megoldó módszer validálását különböző mintafeladatok megoldásán keresztül végeztem el összehasonlítva egy egyszerűsített analitikus megoldással, Ghia és szerzőtársai [98] számítási adataival, valamint Prasad és Koseff [99] kísérletekből származó adataival a nagyon kis Re számoktól a nagy Re számokig kiterjedően [54, pp. 1148-1149], [T6, pp. 1148-1149].

   1.2. Megállapítottam, hogy az FSAC-PP módszer pontosabb és hatékonyabb a nagyon kis Re számú áramlások ($Re \ll 1$) numerikus becslésében, mint az AC [51] és FS-PP [52] módszerek [54, pp. 1177-1178], [T6, pp. 1177-1178].

   1.3. Megállapítottam, hogy legalább harmadrendű interpolációs séma alkalmazása szükséges a nem-lineáris konvektív tagok CB sémával (3.38) történő számításához, hogy pontosan becsüljük a folyadékáramlás fizikailag helyes viselkedését kis Re számú áramlások esetén [54, p. 1153], [T6, p. 1153].

   1.4. Megállapítottam, hogy az FSAC-PP módszer alkalmas a primer és szekunder örvények fizikailag helyes áramvonalképeinek és az egységnégyzet üreg vízszintes és függőleges középvonalai mentén a sebességprofilok pontos becslésére, amikor a konvektív tagok a CB sémával (3.38) történő kiszámításához csak elsőrendű interpolációs sémát alkalmaztunk $Re = 1000$ esetén összehasonlítva Ghia és szerzőtársai [98] által kapott számítási eredményekkel, lásd 3.2, 3.3(a) és 3.3(b) ábrákat [54, pp. 1160-1172], [T6, pp. 1160-1172].

1.5. Megállapítottam, hogy az FSAC-PP módszer pontosabb szimulációs eredményeket szolgáltatott alacsonyabb rendű interpolációs sémák alkalmazása esetén, mint az AC [51] és FS-PP [52] módszerek [54, p. 1172], [T6, p. 1172]. Ez csökkentheti a számítási időt megőrizve az elvárt pontosságot.

1.6. Megállapítottam, hogy az FSAC-PP módszer alkalmazható nagy *Re* számú turbulens áramlások szimulációjára az Implicit Nagy Örvény Szimulációs (ILES) technika felhasználásával—amely egy „Nem finom-felbontású Direkt Numerikus Szimulációs (DNS)" megközelítés [100, p. 475], [T10, p. 475]—, hogy becsüljük a Reynolds-féle feszültségeloszlásokat egy háromdimenziós mozgó fedéllel ellátott üregben összehasonlítva Prasad és Koseff [99] kísérleti adataival $Re = 10000$ esetén, lásd 3.4(a) és 3.4(b) ábrákat [54], [T6]. Instacionárius nagy *Re* számú turbulens áramlások szimulációjára a duális-időlépés eljárást kell alkalmazni [54, pp. 1172-1177], [T6, pp. 1172-1177].

1.7. Megállapítottam, hogy az FSAC-PP módszer pontosabb szimulációs eredmények adott, mint az AC módszer [51] egy bifurkáló lamináris áramlás vizsgálatakor egy hirtelen keresztmetszetváltozású csatornában $Re = 80$ esetén, a nem-lineáris konvektív tagok számítására használt különböző Godunov-típusú diszkretizációs sémákra, összevetve Fearn és szerzőtársai [103] kísérleti adataival, lásd 3.5(c) és 3.5(d) ábrákat [55, pp. 10-11], [T7, pp. 10-11].

1.8. Megállapítható, hogy az FSAC-PP módszer igényelte a legkevesebb számítási időt az AC módszerrel [51] összehasonlítva egy bifurkáló lamináris áramlás vizsgálatakor hirtelen keresztmetszetváltozású csatornában, 15 és 100 közötti különböző *Re* számok esetén, lásd 3.6 ábrát [55, p. 17], [T7, p. 17].

1.9. Megállapítható, hogy nemcsak a diszkretizáció során alkalmazott interpolációs séma rendjének megválasztása befolyásolja a numerikus megoldási eljárás pontosságát, hanem a nyomás-sebesség (PV) összekapcsolási módszer megválasztása is [55, p. 11], [T7, p. 11], [56], [T8].

1.10. Megállapítható, hogy a nem-lineáris konvektív tagok számítására használt nagy-felbontású Godunov-típusú sémák [86], [96] nemcsak az összenyomhatatlan folyadékáramlások nagy pontosságú szimulációjára alkalmazhatóak, hanem közel hiperszonikus, időfüggő, súrlódásos, összenyomható, kémiailag reagáló turbulens magnetogázdinamikai áramlások esetén is, például kocka alakú geometriák mögött [100], [T10].

2. E füzet szerzője levezetett, javasolt és implementált egy új pszeudo-tranziens nyomástér kialakulására érvényes egyenletet (3.73) az alábbi szerint (2017) [57, p. 5], [T9, p. 5]:

$$\boxed{\frac{1}{\beta}\frac{\partial p}{\partial \tau} = \nabla^2 p^{(n)} + \rho\left[(\nabla \otimes \mathbf{u}) \cdot\cdot (\nabla \otimes \mathbf{u})\right]^{(n)} + \rho\,(\mathbf{u}\cdot\nabla)\,D^{(n)}.} \tag{3.83}$$

3. Kifejlesztettem a nyomástér kialakulására érvényes új pszeudo-tranziens egyenlet (3.83) felhasználásával egy két-lépcsős pszeudo-tranziens nyomás-sebesség összekapcsolási algoritmust az összenyomhatatlan folyadékok stacionárius áramlására vonatkozó Navier–Stokes egyenletek megoldására, amely kifejezhető szemi-diszkrét alakban a következők szerint (2017) [57, pp. 5-6], [T9, pp. 5-6]:

$$\boxed{p^{(n+1)} = p^{(n)} + \beta\Delta\tau\left\{\nabla^2 p^{(n)} + \rho\left[(\nabla\otimes\mathbf{u})\cdot\cdot(\nabla\otimes\mathbf{u})\right]^{(n)} + \rho\left(\mathbf{u}\cdot\nabla\right)D^{(n)}\right\},} \tag{3.84}$$

$$\boxed{\mathbf{u}^{(n+1)} = \mathbf{u}^{(n)} - \frac{\triangle\tau}{\rho}\nabla p^{(n+1)} - \triangle\tau\left[\left(\mathbf{u}\cdot\nabla\right)\mathbf{u}\right]^{(n)} + \triangle\tau\nu\nabla^2\mathbf{u}^{(n)} + \triangle\tau\,\mathbf{g}.} \tag{3.85}$$

3.1. A két-lépcsős pszeudo-tranziens nyomás-sebesség összekapcsolási (3.84)–(3.85) algoritmus [57], [T9] egy pszeudo-tranziens nyomásprojekciós módszer, amely levezethető vagy a Harlow és Welch [59] projekciós módszeréből vagy a Chorin-féle [52] FS-PP módszerből [57, p. 2], [T9, p. 2].

3.2. Levezettem és megállapítottam, hogy a Harlow és Welch [59] két-lépcsős nyomásprojekciós módszere (3.67)–(3.68) megegyezik a Chorin-féle [52] három-lépcsős FS-PP módszerrel (3.51)–(3.53). A különbség közöttük az egyenleteik diszkretizációjában van, de mint a Navier–Stokes egyenlet (3.50) megoldására érvényes keretrendszerek azonosak [57, p. 2-4], [T9, p. 2-4].

3.3. Egy saját készítésű C kódot fejlesztettem ki a két-lépcsős pszeudo-tranziens nyomás-sebesség összekapcsolási algoritmus alapegyenleteinek (3.84)–(3.85) numerikus megoldására a Véges Differenciák Módszerének (VDM) használatával. A pszeudo-idő derivált diszkretizálására egy elsőrendű hibataggal rendelkező előrelépő sémát alkalmaztam. A nem-lináris konvektív tagok számítására a Torrance és Rockett [112] által javasolt előrelépő sémát használtam. A többi térbeli tag diszktretizációja másodrendű hibataggal rendelkező centrális sémák alkalmazásával történt [57, p. 6], [T9, p. 6].

3.4. A saját készítésű C kód verifikációját és a két-lépcsős pszeudo-tranziens nyomás-sebesség összekapcsolási algoritmus (3.84)–(3.85) validálását egy mintafeladaton végeztem el egy kétdimenziós vízszintes mikrocsatornában történő áramlás szimulációjára $Re = 10$ esetén. A numerikus megoldás maximum relatív hibája 2% volt összehasonítva egy egyszerűsített analitikus megoldással a csatorna kimeneti szakaszánál [57, p. 8], [T9, p. 8].

3.5. Megállapítottam, hogy a kifejlesztett két-lépcsős pszeudo-tranziens megközelítés (3.84)–(3.85) helyettesítheti a nyomás-Poisson egyenlet (3.55) megoldását összenyomhatatlan folyadékáramlások számításakor és kiküszöbölheti a nyomásmező oszcilláló megoldását kis Re számú áramlás esetén, amikor a primitív változók u, v, p megegyező számítási hálópontokon vannak elhelyezve (lásd 3.8 ábrát) [57, p. 7], [T9, p. 7].

References

[1] G. I. Taylor, 'The Statistical Theory of Turbulence', *Jour. Aero. Sci.*, vol. 4(8), pp. 311–315, 1937.

[2] T. von Kármán, 'The Fundamentals of the Statistical Theory of Turbulence', *Jour. Aero. Sci.*, vol. 4, pp. 131–138, 1937.

[3] A. Kolmogorov, 'Local Structure of Turbulence in Incompressible Viscous Fluid for Very Large Reynolds Number', *Doklady Akademija Nauk, SSSR*, vol. 30, pp. 299–303, 1941.

[4] J. Boussinesq, 'Théorie de l'Ecoulement tourbillant', *Mem. Présentés par Divers Savants Acad. Sci. Inst. Fr.*, vol. 23, pp. 46–50, 1877.

[5] P. A. Davidson, *Turbulence. An Introduction for Scientists and Engineers*. Oxford University Press Inc.: New York, USA, ISBN 978-0-19-852949-1, 2004.

[6] **L. Könözsy**, 'A New Hypothesis on the Anisotropic Reynolds Stress Tensor', *Fluid Mechanics and Its Applications*, vol. 120, pp. 105–135, 2019, ISSN: 0926-5112. DOI: 10.1007/978-3-030-13543-0_5.

[7] T. Czibere, 'Three Dimensional Stochastic Model of Turbulence', *J. Comp. and App. Mech.*, vol. 2, no. 5, pp. 7–20, 2001.

[8] T. Czibere, 'Calculating Turbulent Flows Based on a Stochastic Model', *J. Comp. and App. Mech.*, vol. 7(2), pp. 155–188, 2006.

[9] F. R. Menter, 'Improved Two-Equation k-ω Turbulence Models for Aerodynamic Flows', *NASA Technical Memorandum 103975*, pp. 1–31, 1992.

[10] F. R. Menter, 'Improved Two-Equation Eddy-Viscosity Turbulence Models for Engineering Applications', *AIAA J.*, vol. 32(8), pp. 1598–1605, 1994.

[11] B. J. Daly and F. H. Harlow, 'Transport Equations in Turbulence', *Phys. Fluids*, vol. 13(11), pp. 2634–2649, 1970.

References

[12] B. E. Launder, G. J. Reece and W. Rodi, 'Progress in the Development of a Reynolds-Stress Turbulence Closure', *J. Fluid Mech.*, vol. 68, no. Part 3, pp. 537–566, 1975.

[13] S. B. Pope, 'A More General Effective-Viscosity Hypothesis', *J. Fluid Mech.*, vol. 72, no. Part 2, pp. 331–340, 1975.

[14] C. G. Speziale, S. Sarkar and T. B. Gatski, 'Modelling the Pressure-Strain Correlation of Turbulence - An Invariant Dynamical Systems Approach', *NASA Contractor Report 181979. ICASE Report*, vol. 90-5, 1990.

[15] B. Eisfeild and O. Brodersen, 'Advanced Turbulence Modelling and Stress Analysis for the DLR-F6 Configuration', in *23rd AIAA Applied Aerodynamics Conference, Fluid Dynamics and Co-located Conferences*, https://doi.org/10.2514/6.2005-4727, vol. 2005-4727, 2005, pp. 1–14.

[16] C. Klajbár, **L. Könözsy** and K. W. Jenkins, 'A Modified SSG/LLR-ω Reynolds Stress Model for Predicting Bluff Body Aerodynamics', in *VII European Cong. on Comp. Methods in App. Sci. and Eng. ECCOMAS Congress*, M. Papadrakakis, V. Papadopoulos, G. Stefanou and V. Plevris, Eds., 2016, pp. 936–948.

[17] S. B. Pope, *Turbulent Flows*. Cambridge University Press: Cambridge, United Kingdom, ISBN 978-0-521-59886-6, 2000.

[18] **L. Könözsy**, *A New Hypothesis on the Anisotropic Reynolds Stress Tensor for Turbulent Flows, Volume I: Theoretical Background and Development of an Anisotropic Hybrid k-omega Shear-Stress Transport/Stochastic Turbulence Model*. Fluid Mechanics and Its Applications Series, Springer Nature Switzerland AG, 2019, ISBN: 9783030135423. DOI: 10.1007/978-3-030-13543-0.

[19] T. J. Craft, Launder and K. B. E. Suga, 'Development and Application of a Cubic Eddy-Viscosity Model of Turbulence', *Int. J. Heat and Fluid Flow*, vol. 17, pp. 108–115, 1996.

[20] T. J. Craft, B. E. Launder and K. Suga, 'Prediction of Turbulent Transitional Phenomena with a Nonlinear Eddy-Viscosity Model', *Int. J. Heat and Fluid Flow*, vol. 18, pp. 15–28, 1997.

[21] K. Abe, Y.-J. Jang and M. A. Leschziner, 'An Investigation of Wall-Anisotropy Expressions and Length-Scale Equations for Non-Linear Eddy-Viscosity Models', *Int. J. Heat and Fluid Flow*, vol. 24, pp. 181–198, 2003.

[22] F. Vitillo, C. Galati, L. Cachona, E. Laroche and P. Millan, 'An Anisotropic Shear Stress Transport (ASST) Model Formulation', *Comput. Math. Appl.*, vol. 70, pp. 2238–2251, 2015.

[23] F. R. Menter, M. Kuntz and R. Langtry, '4th Internal Symposium, Turbulence, Heat and Mass Transfer, 2003, Antalya, Turkey', in K. Hanjalić, Y. Nagano and M. Tummers, Eds. Begell House, Inc., New York, Wallingford, 2003, vol. 4, ch. Ten Years of Industrial Experience with the SST Turbulence Model, pp. 625–632, ISBN 1567001963.

[24] **L. Könözsy**, *A New Hypothesis on the Anisotropic Reynolds Stress Tensor for Turbulent Flows, Volume II: Practical Implementation and Applications of an Anisotropic Hybrid k-omega Shear-Stress Transport/Stochastic Turbulence Model*. Fluid Mechanics and Its Applications Series, Springer Nature Switzerland AG, 2021, ISBN: 9783030606022. DOI: 10.1007/978-3-030-60603-9.

[25] T. von Kármán, 'Mechanische Ähnlichkeit und Turbulenz', *Nachrichten von der Gesellschaft der Wissenschaften zu Göttingen. Mathematisch-Physikalische Klasse*, pp. 58–76, 1930.

[26] T. von Kármán, 'Mechanische Ähnlichkeit und Turbulenz', in *Proceedings of the Third International Congress of Applied Mechanics*, P. A. Norstedt & Söner, Stockholm, 1930.

[27] T. von Kármán, 'Mechanical Similitude and Turbulence', *National Advisory Committee for Aeronautics (N. A. C. A.) Technical Memorandum No. 611, Washington, USA; English Translation by Vanier, J.*, pp. 1–21, 1931.

[28] R. A. Antonia, L. Djenidi and P. R. Spalart, 'Anisotropy of the Dissipation Tensor in a Turbulent Boundary Layer', *Phys. Fluids*, vol. 6(7), pp. 2475–2479, 1994.

[29] J. Bakosi and J. R. Ristorcelli, 'Probability Density Function Method for Variable-Density Pressure-Gradient-Driven Turbulence and Mixing', Technical Report, Los Alamos National Laboratory (LANL), Tech. Rep., 2010.

[30] J. Bakosi and J. R. Ristorcelli, 'Probability Density Function Method for Variable-Density Pressure-Gradient-Driven Turbulence and Mixing', in *49th AIAA Aerospace Sciences Meeting, Orlando, Florida*, 2011, pp. 1–15.

[31] P. Raje and K. Sinha, 'Anisotropic SST Turbulence Model for Shock-Boundary Layer Interaction', *Computers and Fluids*, vol. 228, p. 105 072, 2021. DOI: https://doi.org/10.1016/j.compfluid.2021.105072.

[32] H. Tennekes and J. L. Lumley, 'A First Course in Turbulence', in The MIT Press: Cambridge, Massachusetts, USA, ISBN 978-0-262-20019-6, 1972, ch. Vorticity Dynamics, pp. 75–94.

[33] A. Einstein, 'The Collected Papers of Albert Einstein. Volume 6. The Berlin Years: Writings, 1914-1917. English Translation of Selected Text. DOC. 30', in A. J. Kox, M. J. Klein and R. Schulmann, Eds. Princeton University Press, New Jersey 08540, USA, 1997, ch. The Foundation of the General Theory of Relativity, p. 158.

References

[34] R. Aris, *Vectors Tensors and Basic Equations of Fluid Mechanics*. Dover Publications, Inc.: New York, USA, ISBN 0-486-66110-5, 1962.

[35] K. Karamcheti, *Vector Analysis and Cartesian Tensors with Selected Applications*. Holden-Day: San Francisco, California, USA, 1967.

[36] P. Bradshaw, 'The Turbulence Structure of Equilibrium Boundary Layers', *J. Fluid Mech.*, vol. 29, no. Part 4, pp. 625–645, 1967.

[37] **L. Könözsy**, 'The Anisotropic Hybrid k-ω SST/Stochastic Turbulence Model', *Fluid Mechanics and Its Applications*, vol. 125, pp. 115–140, 2021, ISSN: 0926-5112. DOI: 10.1007/978-3-030-60603-9_2.

[38] **L. Könözsy**, 'Implementation of the Anisotropic Hybrid k-ω SST/STM Closure Model', *Fluid Mechanics and Its Applications*, vol. 125, pp. 141–214, 2021, ISSN: 0926-5112. DOI: 10.1007/978-3-030-60603-9_3.

[39] F. R. Menter, 'Turbulence Modeling for Engineering Flows', *A Technical Paper from ANSYS, Inc.*, pp. 1–25, 2011.

[40] P. Bradshaw, D. H. Ferriss and N. P. Atwell, 'Calculation of Boundary-Layer Development Using the Turbulent Energy Equation', *J. Fluid Mech.*, vol. 28, no. Part 3, pp. 593–616, 1967.

[41] D. C. Wilcox, 'The Reassessment of the Scale-Determining Equation for Advanced Turbulence Models', *AIAA J.*, vol. 26, pp. 1299–1310, 1988.

[42] D. C. Wilcox, *Turbulence Modeling for CFD*. DCW Industries, Inc.: Glendale, California, USA, First Edition, ISBN 0-9636051-0-0, 1993.

[43] W. P. Jones and B. E. Launder, 'The Calculation of Low-Reynolds-Number-Phenomena with a Two-Equation Model of Turbulence', *Int. J. Heat Mass Transfer*, vol. 16, pp. 1119–1130, 1973.

[44] **L. Könözsy**, 'Two-Dimensional Simulations with an Anisotropic Hybrid k-ω SST/STM Approach', *Fluid Mechanics and Its Applications*, vol. 125, pp. 215–357, 2021, ISSN: 0926-5112. DOI: 10.1007/978-3-030-60603-9_4.

[45] **L. Könözsy**, 'Three-Dimensional Simulations with an Anisotropic Hybrid k-ω SST/STM Approach', *Fluid Mechanics and Its Applications*, vol. 125, pp. 359–404, 2021, ISSN: 0926-5112. DOI: 10.1007/978-3-030-60603-9_5.

[46] P. S. Klebanoff, 'Characteristics of Turbulence in a Boundary Layer with Zero Pressure Gradient', *NACA Report 1247*, 1954.

[47] J. Laufer, 'The Structure of Turbulence in Fully Developed Pipe Flow', *NACA Technical Report 1174*, 1954.

[48] P. S. Klebanoff and Z. W. Diehl, 'Some Features of Artificially Thickened Fully Developed Turbulent Boundary Layers with Zero Pressure Gradient', *NACA Technical Note 2475*, 1951.

[49] 'NASA Langley Research Center Turbulence Modeling Resource', NASA. [Online]. Available: https://turbmodels.larc.nasa.gov/.

[50] I. ANSYS, 'ANSYS Fluent Theory Guide, Release 19.1', *Canonsburg, PA, USA: ANSYS Inc.*, 2018.

[51] A. J. Chorin, 'A numerical method for solving incompressible viscous flow problems', *Journal of Computational Physics*, vol. 2, pp. 12–26, 1967.

[52] A. J. Chorin, 'Numerical solution of the Navier-Stokes equations', *Math. Comp.*, vol. 22, pp. 745–762, 1968.

[53] **L. Könözsy**, 'Multiphysics CFD Modelling of Incompressible Flows at Low and Moderate Reynolds Numbers', Ph.D. dissertation, Department of Engineering Physics, College of Aeronautics, Cranfield University, Cranfield, Bedfordshire, MK43 0AL, United Kingdom, 2012.

[54] **L. Könözsy** and D. Drikakis, 'A Unified Fractional-Step, Artificial Compressibility and Pressure-Projection Formulation for Solving the Incompressible Navier–Stokes Equations', *Communications in Computational Physics*, vol. 16, no. 5, pp. 1135–1180, 2014, ISSN: 1815-2406. DOI: 10.4208/cicp.240713.080514a.

[55] T.-R. Teschner, **L. Könözsy** and K. W. Jenkins, 'Predicting Non-Linear Flow Phenomena Through Different Characteristics-Based Schemes', *Aerospace*, vol. 5, no. 1:22, pp. 1–20, 2018. DOI: 10.3390/aerospace5010022.

[56] T.-R. Teschner, **L. Könözsy** and K. W. Jenkins, 'A Generalised and Low-Dissipative Multi-Directional Characteristics-Based Scheme with Inclusion of the Local Riemann Problem Investigating Incompressible Flows without Free-Surfaces', *Computer Physics Communications*, vol. 239, pp. 283–310, 2019, ISSN: 0010-4655. DOI: 10.1016/j.cpc.2018.07.026.

[57] **L. Könözsy**, 'Pseudo-Transient Pressure-Momentum Coupling Method for Low-Speed Incompressible Flows', in *MultiScience - XXXI. microCAD International Multidisciplinary Scientific Conference*, Miskolci Egyetem, 2017. [Online]. Available: https://www.uni-miskolc.hu/~microcad/publikaciok/2017/index.html.

[58] G. Karniadakis, A. Beskok and N. Aluru, 'Microflows and nanoflows', *Springer, New York*, 2005.

[59] F. H. Harlow and J. E. Welch, 'Numerical calculation of time-dependent incompressible flow of fluid with free surfaces', *Physics of Fluids*, vol. 8, no. 12, pp. 2182–2189, 1965.

[60] R. Peyret and T. Taylor, 'Computational methods for fluid flow', *Springer-Verlag, Berlin*, 1983.

[61] N. Monokrousos, **L. Könözsy**, V. Pachidis, E. Sozio and F. Rossi, 'A Numerical Approach to Overcome the Very-Low Reynolds Number Limitation of the Artificial Compressibility for Incompressible Flows', *Heliyon*, vol. 10, no. 21, e39587, 2024. DOI: https://doi.org/10.1016/j.heliyon.2024.e39587.

[62] D. Drikakis, P. A. Govatsos and D. E. Papatonis, 'A characteristic-based method for incompressible flows', *International Journal for Numerical Methods in Fluids*, vol. 19, pp. 667–685, 1994.

[63] D. Drikakis, O. P. Iliev and D. P. Vassileva, 'A nonlinear multigrid method for the three-dimensional incompressible Navier-Stokes equations', *Journal of Computational Physics*, vol. 146, pp. 301–321, 1998.

[64] D. Drikakis, 'A parallel multiblock characteristic-based method for three-dimensional incompressible flows', *Advances in Engineering Software*, vol. 26, pp. 111–119, 1996.

[65] K. Zamzamian and S. E. Razavi, 'Multidimensional upwinding for incompressible flows based on characteristics', *Journal of Computational Physics*, vol. 227, pp. 8699–8713, 2008.

[66] E. Shapiro and D. Drikakis, 'Artificial compressibility, characteristics-based schemes for variable density, incompressible, multi-species flows. part i. derivation of different formulations and constant density limit', *Journal of Computational Physics*, vol. 210, pp. 584–607, 2005.

[67] R. Temam, 'Sur l'approximation de la solution des equations de Navier-Stokes par la methode des pas fractionnaires (i)', *Arch. Rat. Mech. Anal.*, vol. 32, pp. 377–385, 1969.

[68] O. A. Ladyzhenskaya, 'The Mathematical Theory of Viscous Incompressible Flow', *Gordon and Breach Science Publishers, Inc., New York*, 1969.

[69] J. B. Bell, P. Colella and H. M. Glaz, 'A second-order projection method for the incompressible Navier-Stokes equations', *Journal of Computational Physics*, vol. 85, pp. 257–283, 1989.

[70] J. B. Bell and D. L. Marcus, 'A second-order projection method for variable-density flows', *Journal of Computational Physics*, vol. 101, pp. 334–348, 1992.

References

[71] A. S. Almgren, J. B. Bell, P. Colella, L. H. Howell and M. L. Welcome, 'A conservative adaptive projection method for the variable density incompressible Navier-Stokes equations', *Journal of Computational Physics*, vol. 142, pp. 1–46, 1998.

[72] R. B. Pember, L. H. Howell, J. B. Bell, P. Colella, W. Y. Crutchfield, W. A. Fiveland and J. P. Jessee, 'An adaptive projection method for unsteady low-Mach number combustion', *Combustion Science and Technology*, vol. 140, pp. 123–168, 1998.

[73] R. Codina, M. Vázquez and O. C. Zienkiewicz, 'A General Algorithm for Compressible and Incompressible Flows. Part III: The Semi-Implicit Form', *Int. J. Numer. Meth. Fl.*, vol. 27, pp. 13–32, 1998.

[74] S. V. Patankar and D. B. Spalding, 'A calculation procedure for heat mass and momentum transfer in three-dimensional parabolic flows', *Int. J. Heat and Mass Transfer*, vol. 15, pp. 1787–1806, 1972.

[75] S. V. Patankar, 'Numerical Hear Transfer and Fluid Flow', *Hemisphere Publishing Corporation, Taylor and Francis Group, New York*, 1980.

[76] H. K. Versteeg and W. Malalasekera, 'Introduction to Computational Fluid Dynamics - The Finite Volume Method', *Longman Group Ltd., First Edition*, 1995.

[77] J. H. Ferziger and M. Perić, *Computational Methods for Fluid Dynamics*. Springer-Verlag, Berlin, Heidelberg, Germany, ISBN 3-540-42074-6, 2002.

[78] O. C. Zienkiewicz and R. Codina, 'A General Algorithm for Compressible and Incompressible Flow - Part I. The Split, Characteristic-Based Scheme', *Int. J. Numer. Meth. Fl.*, vol. 20, pp. 869–885, 1995.

[79] O. C. Zienkiewicz, K. Morgan, B. V. K. S. Sai, R. Codina and M. Vasquez, 'A General Algorithm for Compressible and Incompressible Flow - Part II. Tests on the Explicit Form', *Int. J. Numer. Meth. Fl.*, vol. 20, pp. 887–913, 1995.

[80] O. C. Zienkiewicz, B. V. K. S. Sai, K. Morgan and R. Codina, 'Split, Characteristic Based Semi-Implicit Algorithm for Laminar/Turbulent Incompressible Flows', *Int. J. Numer. Meth. Fl.*, vol. 23, pp. 787–809, 1996.

[81] O. C. Zienkiewicz, P. Nithiarasu, R. Codina, M. Vázquez and P. Ortiz, 'The Characteristic-Based-Split Procedure: An Efficient and Accurate Algorithm for Fluid Problems', *Int. J. Numer. Meth. Fl.*, vol. 31, pp. 359–392, 1999.

[82] P. Nithiarasu, 'An efficient artificial compressibility (ac) scheme based on the characteristic based split (cbs) method for incompressible flows', *Int. J. Numer. Meth. Engng.*, vol. 56, pp. 1815–1845, 2003.

[83] P. Nithiarasu, 'An Efficient Artificial Compressibility (AC) Scheme based on the Characteristic based Split (CBS) Method for Incompressible Flows', *Int. J. Numer. Meth. Engng.*, vol. 56, pp. 1815–1845, 2003.

[84] H. S. Tang and F. Sotiropoulos, 'Fractional step artificial compressibility schemes for the unsteady incompressible Navier-Stokes equations', *Computers and Fluids*, vol. 36, pp. 974–986, 2007.

[85] **L. Könözsy** and D. Drikakis, 'A Coupled High-Resolution Fractional-Step Artificial Compressibility and Pressure-Projection Formulation for Solving Incompressible Multi-Species Variable Density Flow Problem at Low Reynolds Numbers', in *CD-ROM Proceedings of the 6th European Congress on Computational Methods in Applied Sciences and Engineering (ECCOMAS), 2012, Vienna, Austria, Eds.: Eberhardsteiner, J.; Böhm, H.J.; Rammerstorfer, F.G., Publisher: Vienna University of Technology, Austria, pp. 1-15.*, 2012, pp. 3206–3220.

[86] D. Drikakis and W. Rider, 'High-Resolution Methods for Incompressible and Low-Speed Flows', *Springer-Verlag, Berlin*, 2005.

[87] P. Tsoutsanis, I. Kokkinakis, **L. Könözsy**, D. Drikakis, R. Williams and D. Youngs, 'Comparison of Structured- and Unstructured-Grid, Compressible and Incompressible Methods Using the Vortex Pairing Problem', *Computer Methods in Applied Mechanics and Engineering*, vol. 293, pp. 207–231, 2015. DOI: https://doi.org/10.1016/j.cma.2015.04.010.

[88] M. Griebel, T. Dornseifer and T. Neunhoeffer, 'Numerical simulation in fluid dynamics', *Society for Industrial and Applied Mathematics (SIAM)*, 1998.

[89] R. Courant and D. Hilbert, 'Methods of mathematical physics', *John Wiley and Sons Inc., New York*, 1991.

[90] C.-W. Shu and S. Osher, 'Efficient implementation of essentially non-oscillatory shock-capturing schemes', *Journal of Computational Physics*, vol. 77, pp. 439–471, 1988.

[91] M. F. Tome and S. McKee, 'Gensmac - a computational marker and cell method for free surface flows in general domains', *Journal of Computational Physics*, vol. 110, pp. 171–186, 1994.

[92] P. Roache, 'Computational fluid dynamics', *Albuquerque: Hermosa*, 1976.

[93] G.-S. Jiang and C.-W. Shu, 'Efficient implementation of weighted eno schemes', *Journal of Computational Physics*, vol. 126, pp. 202–228, 1996.

[94] C.-W. Shu, 'Essentially non-oscillatory and weighted essentially non-oscillatory schemes for hyperbolic conservation laws', *NASA/CR-97-206253, ICASE Report No. 97-65*, 1997.

References

[95] D. S. Balsara and C.-W. Shu, 'Monotonicity preserving weighted essentially non-oscillatory schemes with increasingly high order of accuracy', *Journal of Computational Physics*, vol. 160, pp. 405–452, 2000.

[96] E. F. Toro, 'Riemann Solvers and Numerical Methods for Fluid Dynamics', *Springer-Verlag, First Edition, Berlin*, 1997.

[97] E. Shapiro and D. Drikakis, 'Artificial compressibility, characteristics-based schemes for variable-density, incompressible, multispecies flows: Part II. Multigrid implementation and numerical tests', *Journal of Computational Physics*, vol. 210, pp. 608–631, 2005.

[98] U. Ghia, K. N. Ghia and C. T. Shin, 'High-Re solutions for incompressible flow using the Navier-Stokes equations and a multigrid method', *Journal of Computational Physics*, vol. 48, pp. 387–411, 1982.

[99] A. K. Prasad and J. R. Koseff, 'Reynolds number and end-wall effects on a lid-driven cavity flow', *Physics of Fluids A*, vol. 1, no. 2, pp. 208–218, 1989.

[100] H. Chaudhary, **L. Könözsy** and Z. A. Rana, 'A Novel Combination of Mathematical Modelling Approaches for Simulating Nearly Hypersonic, Viscous, Reacting Magnetogasdynamic Flows', *Applied Mathematical Modelling*, vol. 107, pp. 464–507, 2022, ISSN: 0307-904X. DOI: 10.1016/j.apm.2022.02.041.

[101] D. Drikakis and W. Rider, *High-Resolution Methods for Incompressible and Low-Speed Flows*, K.-J. Bathe, Ed. Springer-Verlag, Berlin, Heidelberg, Germany, ISBN 3-540-22136-0, 2005.

[102] F. F. Grinstein, L. G. Margolin and W. J. Rider, 'Implicit large eddy simulation: Computing turbulent fluid dynamics', *Cambridge University Press*, 2007.

[103] R. M. Fearn, T. Mullin and K. A. Cliffe, 'Nonlinear flow phenomena in a symmetric sudden expansion', *Journal of Fluid Mechanics*, vol. 211, pp. 595–608, 1990. DOI: 10.1017/S0022112090001707.

[104] A. Toutant, 'General and Exact Pressure Evolution Equation', *Physics Letters A*, vol. 381, no. 44, pp. 3739–3742, 2017. DOI: https://doi.org/10.1016/j.physleta.2017.10.008.

[105] A. Toutant, 'Numerical Simulations of Unsteady Viscous Incompressible Flows using General Pressure Equation', *Journal of Computational Physics*, vol. 374, pp. 822–842, 2018. DOI: https://doi.org/10.1016/j.jcp.2018.07.058.

[106] D. Dupuy, A. Toutant and F. Bataille, 'Analysis of Artificial Pressure Equations in Numerical Simulations of a Turbulent Channel Flow', *Journal of Computational Physics*, vol. 411, p. 109 407, 2020. DOI: https://doi.org/10.1016/j.jcp.2020.109407.

[107] A. M. Alsaghir, S. Mishra, S. Abdallah and J.-H. Bahk, 'A Pseudo-Transient Pressure Gradient Method for Solving the Incompressible Navier-Stokes Equations', *Physics of Fluids*, vol. 37, no. 1, p. 013 618, Jan. 2025. DOI: https://doi.org/10.1063/5.0249017.

[108] L. Baranyi and M. Shirakashi, 'Numerical Solution for Laminar Unsteady Flow about Fixed and Oscillating Cylinders', *Computer Assisted Methods in Engineering and Science*, vol. 6, no. 3-4, pp. 263–277, 1999. [Online]. Available: https://cames.ippt.pan.pl/index.php/cames/article/view/1275.

[109] L. Baranyi, 'Computation of Unsteady Momentum and Heat Transfer from a Fixed Circular Cylinder in Laminar Flow', *Journal of Computational and Applied Mechanics*, vol. 4, no. 1, pp. 13–25, 2003.

[110] L. Baranyi, 'Numerical Simulation of Flow around an Orbiting Cylinder at Different Ellipticity Values', *Journal of Fluids and Structures*, vol. 24, no. 6, pp. 883–906, 2008. DOI: https://doi.org/10.1016/j.jfluidstructs.2007.12.006.

[111] C. Fletcher, *Computational Techniques for Fluid Dynamics, Specific Techniques for Different Flow Categories*, First Edition. Springer-Verlag, Berlin, 1988, vol. 2.

[112] K. E. Torrance and J. A. Rockett, 'Numerical study of natural convection in an enclosure with localized heating from below-creeping flow to the oneset of laminar instability', *Journal of Fluid Mechanics*, vol. 36, pp. 33–54, 1969.

References to the Author's Contributions

[T1] **L. Könözsy**, 'A New Hypothesis on the Anisotropic Reynolds Stress Tensor', *Fluid Mechanics and Its Applications*, vol. 120, pp. 105–135, 2019, ISSN: 0926-5112. DOI: 10.1007/978-3-030-13543-0_5.

[T2] **L. Könözsy**, 'The Anisotropic Hybrid k-ω SST/Stochastic Turbulence Model', *Fluid Mechanics and Its Applications*, vol. 125, pp. 115–140, 2021, ISSN: 0926-5112. DOI: 10.1007/978-3-030-60603-9_2.

[T3] **L. Könözsy**, 'Implementation of the Anisotropic Hybrid k-ω SST/STM Closure Model', *Fluid Mechanics and Its Applications*, vol. 125, pp. 141–214, 2021, ISSN: 0926-5112. DOI: 10.1007/978-3-030-60603-9_3.

[T4] **L. Könözsy**, 'Two-Dimensional Simulations with an Anisotropic Hybrid k-ω SST/STM Approach', *Fluid Mechanics and Its Applications*, vol. 125, pp. 215–357, 2021, ISSN: 0926-5112. DOI: 10.1007/978-3-030-60603-9_4.

[T5] **L. Könözsy**, 'Three-Dimensional Simulations with an Anisotropic Hybrid k-ω SST/STM Approach', *Fluid Mechanics and Its Applications*, vol. 125, pp. 359–404, 2021, ISSN: 0926-5112. DOI: 10.1007/978-3-030-60603-9_5.

[T6] **L. Könözsy** and D. Drikakis, 'A Unified Fractional-Step, Artificial Compressibility and Pressure-Projection Formulation for Solving the Incompressible Navier–Stokes Equations', *Communications in Computational Physics*, vol. 16, no. 5, pp. 1135–1180, 2014, ISSN: 1815-2406. DOI: 10.4208/cicp.240713.080514a.

[T7] T.-R. Teschner, **L. Könözsy** and K. W. Jenkins, 'Predicting Non-Linear Flow Phenomena Through Different Characteristics-Based Schemes', *Aerospace*, vol. 5, no. 1:22, pp. 1–20, 2018. DOI: 10.3390/aerospace5010022.

[T8] T.-R. Teschner, **L. Könözsy** and K. W. Jenkins, 'A Generalised and Low-Dissipative Multi-Directional Characteristics-Based Scheme with Inclusion of the Local Riemann Problem Investigating Incompressible Flows without Free-Surfaces', *Computer Physics Communications*, vol. 239, pp. 283–310, 2019, ISSN: 0010-4655. DOI: 10.1016/j.cpc.2018.07.026.

References to the Author's Contributions

[T9] **L. Könözsy**, 'Pseudo-Transient Pressure-Momentum Coupling Method for Low-Speed Incompressible Flows', in *MultiScience - XXXI. microCAD International Multidisciplinary Scientific Conference*, Miskolci Egyetem, 2017. [Online]. Available: https://www.uni-miskolc.hu/~microcad/publikaciok/2017/index.html.

[T10] H. Chaudhary, **L. Könözsy** and Z. A. Rana, 'A Novel Combination of Mathematical Modelling Approaches for Simulating Nearly Hypersonic, Viscous, Reacting Magnetogasdynamic Flows', *Applied Mathematical Modelling*, vol. 107, pp. 464–507, 2022, ISSN: 0307-904X. DOI: 10.1016/j.apm.2022.02.041.

Author's Selected Publications

[SP1] N. Monokrousos, **L. Könözsy**, V. Pachidis, E. Sozio and F. Rossi, 'A Numerical Approach to Overcome the Very-Low Reynolds Number Limitation of the Artificial Compressibility for Incompressible Flows', *Heliyon*, vol. 10, 2024. DOI: 10.1016/j.heliyon.2024.e39587.

[SP2] H. Chaudhary, **L. Könözsy** and Z. A. Rana, 'A Novel Combination of Mathematical Modelling Approaches for Simulating Nearly Hypersonic, Viscous, Reacting Magnetogasdynamic Flows', *Applied Mathematical Modelling*, vol. 107, pp. 464–507, 2022, ISSN: 0307-904X. DOI: 10.1016/j.apm.2022.02.041.

[SP3] J. F. Townsend, S.-I. Inutsuka, **L. Könözsy** and K. W. Jenkins, 'On High-Order Numerical Schemes for Viscous Relativistic Hydrodynamics Through the Kelvin-Helmholtz Instability', *Monthly Notices of The Royal Astronomical Society*, vol. 515, pp. 451–472, 2022, ISSN: 0035-8711. DOI: 10.1093/mnras/stac1741.

[SP4] M. Righi, V. Pachidis, **L. Könözsy**, T. Giersch and S. Schrape, 'Experimental Validation of a Three-Dimensional Through-Flow Model for High-Speed Compressor Surge', *Aerospace Science and Technology*, vol. 128, 2022, ISSN: 1270-9638. DOI: 10.1016/j.ast.2022.107775.

[SP5] **L. Könözsy**, 'Introduction to Classical Analytical Solutions for Wall-Bounded Turbulence', *Fluid Mechanics and Its Applications*, vol. 125, pp. 1–113, 2021, ISSN: 0926-5112. DOI: 10.1007/978-3-030-60603-9_1.

[SP6] **L. Könözsy**, 'The Anisotropic Hybrid k-ω SST/Stochastic Turbulence Model', *Fluid Mechanics and Its Applications*, vol. 125, pp. 115–140, 2021, ISSN: 0926-5112. DOI: 10.1007/978-3-030-60603-9_2.

[SP7] **L. Könözsy**, 'Implementation of the Anisotropic Hybrid k-ω SST/STM Closure Model', *Fluid Mechanics and Its Applications*, vol. 125, pp. 141–214, 2021, ISSN: 0926-5112. DOI: 10.1007/978-3-030-60603-9_3.

[SP8] **L. Könözsy**, 'Two-Dimensional Simulations with an Anisotropic Hybrid k-ω SST/STM Approach', *Fluid Mechanics and Its Applications*, vol. 125, pp. 215–357, 2021, ISSN: 0926-5112. DOI: 10.1007/978-3-030-60603-9_4.

[SP9] **L. Könözsy**, 'Three-Dimensional Simulations with an Anisotropic Hybrid k-ω SST/STM Approach', *Fluid Mechanics and Its Applications*, vol. 125, pp. 359–404, 2021, ISSN: 0926-5112. DOI: 10.1007/978-3-030-60603-9_5.

[SP10] M. Righi, V. Pachidis and **L. Könözsy**, 'On the Prediction of the Reverse Flow and Rotating Stall Characteristics of High-Speed Axial Compressors Using a Three-Dimensional Through-Flow Code', *Aerospace Science and Technology*, vol. 99, 2020, ISSN: 1270-9638. DOI: 10.1016/j.ast.2019.105578.

[SP11] M. A. Hossain, S. A. Nabavi, P. Ranganathan, **L. Könözsy** and V. Manovic, '3D CFD Modelling of Liquid Dispersion in Structured Packed Bed Column for CO2 Capture', *Chemical Engineering Science*, vol. 225, 2020, ISSN: 0009-2509. DOI: 10.1016/j.ces.2020.115800.

[SP12] P. Bagul, Z. A. Rana, K. W. Jenkins and **L. Könözsy**, 'Computational Engineering Analysis of External Geometrical Modifications on MQ-1 Unmanned Combat Aerial Vehicle', *Chinese Journal of Aeronautics*, vol. 33, pp. 1154–1165, 2020, ISSN: 1000-9361. DOI: 10.1016/j.cja.2019.12.027.

[SP13] J. F. Townsend, **L. Könözsy** and K. W. Jenkins, 'On the Development of a Rotated-Hybrid HLL/HLLC Approximate Riemann Solver for Relativistic Hydrodynamics', *Monthly Notices of The Royal Astronomical Society*, vol. 496, pp. 2493–2505, 2020, ISSN: 0035-8711. DOI: 10.1093/mnras/staa1648.

[SP14] T.-R. Teschner, **L. Könözsy** and K. W. Jenkins, 'A Generalised and Low-Dissipative Multi-Directional Characteristics-Based Scheme with Inclusion of the Local Riemann Problem Investigating Incompressible Flows without Free-Surfaces', *Computer Physics Communications*, vol. 239, pp. 283–310, 2019, ISSN: 0010-4655. DOI: 10.1016/j.cpc.2018.07.026.

[SP15] L. Casadei, **L. Könözsy** and N. J. Lawson, 'Unsteady Detached-Eddy Simulation (DES) of the Jetstream 31 Aircraft in One Engine Inoperative (OEI) Condition with Propeller Modelling', *Aerospace Science and Technology*, vol. 91, pp. 287–300, 2019, ISSN: 1270-9638. DOI: 10.1016/j.ast.2019.05.034.

[SP16] M. Righi, V. Pachidis, **L. Könözsy** and L. Pawsey, 'Three-Dimensional Through-Flow Modelling of Axial Flow Compressor Rotating Stall and Surge', *Aerospace Science and Technology*, vol. 78, pp. 271–279, 2018, ISSN: 1270-9638. DOI: 10.1016/j.ast.2018.04.021.

[SP17] D. Sebastia-Saez, S. Gu, **L. Könözsy**, J.-U. Repke and H. Arellano-García, 'On the Effect of the Froude Number on the Interface Area of Gravity-Driven Liquid Rivulets', *Chemical Engineering Research and Design*, vol. 130, pp. 208–218, 2018, ISSN: 0263-8762. DOI: 10.1016/j.cherd.2017.12.003.

Author's Selected Publications

[SP18] M. Szőke, T. Józsa, Á. Koleszár, I. Moulitsas and **L. Könözsy**, 'Performance Evaluation of a Two-Dimensional Lattice Boltzmann Solver Using CUDA and PGAS UPC Based Parallelisation', *ACM Transactions on Mathematical Software*, vol. 44, 2017, ISSN: 0098-3500. DOI: 10.1145/3085590.

[SP19] P. Salmon, **L. Könözsy**, C. Temple and S. Grove, 'Numerical Investigation on Various Heat Exchanger Performances to Determine an Optimum Configuration for Charge Air Cooler, Oil And Water Radiators in F1 Sidepods', *Applied Thermal Engineering*, vol. 117, pp. 235–244, 2017, ISSN: 1359-4311. DOI: 10.1016/j.applthermaleng.2017.02.026.

[SP20] E. P. Silva, M. Nele, e. M. P. F. Frutuoso and **L. Könözsy**, 'Underground Parallel Pipelines Domino Effect: An Analysis Based on Pipeline Crater Models and Historical Accidents', *Journal of Loss Prevention in the Process Industries*, vol. 43, pp. 315–331, 2016, ISSN: 0950-4230. DOI: 10.1016/j.jlp.2016.05.031.

[SP21] **L. Könözsy** and D. Drikakis, 'A Coupled High-Resolution Fractional-Step Artificial Compressibility and Pressure-Projection Formulation for Solving Incompressible Multi-Species Variable Density Flow Problem at Low Reynolds Numbers', in *CD-ROM Proceedings of the 6th European Congress on Computational Methods in Applied Sciences and Engineering (ECCOMAS), 2012, Vienna, Austria, Eds.: Eberhardsteiner, J.; Böhm, H.J.; Rammerstorfer, F.G., Publisher: Vienna University of Technology, Austria, pp. 1-15.*, 2012, pp. 3206–3220.

[SP22] **L. Könözsy**, P. Scienza and D. Drikakis, 'Validation of a Magneto- and Ferro-Hydrodynamic Model for Non-Isothermal Flows in conjunction with Newtonian and Non-Newtonian Fluids', in *ECCOMAS Congress 2016: Proceedings of the VII European Congress on Computational Methods in Applied Sciences and Engineering*, vol. 1, 2016, pp. 1061–1083. DOI: 10.7712/100016.1870.9372.

[SP23] P. Tsoutsanis, I. W. Kokkinakis, **L. Könözsy**, D. Drikakis, R. J. R. Williams and D. L. Youngs, 'Comparison of Structured- and Unstructured-Grid, Compressible and Incompressible Methods Using the Vortex Pairing Problem', *Computer Methods in Applied Mechanics and Engineering*, vol. 293, pp. 207–231, 2015, ISSN: 0045-7825. DOI: 10.1016/j.cma.2015.04.010.

[SP24] **L. Könözsy** and D. Drikakis, 'A Unified Fractional-Step, Artificial Compressibility and Pressure-Projection Formulation for Solving the Incompressible Navier–Stokes Equations', *Communications in Computational Physics*, vol. 16, no. 5, pp. 1135–1180, 2014, ISSN: 1815-2406. DOI: 10.4208/cicp.240713.080514a.

[SP25] **L. Könözsy**, M. S. Kharicha, S. Eck, M. Wu and A. Ludwig, 'Numerical and Experimental Investigation of NH4CL Solidification', *Materials Science Forum*, vol. 649, pp. 367–372, 2010, ISSN: 0255-5476. DOI: 10.4028/www.scientific.net/{MSF}.649.367.

[SP26] **L. Könözsy**, A. Ishmurzin, M. Grasser, M. Wu, A. Ludwig, R. Tanzer and W. Schützenhöfer, 'Columnar to Equiaxed Transition During Ingot Casting Using Ternary Alloy Composition', *Materials Science Forum*, vol. 649, pp. 349–354, 2010, ISSN: 0255-5476. DOI: 10.4028/www.scientific.net/{MSF}.649.349.

[SP27] **L. Könözsy**, S. Eck, M. S. Kharicha, M. Wu and A. Ludwig, 'Experimental and Numerical Investigations of NH4CL Solidification in a Mould: Part 2: Numerical Results', *International Journal of Cast Metals Research*, vol. 22, pp. 172–174, 2009, ISSN: 1364-0461. DOI: 10.1179/136404609{X}367605.

[SP28] **L. Könözsy**, A. Ishmurzin, F. Mayer, M. Grasser, M. Wu and A. Ludwig, 'Numerical Investigation of Grid Influence on Formation of Macrosegregation', *International Journal of Cast Metals Research*, vol. 22, pp. 175–178, 2009, ISSN: 1364-0461. DOI: 10.1179/136404609{X}367614.

[SP29] M. Wu, **L. Könözsy**, A. Ludwig, W. Schützenhöfer and R. Tanzer, 'On the Formation of Macrosegregations in Steel Ingot Castings', *Steel Research International*, vol. 79, pp. 637–644, 2008, ISSN: 1611-3683. DOI: 10.2374/{SRI}08{SP}020-79-2008-637.

Author's Books

[B1] **L. Könözsy**, *A New Hypothesis on the Anisotropic Reynolds Stress Tensor for Turbulent Flows, Volume I: Theoretical Background and Development of an Anisotropic Hybrid k-omega Shear-Stress Transport/Stochastic Turbulence Model*. Fluid Mechanics and Its Applications Series, Springer Nature Switzerland AG, 2019, ISBN: 9783030135423. DOI: 10.1007/978-3-030-13543-0.

[B2] **L. Könözsy**, *A New Hypothesis on the Anisotropic Reynolds Stress Tensor for Turbulent Flows, Volume II: Practical Implementation and Applications of an Anisotropic Hybrid k-omega Shear-Stress Transport/Stochastic Turbulence Model*. Fluid Mechanics and Its Applications Series, Springer Nature Switzerland AG, 2021, ISBN: 9783030606022. DOI: 10.1007/978-3-030-60603-9.